CONTINUUM MODELLING OF SILICON DIFFUSION IN INDIUM GALLIUM ARSENIDE

By

HENRY LEE ALDRIDGE JR.

A DISSERTATION PRESENTED TO THE GRADUATE SCHOOL
OF THE UNIVERSITY OF FLORIDA IN PARTIAL FULFILLMENT
OF THE REQUIREMENTS FOR THE DEGREE OF
DOCTOR OF PHILOSOPHY

UNIVERSITY OF FLORIDA

2016

To my parents, family and all of the past and present SWAMP group members

ACKNOWLEDGMENTS

First I want to thank my parents for always being a constant of love and support in my life, both in times of great challenges and in great triumph. Thanks to them and my immediate and extended family for believing in me more than I originally believed in myself.

There have been so many people that I have been in contact with, working with, and have the pleasure and opportunity to learn from during my time at UF. I've learned a great deal from being a part of this project, and have had professors and role models that have only empowered me. Thanks to Professor Kevin Jones for accepting me into his group in early 2013, and for his consistently great energy, interest, and enthusiasm for the research. Also thanks to Dr. Mark Law, Erin Patrick and their students for their guidance and collaboration in learning and utilizing FLOOXS. It's been great collaborating, discussing experiment models, and overcoming the occasional instance when FLOOXS returns panic errors but provides no clues to the root issue.

This is for all of those people who have inspired, enlightened, and blazed ahead, years before. It's a great thing to have something like legacy, or people that you can look up to, specifically in the SWAMP group. I want to say thanks to all of the swampies, past and the present, even though I may not have known the majority of them personally.

Very importantly I want to acknowledge my good friend and colleague Aaron Lind, who worked on the same funded project. He consistently approached things in a measured, methodical, and meticulous fashion and has been an outstanding role model for everyone in the group that knew him. I greatly enjoyed our several discussions, collaboration, sharing thoughts and bouncing experiment ideas off of one another.

I'd also like to thank the several external people that I have collaborated with, including the modelling group at Intel. Special thanks to Steve Cea, Martin Giles, Aaron Lilak, and Harold Kennel. I had to hit the ground running dealing with programming, scripting and modeling, I want to say thanks for all of your guidance. Thanks to Cory Bomberger, and Dr. Joshua Zide for working with us, providing MBE samples that added an additional dimension of study to our project. Thanks to Yevgeniy Puzyrev and Dr. Socrates Pantelides for generously supporting this work by doing DFT calculations specifically for our system, which paved the way for a more elaborate and physically based diffusion model to be developed.

I would also like to thank Semiconductor Research Corporation, Intel, Oak Ridge National Laboratory and GEM Graduate Fellowship program for financial support and providing research opportunities.

Finally, thanks to Nicholas Vito, Patrick Whiting and several others who have been positive characters and influences during my PhD track. Overall, several people helped me out along the way, and were all great influences. It has been a wonderful learning and growing experience these past few years.

TABLE OF CONTENTS

LIST OF TABLES

LIST OF FIGURES

Abstract of Dissertation Presented to the Graduate School
of the University of Florida in Partial Fulfillment of the
Requirements for the Degree of Doctor of Philosophy

CONTINUUM MODELLING OF SILICON DIFFUSION
IN INDIUM GALLIUM ARSENIDE
By

Henry Lee Aldridge Jr.

August 2016

Chair: Kevin S. Jones
Major: Materials Science and Engineering

A possible method to overcome the physical limitations experienced by continued transistor scaling and continue improvements in performance and power consumption is integration of III-V semiconductors as alternative channel materials for logic devices. Indium Gallium Arsenide (InGaAs) is such a material from the III-V semiconductor family, which exhibit superior electron mobilities and injection velocities than that of silicon. In order for InGaAs integration to be realized, contact resistances must be minimized through maximizing activation of dopants in this material. Additionally, redistribution of dopants during processing must be clearly understood and ultimately controlled at the nanometer-scale. In this work, the activation and diffusion behavior of silicon, a prominent n-type dopant in InGaAs, has been characterized and subsequently modelled using the Florida Object Oriented Process and Device Simulator (FLOOPS).

In contrast to previous reports, silicon exhibits non-negligible diffusion in InGaAs, even for smaller thermal budget rapid thermal anneals (RTAs). Its diffusion is heavily concentration-dependent, with broadening “shoulder-like” profiles when doping levels exceed 1-3×$10^{19}$$cm^{-3}$, for both ion-implanted and Molecular Beam Epitaxy (MBE)-grown cases. Likewise a max net-activation value of ~1.7×$10^{19}$$cm^{-3}$ is consistently reached

with enough thermal processing, regardless of doping method. In line with experimental results and several ab-initio calculation results, rapid concentration-dependent diffusion of Si in InGaAs and the upper limits of its activation is believed to be governed by cation vacancies that serve as compensating defects in heavily n-type regions of InGaAs. These results are ultimately in line with an amphoteric defect model, where the activation limits of dopants are an intrinsic limitation of the material, rather than governed by individual dopant species or their methods of incorporation. As a result a Fermi level dependent point defect diffusion model and activation limit model were subsequently developed in FLOOPS with outputs in good agreement with experimental results.

CHAPTER 1
INTRODUCTION

1.1 Scaling and Moore's Law

Scaling of devices is the main trend that has driven the semiconductor industry for several decades. Doubling the number of transistors every 12-18 months, also known as Moore's Law[1], has decreased the average cost per transistor, and ultimately has had a transformative impact on everyday life. Cheaper devices have allowed advanced technology and capabilities to be attainable for billions of people across the globe, with greater accessibility than ever before. Classic Dennard scaling has been implemented to accomplish this, which is decreasing of feature dimensions, such as oxide thickness, channel length, and source and drain depths by a scaling factor κ[2,3], as demonstrated in Figure 1-1.

Likewise, the applied voltages have scaled at its own, albeit slower pace, usually by factor κ' [4]. As features continued to decrease in size, a short channel regime was finally met, which had its own set of challenges- most notably short channel effects (SCEs), where electrostatic control of the transistor becomes difficult with smaller dimensions [3]. Multigate geometries, such as finFETs and Gate-All-Around (GAA) FETs have been developed to obtain greater electrostatic control over silicon devices as they continued to scale, depicted in Figure 1-2.

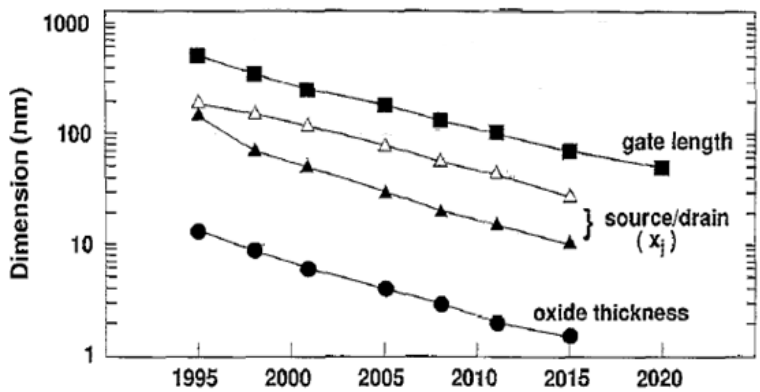

Figure 1-1. Continued decrease in gate length, source and drain junction depth, oxide thickness with time[3]

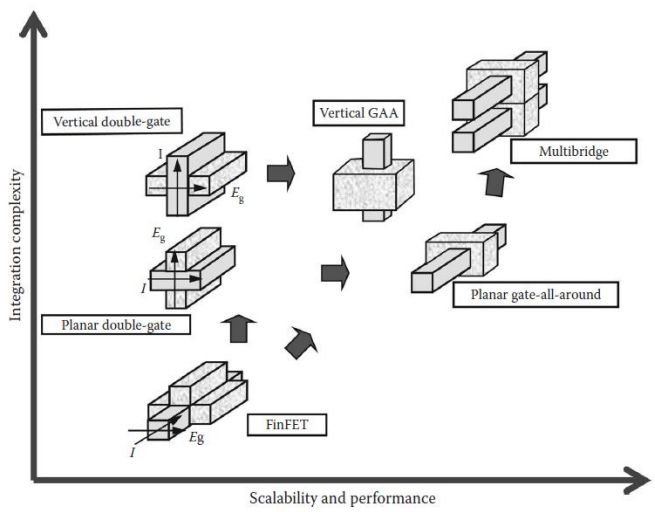

Figure 1-2. Illustration of several Multigate devices, including FinFETs and gate all around (GAA) configurations[5]. I = current and E_g=electric field.

Smaller dimensions and lower power consumption demands are pushing conventional silicon-based logic to its physical limit, where device control and cost effectiveness become harder to attain as the industry approaches the 2-3nm nodes. This is reflected in the shift of International Technology Working Group (ITRS) roadmap, where advances in the industry will no longer use device scaling as a sole metric of progress. ITRS 2.0, which was developed between 2012-2014, will also account for alternative material development, such as InSb, InGaAs, graphene and carbon

nanotubes, and development of mobile and server-focused computing as well as the Internet of things[6–8]. Ultimately, the semiconductor industry will now look to alternative materials and larger scopes of systems to continue trends of equivalent increases in speed, cost-effectiveness and performance. Further use and development of III-Vs semiconductors is one method to further this technological push.

1.2 III-V Materials

Due to the physical limitations of scaling silicon-based devices, alternative materials are needed in order to continue this scaling and performance trend. One major example of this is use of high-k dielectrics for the gate oxides instead of silicon dioxide to prevent electron tunneling[9]. Alternative channel materials are also an important area of research for current transistor development. III-V semiconductors have traditionally found widespread use in optoelectronic applications, in part due to their direct band gaps and tunable lattice constants[10].

1.2.1 III-V Characteristics and Challenges

Implementing logic devices with channel materials that have higher carrier injection velocities, would allow for faster transistor switching than their silicon counterparts. III-V semiconductors are currently prime candidates for transistor channel materials due to this very characteristic. This family of materials consists of elements from group III and group V of the periodic table, and could be an alloy of these species. For the scope of this work, the InAs and GaAs alloying composition is lattice matched to InP ($In_{0.53}Ga_{0.47}As$), but will be referred to as “InGaAs” in this work, unless a different composition is specifically noted.

III-V electron mobilities are significantly higher than silicon counterparts in the ballistic regime, with mobilities ≥9200 $cm^2 V^{-1}s^{-1}$, compared to 1450 $cm^2 V^{-1}s^{-1}$ for

unstrained silicon, as shown in Figures 1-3 and 1-4[10]. Figures 1-4 through 1-6 present some major parameter differences between some III-V semiconductors, Si, and Germanium[11] and Equation 1-1 illustrates how having a lower effective mass (m_t^*) contributes to a larger carrier velocity, with a given transistor length (T_L)[12].

$$v_T \propto \sqrt{\frac{2k_B T_L}{\pi\, m_t^*}} \tag{1-1}$$

The need for lower power consumption and faster switching is greatly influenced by the resistances of the transistor. The need for lower contact resistances are of great importance, with a source and drain resistivity of less than 15 Ω-μm and 1 Ω-μm^2 required to continue current ITRS scaling trends[13]. In order to mitigate these significant resistances, improved dopant activation is a paramount task.

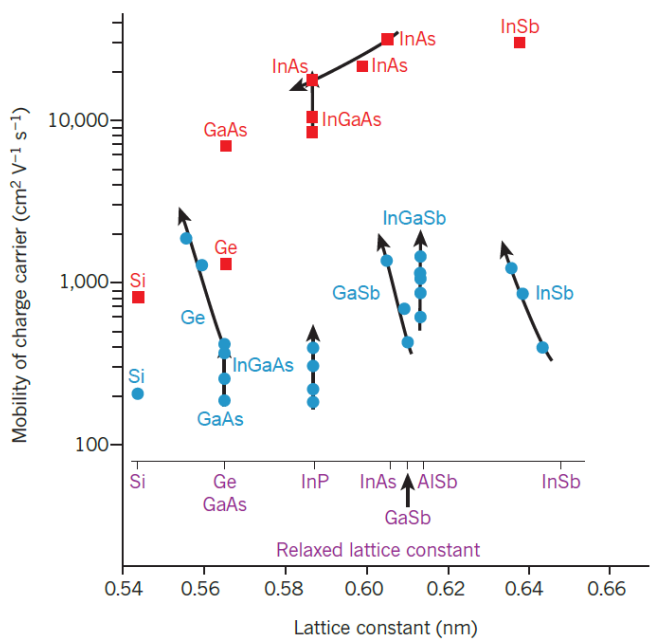

Figure 1-3. Electron and hole mobilities of various III-V semiconductors, compared with silicon and germanium[10].

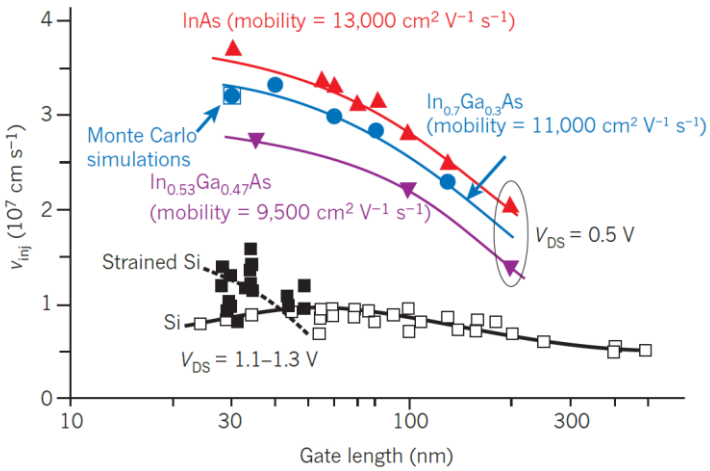

Figure 1-4. Injection velocities of III-V materials compared to that of Si and Ge[10].

	Si	Ge	GaAs	InP	InAs	InSb
Electron mobility (cm²/Vs)	1600	3900	9200	5400	40000	77000
Electron effective mass ($/m_0$)	m_t: 0.19 m_l: 0.916	m_t: 0.082 m_l: 1.467	0.067	0.082	0.023	0.014
Hole mobility (cm²/Vs)	430	1900	400	200	500	850
Hole effective mass ($/m_0$)	m_{HH}: 0.49 m_{LH}: 0.16	m_{HH}: 0.28 m_{LH}: 0.044	m_{HH}: 0.45 m_{LH}: 0.082	m_{HH}: 0.45 m_{LH}: 0.12	m_{HH}: 0.57 m_{LH}: 0.35	m_{HH}: 0.44 m_{LH}: 0.016
Bandgap (eV)	1.12	0.66	1.42	1.34	0.36	0.17
Permittivity	11.8	16	12	12.6	14.8	17

m_{HH}, mass of heavy holes; m_{LH}, mass of light holes; m_t, transverse effective mass; m_l, longitudinal effective mass.[10]

Figure 1-5. Electrical Properties of SI, Ge, and various III-V compound semiconductors[11]

Fundamental differences require careful consideration when determining device design using new materials. As shown from Figure 1-5, the electron effective mass for III-Arsenides are significantly lower than that of silicon, which allows for greater mobility and lower operating voltages. This this lower effective electron mass also leads to lower density of states for a given material, as characterized by[14]:

$$g(E) = \left(8\pi 2^{\frac{1}{2}}\right)\left(\frac{m_e}{h^2}\right)^{\frac{3}{2}} E^{\frac{1}{2}} \tag{1-2}$$

Where the electron effective mass (m_e) is proportional to the density of states g(E) for a given material. The density of states, and ultimately the attainable carrier concentrations for GaAs and InAs are significantly lower than that of silicon.

This also leads to challenges with bulk and ultra-thin body (UTB) device applications, where the centroid of inversion charge is deeper in the bulk, and at a lower peak concentrations than their silicon counterparts as seen in Figure 1-6. In order to have comparable electrostatic control (λ) of an InGaAs thin-body field effect transistor (FET) to that of a silicon FET, the fin channel thickness would need to be thinner proportional to the ratio of the dielectric constant of the two materials ($\varepsilon_{III-V}/\varepsilon_{Si}$) illustrated by Equation 1-3[12]. Clearly these limitations must be accounted for, especially in light of smaller device dimensions.

$$\lambda=\sqrt{\frac{\varepsilon_S}{\varepsilon_{ox}} t_S t_{ox}} \tag{1-3}$$

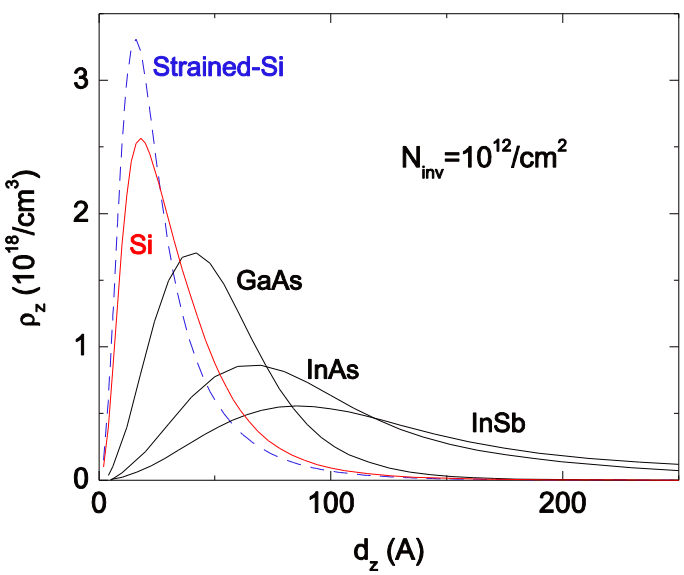

Figure 1-6. Inversion layer charge concentrations and depths for various semiconductors [12].

Contact resistances become predominant as devices are scaled further. Equation 1-4 illustrates the direct dependence of surface contact resistivity (ρ_c) on contact resistance (R_{co}) for short channel scales[4].

$$R_{CO} = \frac{\rho_C}{W l_c} \tag{1-4}$$

In order to obtain contact resistivities down to 1 Ω-μm^2 following IRTS projections, n-type doping levels of approaching 1×10^{20} cm^{-3} in $In_{0.53}Ga_{0.47}As$ are needed[15]. Figure 1-7 present the intrinsic and maximum carrier concentrations for InP, GaAs, and $In_{0.53}Ga_{0.47}As$. Attaining activation levels closer to this maximum limit for InGaAs was a central goal of this work.

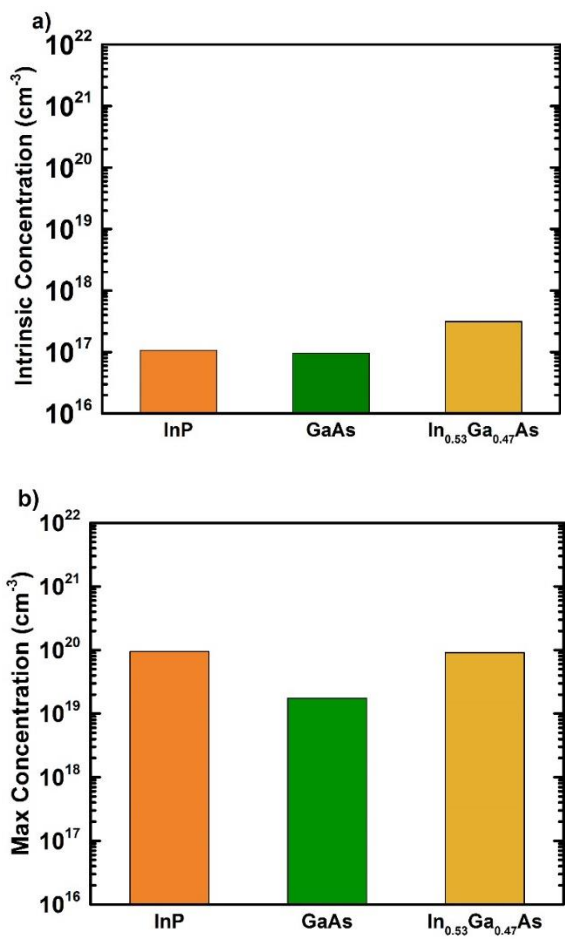

Figure1-7. Carrier concentrations of InP, GaAs and $In_{0.53}Ga_{0.47}As$ for a) intrinsic conditions and b) maximum values per material[16].

1.2.2 III-V Sublattices and Defects

Accounting for and maximizing activation in III-Vs, including InGaAs, will require study and consideration of atomic structure and point defects. One major difference between Si and III-Vs are there are two sublattice in III-V materials: the cation and anion sublattice, as illustrated in Figure 1-8. III-Vs consist of different elements from group III and group V of the periodic table, and incorporating high enough levels of additional elements from these groups can lead to alloys, notable ones include AlInAs, AlGaAs, InGaAs, and InAsSb.

The existence of two or more different elements present in a unit cell of the material on two sublattices leads to additional types of point defects, such cation and anion vacancies and interstitials. III-Vs also can have antisite defects, which is where a cation or anion are on the wrong sublattice, such as a gallium atom on an arsenic site ($\mathrm{Ga}_{\mathrm{As}}^{-1}$) or an arsenic atom on a Gallium site ($\mathrm{As}_{\mathrm{Ga}}^{+1}$) in GaAs for example. These defects can lead to comparatively large interface trap densities that make it harder to invert the transistor channel under a given electric field. This issue of inversion can be exacerbated with longer active channel lengths and greater interface surface areas of FinFETs and other multigate structures. Due to the additional lattice, not all point defect-atomic interactions can be assumed to be between first nearest neighbor pairs, like in elementary semiconductors. As will be discussed further in Chapter 2, many approaches to characterizing and modelling III-V behavior has included one or both sublattices. If only a single sublattice is considered, the closest interaction distance is the second-nearest neighbor pair. This very fact can lead to differences in how interstitials and vacancies recombine in III-Vs vs single element semiconductors.

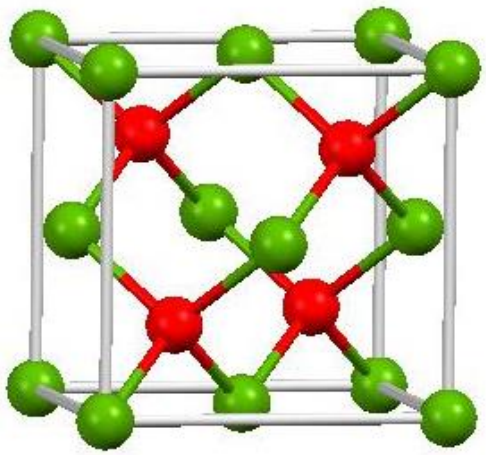

Figure 1-8. Unit Cell of zinc blende III-V semiconductor, GaAs. Gallium in green, arsenic in red.

Doping studies have been carried out to maximize activation in III-V materials, including InGaAs, in this work. Physical, and more importantly, electrical solubility is of paramount importance to understand. Solubility of an impurity is the amount of a material that can dissolved into a matrix as a solid solution, without forming separate phases or precipitates[17]. For silicon system, it is comparatively simple since there are no differing sublattices. In the case of III-Arsenides, consideration of dopant or defect self-compensation should be taken into account with dealing with incorporation of impurities into the bulk. Several additional possibilities must be taken into account for impurity incorporation in III-V systems.

1.2.3 Possible Form of Integration

Aside from III-V channel doping, another apparent challenge is the integration of the material on a Si-based substrate. Large concentrations of defects, such as threading dislocations, can propagate due to lattice mismatch of III-V layer on silicon. Layers of graded lattice constant material is one method to account for this lattice mismatch, and can minimize formation of defects into the electrically active areas.

Groups such as Kohen et al. have demonstrated the use of buffer layers, such as Ge to mitigate the growth of defects in the uppermost GaAs layer grown by MOCVD as shown in Figure 1-9.

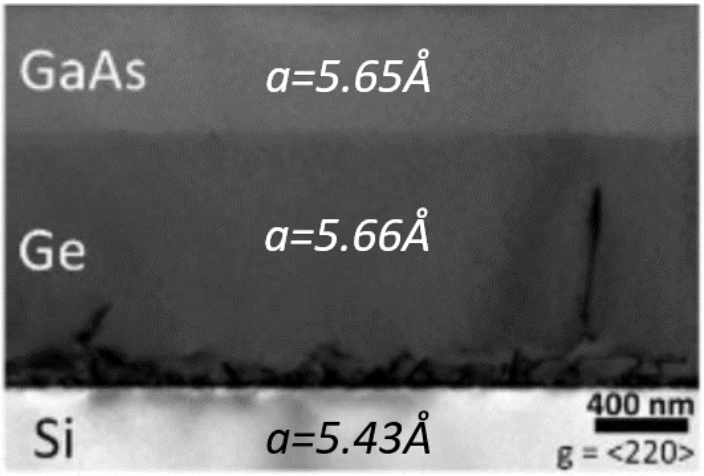

Figure 1-9. Metal Organic Chemical Vapor Deposition (MOCVD) Growth of GaAs onto Si substrate through use of Ge buffer layer. Respective lattice constants are overlaid[18].

It is likely that III-As materials will be processed as NMOS channels in junction with Germanium-based PMOS for future IC systems[19,20], using their superior electron and hole mobilities respectively. Both of these device types will be developed on a Si substrate due to the maturity and pre-established position of Si-based processing tools and techniques. Figure 1-10 is one example of this co-integration concept involving III-Vs and Ge channel CMOS transistors.

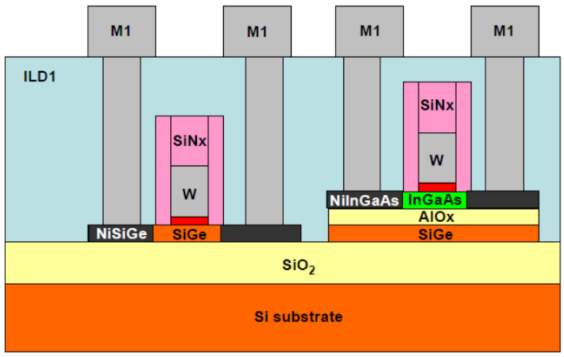

Figure 1-10. Illustration of complementary InGaAs and Ge channel MOSFETS for CMOS applications[19].

1.3 Contributions to the Field

In this work, silicon diffusion and activation behavior in $In_{0.53}Ga_{0.47}As$ has been explored and characterized, with the purpose of maximizing n-type activation. The nature and extent of silicon diffusion in InGaAs has been characterized with a continuum-based dopant-diffusion diffusion model in FLOOPS and has been used to predict profile evolution and activation levels with thermal processing. Major assumptions and perspectives from past work needs to be reconsidered in light of the activation and diffusion behavior manifest in this project, and will be discussed.

1.4 Organization of Dissertation

This document will first review literature related the activation and diffusion of dopants, primarily Si in InGaAs, GaAs and related materials in Chapter 2. Prominent recurring processing and characterization techniques used for this project and relevant topics will be discussed in Chapter 3. Notable activation and diffusion experimental results are presented and discussed in Chapter 4. Various programs, simulation tools, and developed dopant diffusion and activation models are described and presented in Chapter 5. Finally conclusions and suggestions for future work are included in Chapter 6.

CHAPTER 2
LITERATURE REVIEW

In Chapter 2 diffusion of Si in InGaAs and related systems is a major focus. Activation behavior and its connection with diffusion will also be discussed.

2.1 Diffusion Basics

Diffusion is the redistribution of matter within a given medium, and should be accounted for when dealing with activation of dopants in a medium. Diffusion of impurities and defects in semiconductors is just one subset of the fundamental phenomena observed and studied in nature. Clearly gas phase and liquid phase diffusion generally occur at faster rates than in solids. This is in part due to the periodic lattice, higher density, and greater interatomic interactions of the solid and crystalline diffusing medium[21]. Diffusion flux (J), is defined as the number of a species moving through a given area perpendicular to its direction of movement, as illustrated by Fick's first Law of diffusion:

$$J = -D\left(\frac{\partial C}{\partial x}\right) \tag{2-1}$$

Where the primary driving force for the flux of an impurity is dependent on the concentration gradient of that impurity in a medium. In a three dimensional volume, if the incoming and outgoing fluxes of all three dimensions balance, there is an accumulation or loss of the diffusing species in that volume. An illustration of species diffusing through a finite volume is included in Figure 2-1[21].

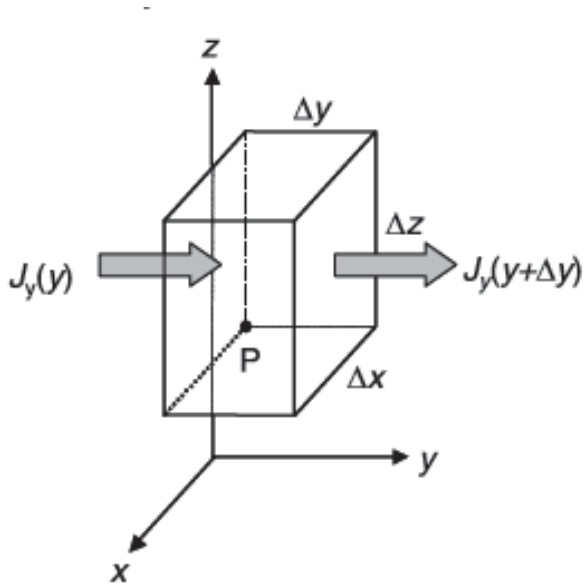

Figure 2-1. Illustration of flux through a finite-volume medium[21].

For a finite source of a diffusing species, Fick's second law is represented as:

$$\left(\frac{\partial C}{\partial t}\right) = D\left(\frac{\partial^2 C}{\partial x^2}\right) \tag{2-2}$$

Where diffusivity is a function of temperature as shown through a simple Arrhenius relationship:

$$D = D_0 \exp\left(-\frac{E_a}{kT}\right) \tag{2-3}$$

Where D_0 is the prefactor and E_a is the activation energy needed for an impurity to diffuse. The Diffusivity (D) described in Equation 2-3 above is taking a binary approach towards diffusion. A multicomponent diffusivity approach can also be taken, where the diffusivities depend on the local concentrations of the elemental constituents in the medium, commonly used in more complex systems like superalloys[22]. For all subsequent discussions, diffusivity will take a binary impurity/matrix approach, as done in most semiconductor studies.

2.2 Diffusion Mechanisms Through Crystalline Solids

Unlike gases and liquids, a central method for impurities to diffuse in a single crystal semiconductor are through interaction with point defects. Absences of atoms in a lattice site (i.e. vacancies) are one method for which impurities and matrix atoms can redistribute through exchanging locations. Atoms not present on lattice sites, (interstitials) can also contribute to and influence diffusion[23].

At an atomic level, there are distinct regimes in the diffusion path for an atom redistributing through a substrate. As mentioned, diffusion is a thermally activated process. The frequency of jumps from one lattice site to another increases exponentially with increasing temperature as illustrated for interstitial and vacancy diffusers by equations 2-4 and 2-5 respectively[24]:

$$v = 4v_D \exp\left(-\frac{H_m^I}{kT}\right) \tag{2-4}$$

$$v = 4v_D \left(\frac{C_V}{N_S}\right) \exp\left(-\frac{H_m^V}{kT}\right) \tag{2-5}$$

The frequency of lattice plane jumps v is directly influenced by the material Debye frequency of phonons v_D, and number of equivalent potential interacting neighbor sites, which is four in the case of silicon. Since vacancy diffusers require vacancies in the vicinity to diffuse, the abundance of these point defects must be taken into account in Equation 2-5. The potential energy barrier of migration H_m^X or E_m is the "saddle," or high energy point between two stable low energy positions in the lattice. In the case of a vacancy diffuser, the diffusing atom is required to overcome this energy barrier in order to complete its diffusion jump to a vacant neighboring substitutional site as shown in Figure 2-2. The completion of this jump requires that: 1) the diffusing species has enough energy for motion, 2) vacancies are present in nearest-neighbor

sites, 3) the surrounding atoms move enough to prevent inhibition due to atomic repulsion.

An alternative to displaying the migration and vacancy concentration components separately in Equation 2-5 is to combine the values into a diffusion activation energy term E_a as originally included in Equation 2-3:

$$\frac{C_V}{N_S} = \exp\left(-\frac{H_f^V}{kT}\right) \tag{2-6}$$

$$H_f^V + H_m^V = E_a^V \tag{2-7}$$

The atomic frequency of jumps *v* can be connected back to Fick's first and second laws. In the case of cubic crystalline material, and assuming that the number of diffusion-aiding defects does not change significantly with distance, the diffusion coefficient *D* of a species can be defined as[25]:

$$D = a^2 v \tag{2-8}$$

Where *a* is the distance between equivalent neighbor lattice sites in the medium.

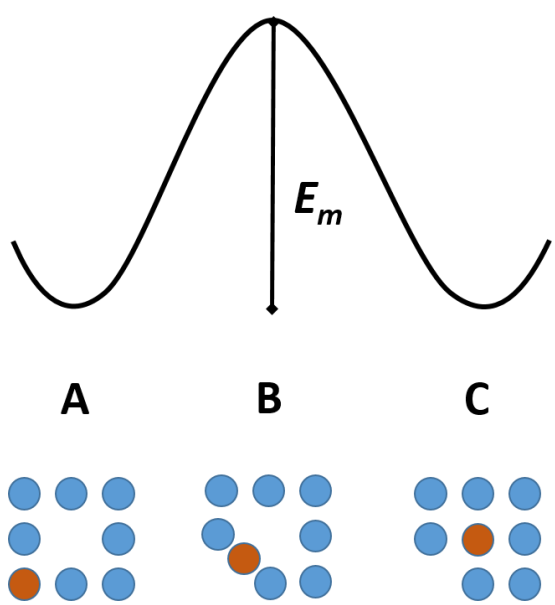

Figure 2-2. Illustration of saddle point regimes and the migration barrier (H_m, E_m) required for impurity displacement in a medium.

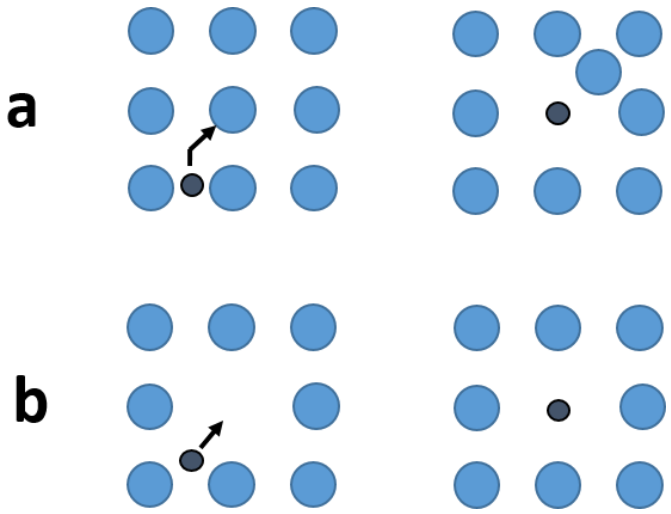

Figure 2-3. Illustration of two versions of interstitial diffusion. a) kick out and b) Frank-Turnbull mechanisms.

Finally, atoms that diffuse via an interstitial mechanism also have their own, usually lower migration barriers of diffusion between interstitial sites. Interstitial diffusers are generally faster than vacancy diffusers, due to lower bonding and interaction with surrounding lattice atoms, and a larger number of available locations to diffuse. Interstitials can be formed through the Frank-Turnbull reaction, where a vacancy and interstitial are created simultaneously, when an atom moves off of a substitutional site. They can also be formed through a kick-out mechanism, where an interstitial replaces a substitutional atom in the lattice, generating another interstitial. Both of these mechanisms are illustrated in Figure 2-3. Another interstitial configuration, referred as an interstitialcy, is when two interstitial atoms occupy the location of a single substitutional site in the lattice[26]. Despite their distinct nature, these will largely be considered as interstitials when dealing with experimental and modelling results.

It is important to note that in order to have a net redistribution of an atom or impurity, there has to be other diffusion-aiding defects in the diffusing direction. Alternatively, the initial diffusion aiding defect would have to migrate to another location

in relation to the impurity, allowing net displacement to occur. Murray et al. describes this mechanism for net displacement of Si, as shown in Figure 2-4.

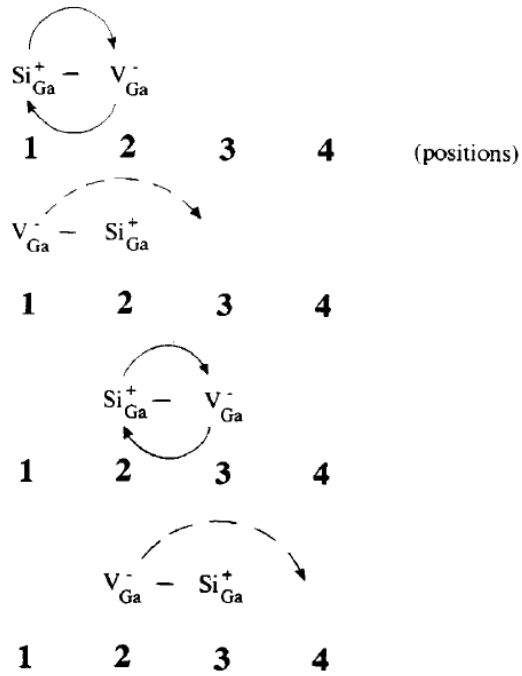

Figure 2-4. Migration of a defect in a lattice enabling net displacement of a dopant[27].

2.3 Point Defects

2.3.1 Point Defect Formation

Since impurities clearly require defects in order to move in a semiconductor lattice, the concentration and formation of point defects are an important value to consider. For any temperature over 0K, a finite number of defects will be present in a semiconductor[26,28]. The number of point defects present is dependent on temperature as well as the lattice density of the matrix as seen in Equation 2-9.

$$\frac{[C_X]}{[C_S]} = \theta_x exp\left[\frac{-G_x^f}{kT}\right] = \theta_x exp\left[\frac{S_x^f}{k}\right] exp\left[\frac{-H_x^f}{kT}\right] \quad (2\text{-}9)$$

Where C_x and C_s are the point defect and lattice density respectively. Dopant configuration, or degeneracy factor θ is the number of equivalent defect configurations

of a defect, which is 4 for first nearest neighbor pairs in silicon, and 12 for the second nearest neighbor pair in the cation sublattice of III-Arsenides. G_x^f , S_x^f and H_x^f , are the Gibbs free energy, entropy and enthalpy of formation for the given defect, respectively. At higher temperatures, more defects are present, enabling more pronounced dopant diffusion.

2.3.2 Charged Point Defects

Defects have the ability to transition to different charges states, based on the electron richness, or Fermi level of the host material. Neutral defects have dangling bonds, which can obtain electrons from the surrounding lattice or donate electrons to the material[28]. A charge state transition can be illustrated with the ionization of an acceptor type defect as shown in equation:

$$V^0 \leftrightarrow V^{-1} + h^{+1} \tag{2-10}$$

While a corresponding reaction of the ionization of a donor type defect is illustrated in Equation 2-11:

$$I_{III}^0 \leftrightarrow I^{1+} + e^{1-} \tag{2-11}$$

In both cases, a neutral defect is converted to a charged defect. The relative concentration of charged defects can be deduced from the Equation 2-12 and 2-13 below:

$$\frac{[X^{1-}]}{[X^0]} = \frac{\theta_{X^{1-}}}{\theta_{X^0}} \exp\left[\frac{E_F - E_{X^{1-}}}{kT}\right] \tag{2-12}$$

$$\frac{[X^{1+}]}{[X^0]} = \frac{\theta_{X^{1+}}}{\theta_{X^0}} \exp\left[\frac{E_{X^{1+}} - E_F}{kT}\right] \tag{2-13}$$

This approach can be expanded for defects with greater amounts of charge.

$$\frac{[X^{2-}]}{[X^0]} = \frac{\theta_{X^{2-}}}{\theta_{X^0}} \exp\left[-\frac{E_{X^{2-}} + E_{X^{1-}} - 2E_F}{kT}\right] \tag{2-14}$$

$$\frac{[X^{2+}]}{[X^0]} = \frac{\theta_{X^{2+}}}{\theta_{X^0}} \exp\left[-\frac{2E_F - E_{X^{2+}} + E_{X^{1+}}}{kT}\right] \quad (2\text{-}15)$$

Where the relative concentration of charged defects are determined by temperature, the ionization energies of the respective defects and the local fermi level of the material. Groups like Tan et al. calculated the equilibrium concentration of gallium vacancies of several different charge states with respect to n-type doping, and illustrated this change for triply ionized gallium vacancies (V_{Ga}^{3-}). A more direct look at this approach, which is covered and utilized the in the FLOOPS diffusion model, is discussed in Chapter 5. An illustration of the charge-state dependence on concentration of defects with respect to doping level is included in Figure 2-5.

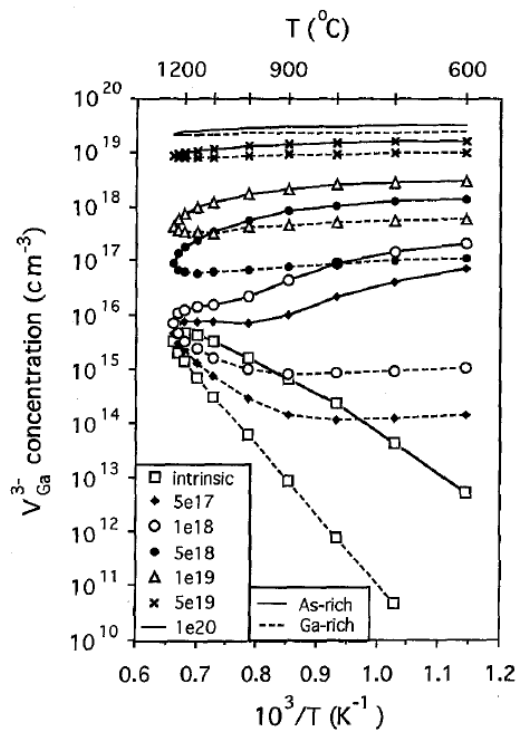

Figure 2-5. Chart showing concentration of different charged cation vacancies with respect to n-type doping levels[29].As seen from several diffusion studies in silicon and III-As alike, and the current work with InGaAs as a substrate, charged point defects can play a major role in dopant diffusion and activation.

2.4 Silicon Diffusion

2.4.1 Silicon Diffusion in InGaAs

Si diffusion and activation in InGaAs has been published and somewhat considered in the past, but was not considered to be a major problem. Even as recently as 2011[30], silicon diffusion in InGaAs was reported as inconsequential, summarized by the negligible diffusion observed upon thermal processing in Figure 2-6. As will be illustrated in Chapter 4, silicon diffusion in InGaAs was found to be significant at concentrations exceeding ~1×10^{19}cm^{-3}. This behavior was subsequently studied, modelled and predicted in this project.

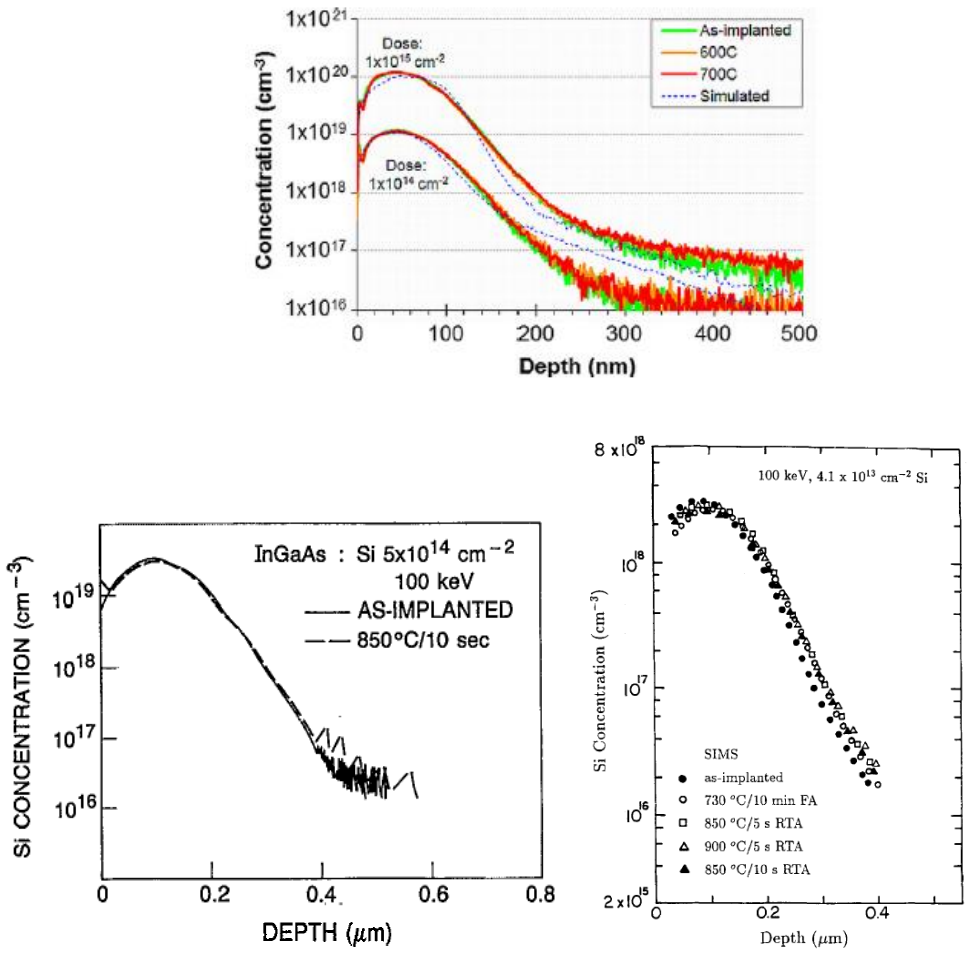

Figure 2-6. SIMS profiles of ion-implanted Si in InGaAs from previous annealing studies suggesting negligible diffusion[30–32].

Since InGaAs is an alloy of two III-As materials (InAs and GaAs), it is helpful to account for previous studies dealing with silicon diffusion in these individual materials. Si diffusion studies in GaAs will be the main focus since it is the most-studied of the three materials. A few superlattice studies will also be mentioned, since they can shed helpful insight into diffusion tendencies as well.

2.4.2 Si Diffusion in GaAs and Related Materials

GaAs has is the more thoroughly studied of the III-Arsenides, and in line with this many proposed mechanisms have been developed over the years to characterize dopant diffusion in it. It is especially relevant for better understanding Si diffusion and activation in InGaAs given that the major difference is the additional cation species, indium, being present in the alloy.

In silicon systems, there was significant work carried out on modelling and studying the effects of extended defects on dopant diffusion, notably interstitial loops and {311} defects on interstitial diffusers like that of boron and phosphorus. Great care was taken to model the kinetics of extended defect evolution, given that those defects were comparably more stable, than those in InGaAs[33,34]. There is no experimental evidence that suggests that silicon in InGaAs or related systems create PIC or BIC like clusters that migrate through the lattice.

It is commonly considered that Si diffuses via a vacancy mechanism. Earlier works like those of Grenier and Gibbons proposed that a Si_{Ga}-Si_{As} neutral pair were the mobile species in GaAs, where they would aid each other in diffusion by moving on their respective sublattice through the reaction[35]:

$$(Si_{Ga}^{+}Si_{As}^{-}) + V_{Ga} \leftrightarrow V_{Ga} + (Si_{As}^{-}Si_{Ga}^{+}) \tag{2-16}$$

It was proposed that the silicon on a cation site would exchange locations with a cation vacancy, then leading to this following reaction:

$$(Si_{As}^{-}Si_{Ga}^{+}) + V_{As} \leftrightarrow V_{As} + (Si_{Ga}^{+}Si_{As}^{-}) \tag{2-17}$$

Where the Si atom on an anion site would proceed to exchange with an arsenic vacancy in turn. A repetition of these reactions would enable a net displacement of the Si pair through the lattice. Interestingly, this neutral pair model did not account for possible charge states of the defects, particularly the cation and anion vacancies. The population of charged defects is clearly a pronounced phenomenon in III-Vs, and theoretical calculations suggest this, especially those that point to charged substitutional dopant-vacancy pairs as the primary mechanism of diffusion and governors of the extent of activation.

Also, if the neutral pairs were present in appreciable numbers, there would be no net change in the position of the fermi level, so certain acceptor or donor-type defects that could aid in diffusion would be less likely to form. Previous work have suggested that this neutral pair would tend to be less mobile than alternative mechanisms[36]. Due to these results and conclusions, other mechanisms were proposed for Si diffusion in InGaAs, with the V_{III}-Si_{III} pair presented often at the mobile species in heavily n-type GaAs systems.

Further modelling efforts were carried out by Tan et al, and came up with further evidence against this neutral pair model. The group had significant issues fitting the profile parameters through parametric adjustment[37]. Due to this fundamental issue with the model, they no longer supported the neutral pair model as the dominant diffusion mechanism of silicon in GaAs.

The arsenic sublattice was commonly viewed as a route for self-compensation for Si when doping concentrations are high enough[38]. Studies and calculation works have illustrated that diffusion via the arsenic sublattice is not as prominent as Si diffusion via the cation sublattice. Naturally, the growth and subsequent capping of III-As samples with an arsenic overpressure inhibits the formation of anion vacancies. This dependence of arsenic vacancy concentration on As overpressure are illustrated by the equations[39]:

$$As_{As} \leftrightarrow \frac{1}{4} As_4 + V_{As} \tag{2-18}$$

$$C_{V_{As}}^{eq} \propto (p_{As})^{-\frac{1}{4}} \tag{2-19}$$

Equation 2-19 is a result after application of the mass action law, where abundance of As in the gas phase diminishes the amount of arsenic vacancies at equilibrium. In As-Rich conditions, ab-initio calculations have suggested that the dominant As defect is the as antisite (As_{Ga}), and the arsenic interstitial (As_i), rather than the arsenic vacancy(V_{As})[40]. Other ab-initio calculation work has proposed that As diffuses via second nearest neighbor pair on the As sublattice[41].

$GaAs_{1-x}Sb_x$ and $GaAs_{1-x}P_x$ superlattice mixing experiments further illustrate how important arsenic overpressure is on the behavior and abundance of defects on the As sublattice. With a greater As overpressure, the group V site occupying species (Sb and P) diffused markedly faster than lower overpressures, indicating that the self-diffusion of the arsenic sublattice is predominantly the substitutional interstitial mechanism. All of these studies carried out in as-rich conditions point to As vacancies having a smaller role and influence that their cation counterparts- especially when doped heavily n-type.

Later works focused more on the gallium sublattice as the primary diffuser. Following the neutral nearest neighbor silicon pair model suggested by Grenier and gibbons, a cation vacancy silicon substitutional mechanism was promoted at the primary mechanism for silicon diffusion in GaAs and related systems, illustrated by the mechanism:

$$V_{III}^{-m} + Si_{III}^{+} \leftrightarrow \left(V_{III}\, Si_{III}\right)^{-(m-1)} \tag{2-20}$$

Where m is the charge state of the negatively charged gallium vacancy, and the second nearest neighbor pair redistributes through the lattice. The effective diffusivity of silicon or other substitutional n-type dopants is often characterized as[42]:

$$D_{eff} = \sum_m D_m \times [V_{Ga}^{m}] \tag{2-21}$$

When expanded out, taking different defect charge states into account, and put into a form following Shockley and Last[43], Equation 2-21 becomes:

$$D_{eff} = D_0 + D_{01}\left(\frac{n}{n_i}\right) + D_{02}\left(\frac{n}{n_i}\right)^2 + D_{03}\left(\frac{n}{n_i}\right)^3 \tag{2-22}$$

Equation 2-22 is a central basis for modelling substitutional dopant diffusion in silicon as well as other materials, including GaAs, and aspects of this approach is included in the diffusion models for Si diffusion in InGaAs, as described fully in Chapter 5.

Unlike the neutral nearest pair and vacancy diffusion in silicon, the proposed diffusion mechanisms involve interaction between the second nearest neighbor pairs in GaAs and related materials. Figure 2-7 illustrates the 12 equivalent second nearest neighbor cation sites for a given cation verses the four equivalent nearest neighbor sites in a diamond cubic elemental semiconductor system. Clearly from this difference alone,

there will be different energetics and nuances of dopant diffusion in III-V materials compared to silicon.

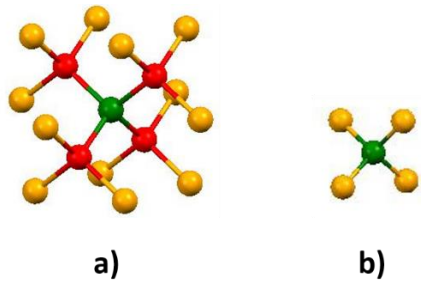

Figure 2-7. Illustration of a) the 12 second-nearest neighbor pairs (orange) of central cation site (green) compared to b) first nearest neighbor pairs in a silicon system with a central silicon atom (green).

Previous work have demonstrated and proposed concentration-dependence of Si diffusion in GaAs, like shown in Figure 2-8[42,44]. This enhanced diffusion was attributed to the increased concentration of vacancies present in the material at heavily doped regions. Again, superlattice studies shed further light, supporting this mechanism, where increasing n-type doping of group III species resulted in increasing diffusion, as reported in Figure 2-9[45].

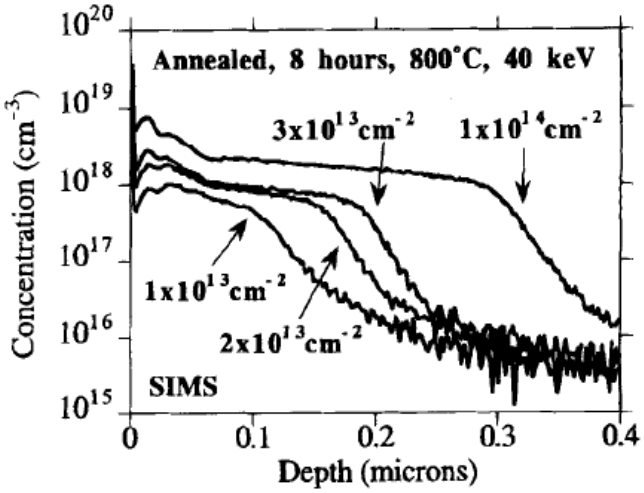

Figure 2-8. Concentration-dependent diffusion of Ion implanted Si in GaAs for various doses. [46]

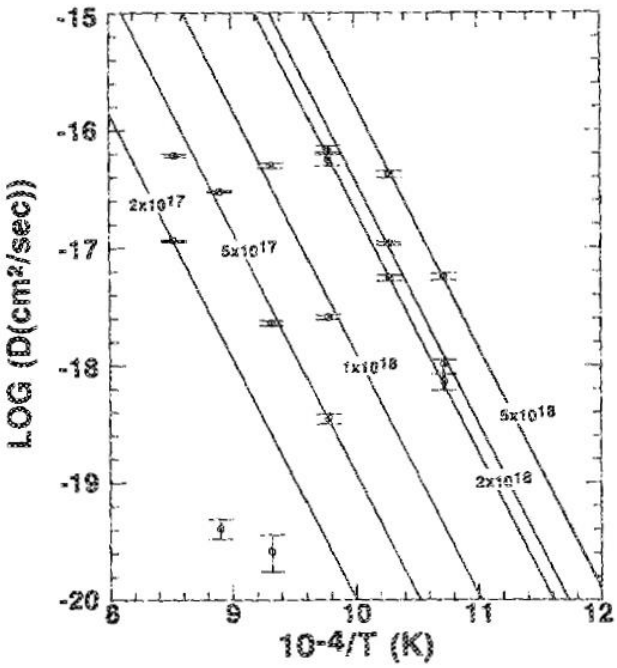

Figure 2-9. Enhancement of Al diffusion with an increase of Si concentrations in an AlAs-GaAs superlattice[45].

Unlike GaAs, InAs has a much smaller pool of literature, including diffusion data. InAs is more challenging of a material to handle and characterize, partially due to its brittleness. Other issues have been experienced when trying to measure carrier concentrations of InAs samples using Hall Effect, due its narrow band gap of 0.354 eV. Alternative methods such as Raman scattering was carried out determine the extent Si activation in InAs [47]. In terms of diffusion, it was also concluded that silicon has negligible diffusion upon anneal as illustrated in Figure 2-10, which is reminiscent of the ion implanted profiles in InGaAs[48].

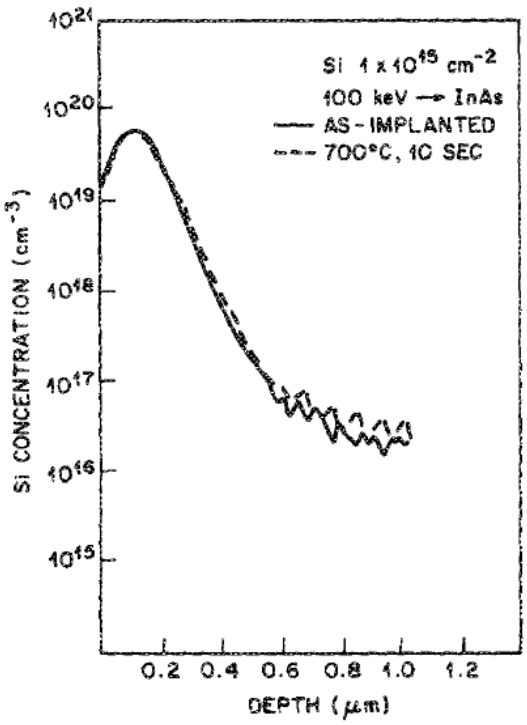

Figure 2-10. SIMS Profile of $1\times10^{15}cm^{-2}$ 100keV Si Implant into InAs before and after annealing at 700°C for 10s[48].

2.4.2.1 Recap - Diffusion of InGaAs

Similar concentration-dependent diffusion profiles are observed in InGaAs as was reported in GaAs, and the pursuit to fully characterize, model and predict this behavior is covered in Chapters 4 and 5. The primary mechanism implemented was the V_{III}-Si_{III} pair, similar to the prevailing proposed mechanism in GaAs.

2.4.2.2 Accounting for interstitials in literature

Formation of vacancies in n-type III-Arsenides and subsequent diffusion may be presented in literature, but the generation of interstitials from that vacancy formation must also be taken into account. Methods that could possibly point to generation of vacancies in heavily n-type GaAs and InGaAs are presented in HBT studies where rapid diffusion of p-type dopants in adjacent layers was observed. The proposed mechanism of this enhancement involves the generation of Frenkel pairs in the heavily

n-type GaAs or InGaAs layers. This generation of cation interstitials, which are thought to diffuse into adjacent p type layers enhancing interstitial diffusion of zinc in tunnel junctions of solar cells or in base layers of HBTs[49,50]. An illustration of this phenomena proposed by Takamoto et al. is included in Figure 2-11.

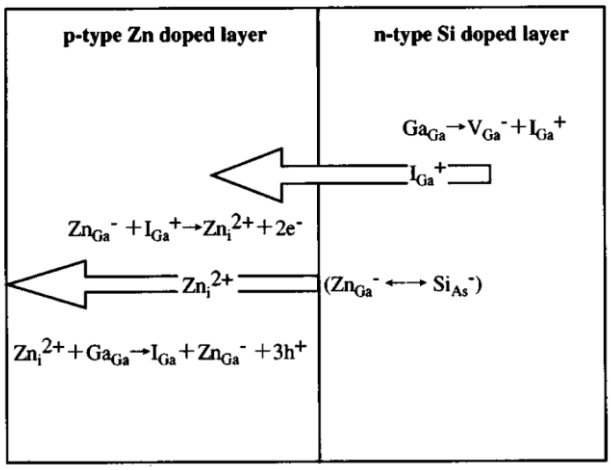

Figure 2-11. Illustration of diffusion model where interstitials generated from the fermi level effect enhance Zn diffusion in a tunnel junction[49].

2.4.3 Percolation

Percolation is one possible explanation of enhanced diffusion of silicon observed in GaAs and InGaAs. According to Stauffer, percolation is a phenomena dealing with statistics and probabilities. When a certain critical concentration (p_c) of an event or species exists in a system, a “super network” of those species are formed, enabling an enhancement or prolonging of that effect. An example illustrated by Stauffer was the enhancement in the spread of a fire in a grid as shown in Figure 2-12. When the concentration of trees on fire approached a specific value of p_c, clusters of burning trees spanned the entire swath of forest, assuming that the a fire could spread to adjacent trees[51].

From this approach, there was a critical concentration at which the fire could penetrate the entire forest, given that the concentration of fires was high enough, and a fire “superlattice” was formed. This phenomena can be applied to impurities in a crystalline medium as well. When concentrations of impurities are high enough in a semiconductor, they become a “super network” with an nth nearest neighbor distance away from each other. Their comparatively close proximity makes it easier for the diffusion-aiding defects such as vacancies to form and migrate through the lattice. Figure 2-13 illustrates the rapid enhancement of impurity diffusion when reaching a critical percolation threshold C_{th} in a theoretical material. The closer the defect is to an impurity in the “infinite” network of impurities, the lower the given barrier of migration is for that given defect, as illustrated for P and As-V pairs in silicon in Figures 2-14 and 2-15 respectively.

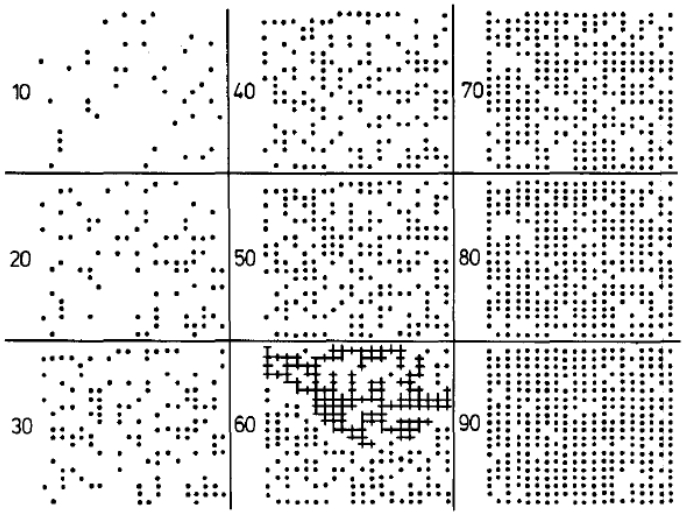

Figure 2-12. Illustration of percolation. Increase of concentration on a 20x20 square lattice. Series of crosses in 60 percent occupied lattice is the largest percolating cluster[52].

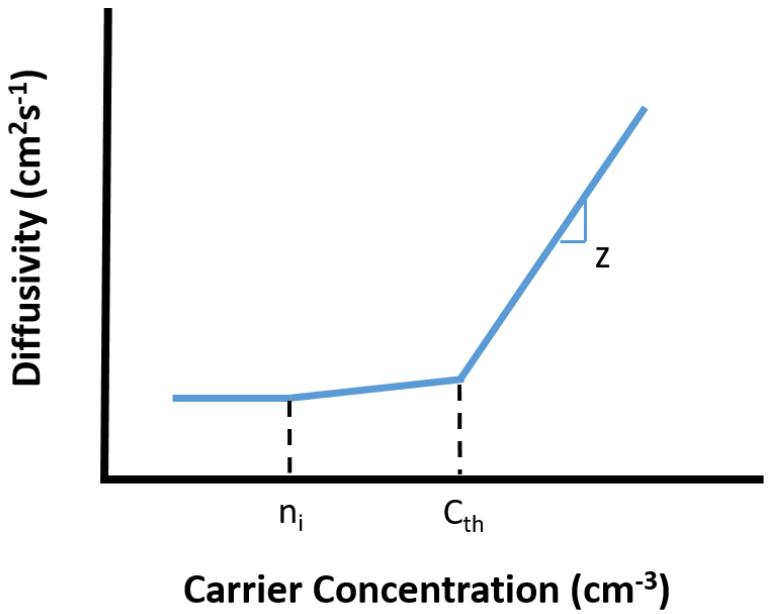

Figure 2-13. Illustration of Diffusivity enhancement due to reaching critical concentration p_c. The slope of the enhanced region is commonly viewed as the power of concentration dependence, or the corresponding charge state of the diffusion enabling defect.

DFT calculations from Xie et al. have suggested that the range for this lowering of migration energy is the 5th nearest neighbor site for As in silicon. Previous ab-initio calculations such as these have had its limitations, since supercell sizes were on the order of 64 atoms. Having a simulated structure that small could lead to inaccuracies in calculated migration and formation energies, since there would be unrealistically high concentrations of dopants and defects in the simulated volume. Later works suggest that this barrier lowering range is farther, up to a 7-9th nearest neighbor pair distance. Determining the effects and ranges of any sort supernetwork effect is computationally expensive.

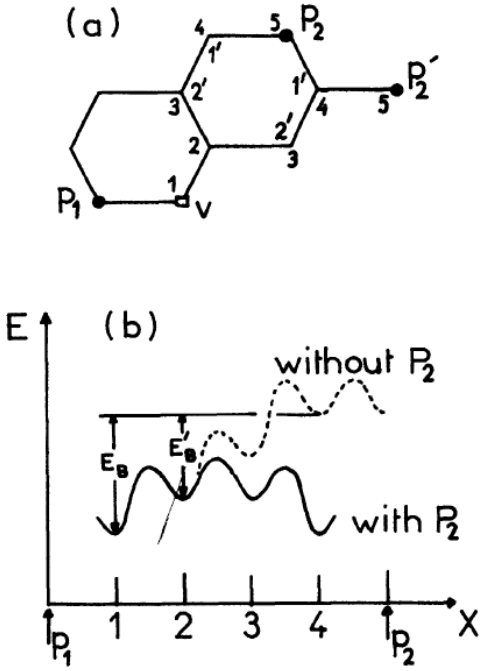

Figure 2-14. Schematic of Energy of migration barrier lowering with respect to another P atom in Si Lattice[53]

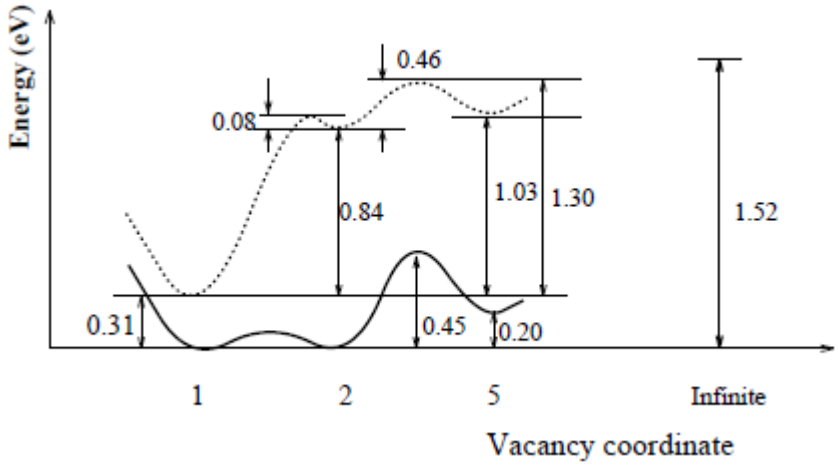

Figure 2-15. As-V pair Potential energy vs vacancy coordination with (solid line) and without (dotted line) 5 nearest neighbor As[54].

Although percolation is an interesting concept, the mechanism and nature of silicon diffusion has been studied in this work at a more fundamental level focusing on individual second nearest neighbor point defect pairs, rather than a large supernetwork.

2.5 Activation Review of Si in InGaAs

Diffusion is an important factor for creation of electrically-active regions, and is closely modelled and studied since it is a byproduct of thermal treatment. Another direct, and highly important aspect semiconductor processing is the electrical activation and solubility of the dopants. Both diffusion and activation are closely coupled, since both deal with occupation of lattice sites, interaction with point defects, and local fermi levels. Activation of dopants in III-Vs are relatively more challenging than for elemental semiconductors.

2.5.1 Site Occupancy and Solubility

Site occupancy is of great importance in understanding, and ultimately maximizing activation of a dopant in InGaAs. Having two sublattices more than doubles the amount of defects possible, and complicates understanding of what roles dopants play in the material. Certain species can be isoelectronic, where they do not donate or accept and electron when activated, such as Ga or P as shown on Figure 2-16. Other species that arises from this two sublattice system are amphoteric dopants, or dopants that can occupy both group III and group V sites in a compound semiconductor. In the case of III-Vs, group IV dopants such as Si, Ge, and Sn can occupy both cation and anion sites. Finally, there group II and group VI species can serve as acceptors and donors respectively. Other dopants, such as Be and Mg (not shown in Figure 2-16,) are also desirable p-type dopants. These two species are viewed as advantageous for ion implanting InGaAs, since they are both lighter than Zn, and can be implanted deeper and more accurately[55].

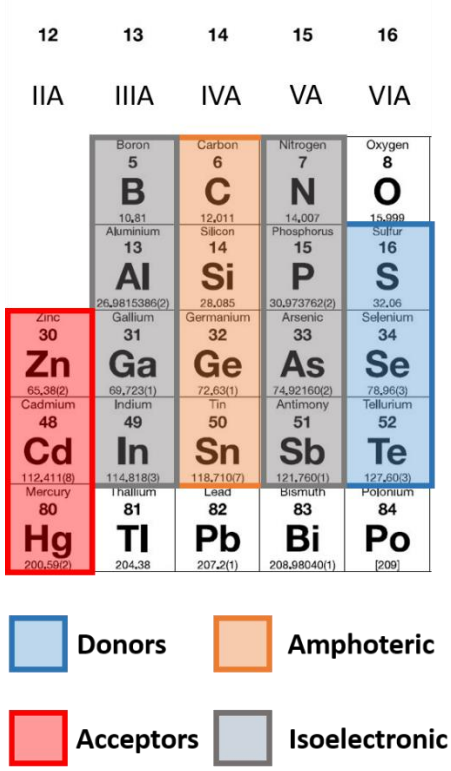

Figure 2-16. Different groups of elements from Periodic table, and their doping roles in III-V Semiconductors. Other notable p-type dopants, such as Be and Mg, are not shown.

One central parameter that determines not only chemical but electrical solubility of a dopant is its atomic size. The larger the atom, the more strain it would introduce into the host lattice, limiting how much can be incorporated into the solid solution. Despite clear evidence of the impact of dopant atomic size, there are other factors that govern where and how many atoms will ultimately reside in the semiconductor crystal. Growth conditions, such as process temperature, arsenic overpressure, and inert annealing ambient can all determine where amphoteric dopants such as silicon will reside. High As:III overpressures are used in an effort to promote relative abundance of cation vacancies and relative scarcity of anion vacancies to promote a greater degree of dopant incorporation on cation sites and n-type doping.

Amphoteric Nature of Si in III-Vs. Si can substitutionally occupy both the cation and anion site, and it was believed that this amphoteric characteristic was the cause for activation limits in III-Vs, including InGaAs. As mentioned, there is probability of self-compensation to occur once a certain concentration of certain dopants is reached. Figure 2-17 is an illustration of amphoteric manifestations of substitutional Si, as well as antisite defects in InGaAs, compared to a perfect crystal.

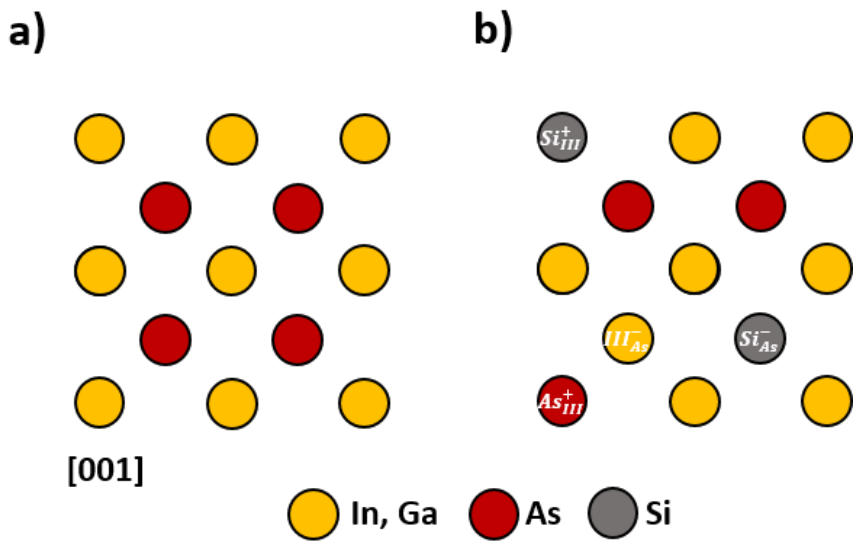

Figure 2-17. a) Perfect InGaAs unit cell in [001] direction. b) Illustration of self-compensation of amphoteric silicon and antisite defects in InGaAs unit cell.

Historically, activation of several dopants in a silicon, such as P and B, have been modelled by incorporating dissolution kinetics of extended defects, including {311} defects and loops[33,34,56]. A major difference with processing of dopants in III-Vs is the fact that extended defects and complexes appear to play a less significant role on dopant activation. Bhattacharya et al. have studied Si-implanted GaAs and have determined that 60-70% of the silicon were incorporated into substitutional lattice site following 10min 750 and 850°C anneals, while less than 2% clustering was observed[38,57]. In light of near-complete substitutional occupation of silicon onto lattice

sites a common parameter used for quantifying activation of III-Vs has been the compensation ration θ[58]:

$$\theta = \frac{N_A}{N_D} \tag{2-23}$$

Where N_a is the concentration of silicon acceptors while N_D is concentration of silicon donors in the material. Another parameter often used is the activation efficiency of a dopant, which is the percentage of the total amount of dopant introduced that is activated. The goal usually is the maximize n-type activation of Si, thus making the compensation ratio parameter as small as possible and the activation efficiency as high as possible.

2.5.2 Ion-Implantation

The advantages of ion implantation are described further in Chapter 3. Close control of dopant type, energy, and dose allows for specific concentrations, and thus leads to specific behavior of dopants upon annealing. Clearly there is a processing window in which a specific depth, peak concentration and temperature are needed in order to obtain the greatest activation possible at the desired scale. Comparatively high energy (>20keV) and or lower dose implants (≤ $1\times10^{14}cm^{-2}$) can lead to lower peak concentrations where the majority(60-100%) of silicon has been observed to incorporate on cation sites upon thermal processing[32,59]. As highlighted by Alian et al, low dose Si implantation into InGaAs allowed for greater activation efficiency than for higher dose implants at the same energies. Their reported activation efficiencies of Si^+ implanted into InGaAs at 50keV were 57% and 12.5% for 1×10^{14} and $1\times10^{15}cm^{-2}$ doses respectively[30].

As the Si doping increases, amphoteric behavior is thought to manifest, where self-compensation could occur in in the form of antisites, Si occupying anion sites, or Si_{Ga}-Si_{As} neutral nearest neighbor pairs[59]. In light of conditions of significant Si redistribution, neutral nearest neighbor pairs seem to be less plausible since they are thought to be not as mobile and not as favorable to form. Some previous activation models using the compensation ratio for GaAs even ignore the possibility that vacancies are electrically active and that interstitials could exist upon implant.

The current work for this project differs from GaAs and InGaAs Ion implantation studies in the past by combining shallower low energy implants (10-20keV) with doses (5×10^{14}-6×10^{14}) that reach the chemical peak concentration of Si at or above $1\times10^{20}cm^{-3}$ in an effort to create shallow junctions and maximize activation .

2.5.3 Co-Implantation

Even with varying different ion implantation conditions, there was ultimately a limit at which further activation was not attained. One of the highest net carrier concentrations of InGaAs implanted with silicon was around $1.7\times10^{19}cm^{-3}$ as reported by Rao et al[32]. Other studies have been carried out to obtain even higher levels of activation, through the use of co-implantation. The main principle of this approach is to use one or more additional species to implant into a material, where each different species would preferentially occupy certain lattice sites, further enhancing or influencing the net activation. Some works like that of Sugitani et al. suggest that implanting GaAs with phosphorous along with silicon enhanced n-type activation, and caused a smaller Photoluminescence (PL) peak intensity of Si_{As} and Ga_{As} acceptors[60]. They claimed that the largest activation enhancement came from the lowest 40 keV P^+ dose ($1\times10^{13}cm^{-2}$) co-implanted with 10keV $2\times10^{13}cm^{-2}$ Si^+ implant by about 34%.

Others have used co-implants to regulate stoichiometry, like implanting GaAs with arsenic to prevent arsenic vacancies from forming during an anneal, thus enhancing activation of ion implanted silicon by a reported 100% increase [61]. Again, these implant energies are relatively high, with low resulting peak concentrations: 150 keV ~1×10^{15}-1×10^{16}cm^{-2} and 100keV 2×10^{13}cm^{-2} for As^+ and Si^+ implants respectively.

Ambridge and Heckingbottom tried controlling site availability of the cation sublattice by co-implanting GaAs with gallium and selenium, with the purpose of improving n-type activation[62]. They carried out their study with the theory that the product of both types of vacancies (V_{Ga} and V_{As}) would remain constant for a material at thermodynamic equilibrium, so as fewer anion vacancies are present, more Ga vacancies are formed. With Selenium occupying anion sites, the co-implanted Ga^+ would circumvent any increase in cation vacancy formation. The group suggested that enhancement of a 1×10^{13}cm^{-2} or 2×10^{14}cm^{-2} 350 keV Ga^+ implant with a 390keV Ga^+ implant of equal dose upon annealing increased the percent activation from an average of 40% to a maximum of 90% for the single and dual implants respectively.

Co implants with inert gas species were also tried in the past, and have reported increased silicon activation. Liu et al. implanted GaAs with a 750keV 5×10^{12}-1×10^{13}cm^{-2} Ar^+ implant as a pretreatment, followed by a 2-5×10^{12}cm^{-2} Si^+ implant. They reported a consistent improvement in the compensation ratio θ (N_A/N_D decreasing) with decreasing Ar^+ dose[63]. Co-Implants have been repeatedly reported to improve activation percentages and compensation ratios in GaAs. It is yet to be known if this method of co-implantation would improve activation in InGaAs, particularly at the doses and concentrations we find relevant today.

2.5.4 Charged Defects and Their Role in Compensation

Amphoteric compensation and site selectivity should be considered as possibilities, but other viable mechanisms of activation behavior could be the predominant factor governing activation. One possible explanation for the observed limitation of activation levels in III-Vs could be due to the existence of stabilization fermi level E_{FS} that is specific for a semiconducting material. A specific consideration when dealing with compound semiconductors is the fact that the formation of defects can drastically change with respect fermi level, and can serve as donors or acceptors to remain at a stabilization fermi level E_{FS}. The basis of amphoteric defect model (ADM) presented by Walukiewicz suggests that at a given fermi level, certain point defects will form to counterbalance the fermi level shift away from the stabilization level due to doping[64,65]. Figure 2-18 shows possible acceptor and donor defect formation energies, which change with respect to fermi level. Point defects, such as cation vacancies, have the potential to serve as acceptors, as well as have the capacity to aid in significant silicon diffusion. This model is in good agreement with superlattice mixing studies where mixing was enhanced with greater n-type doping levels. Figures 2-18 and 2-19 illustrate the point that the maximum stable activation of a material is dependent on the relative location of the fermi level stabilization energy to the conduction band minimum or valence band maximum. Further evidence of a maximized activation is shown in Figure 2-20 for an array of free carrier concentrations with respect to donor concentration for several dopants. The carrier concentration being roughly proportional the donor concentration to the 1/3 power at levels greater than $1\times10^{18}cm^{-3}$ further suggests that the triple-negative charged gallium vacancy serves as an acceptor in heavily n-type GaAs .

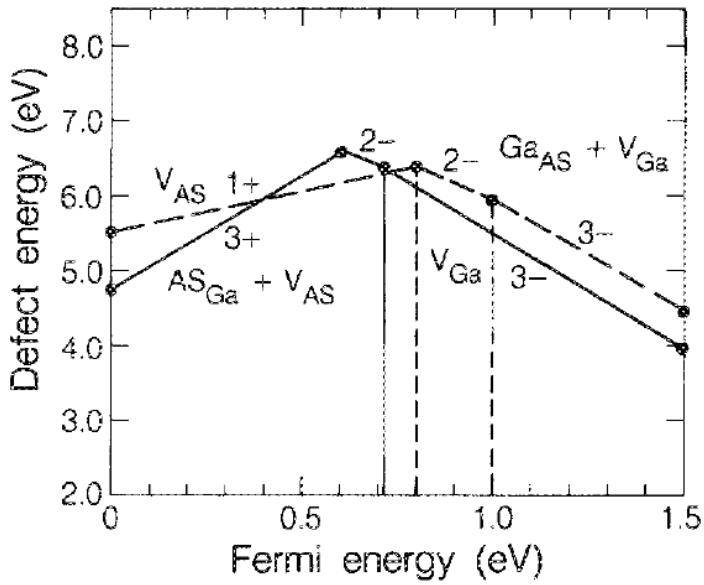

Figure 2-18. Formation energies of defects with respect to fermi level along with their respective charges. Energy maximums are the fermi level stabilization for each defect system[64].

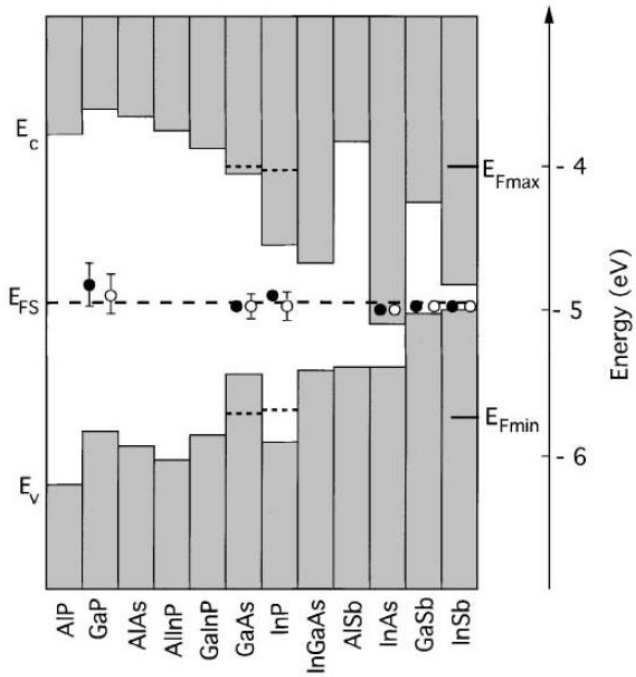

Figure 2-19. Fermi level stabilization energy E_{FS} and band offsets for several III-V compound semiconductors[65].

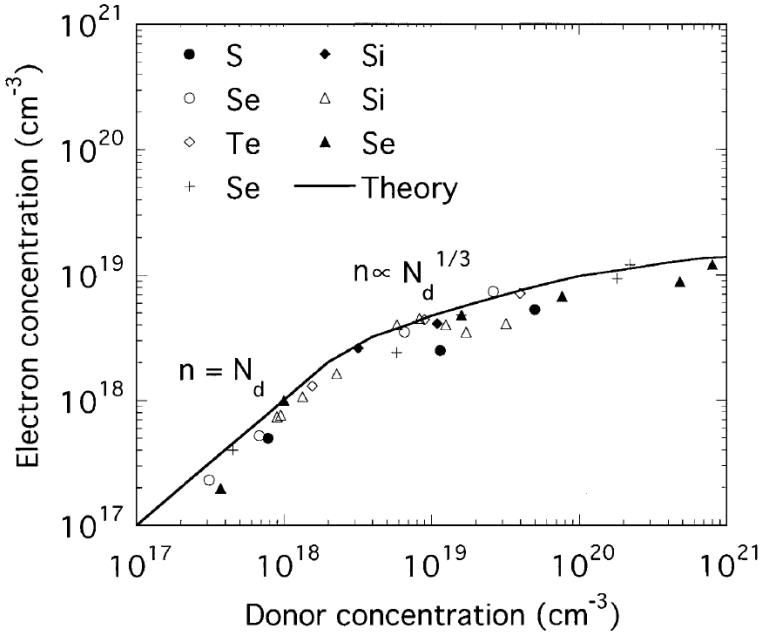

Figure 2-20. Free carrier concentration with respect to donor chemical concentration in GaAs, including both experimental results and the outputs of the Amphoteric Defect Model[65].

CHAPTER 3
PROCESSING AND CHARACTERIZATION TECHNIQUES

There are several techniques used to study dopant diffusion and activation in semiconductors, including imaging, ion-implantation, etching, and pre-thermal processing of treatments and depth profiling. The primary processing methods used in this work was atomic layer deposition (ALD), molecular beam epitaxy, ion implantation, secondary ion spectrometry, and thermal annealing. All of these techniques enabled for the proper preparation, observation and analysis of diffusion and activation data obtained for dopants in InGaAs. Table A-1 specifically includes the growth conditions, layer thicknesses, and doping conditions of the InGaAs samples used in this work.

3.1 Ion Implantation

Ion implantation is a prominent doping technique used to introduce dopant atoms into a material through ion bombardment, and is a significant dopant technique used in this project. The process was invented by Russell Ohl at Bell Labs in 1951. William Shockley then filed a patent for ion implantation three years later in 1954, and was granted the patent in 1957. It has then grown in usage as a central component of semiconductor processing in the several decades since. A basic schematic of an ion implanter is included in Figure 3-1.

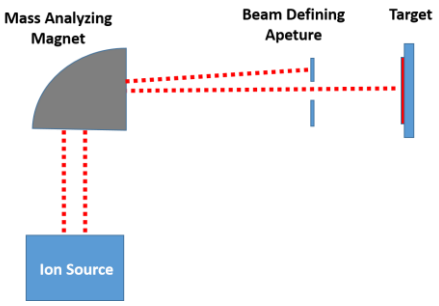

Figure 3-1. Simplified Schematic of an Ion Implanter.

There are fundamentally a few main parts to an ion implanter. The first is the ion source, which contains the species to be implanted. Second is the mass analyzing magnet, which separates the ions of different mass. Third is the beam defining aperture and finally the processing chamber where the target lies. Rastering can be either mechanical in nature, through movement of the sample, or carried out with electrostatic deflection.

Ion implantation is a versatile processing technique to selectively dope active regions of devices, since the specific concentration, depth, angle, and type of implanted ions can be controlled. It has enabled continued scaling through the use of shallower source and drain regions and techniques to prevent short channel effects at smaller nodes, like halo implants. Another benefit of ion implantation is allowing the use of self-aligned gates, where the gate is deposited before implantation of source and drain regions. This allowed for superior alignment and tighter tolerances of source drain and gate, and 40% fewer masking steps in transistors since its invention by Robert Bower in 1969[66].

Ion energies ranging from few eV to several MeV can be used to tailor dopant depth. Ion doses, usually in units of square centimeter (cm^{-2}) can vary significantly. It can be set low enough to avoid substrate amorphization, or can be used to intentionally create electrically-isolated regions, which have been demonstrated for III-Vs[67,68]. If entire regions or wafers are needed to be implanted, the beam can be rastered across the wafer surface for uniform coverage.

3.1.1 Implant Damage and Collision Cascades

Ion implantation is a method to introduce dopants, but has one closely coupled side effect: implant damage. High energy ions that bombard a target invariably transfer

energy into substrate atoms, generating collision cascades. These collision cascades are where several atoms in a lattice are set into motion by an incident atom, and subsequently transfer their energy to surrounding atoms in the lattice. The collision cascade ceases to propagate once the transferred energy is lower than displacement energy of the receiving atom, resulting in a net interstitial. When the dose of implanted ions is high enough, this disruption can even cause whole portions of the substrate material to become amorphous. Heavier ions are known to generate more damage and have shorter projected range than lighter ions at a given implant energy, as shown in Figure 3-2.

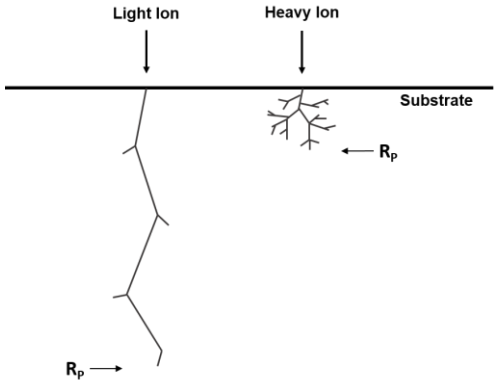

Figure 3-2. Illustration of light vs heavy ions into a material and resulting cascades at a given implant energy.

For III-Vs SPEG regrowth is known to lead to low quality films. Knowing and characterizing the amorphizing limits of a material of paramount importance. Damage threshold density (TTD) is a parameter used to quantify how much damage can occur in a cubic centimeter of material before it amorphizes, as studied by works like that of Jones and Santana[69].

The Giles “plus one” model is common approach to account net generation of defects from ion bombardment. As an ion is implanted, it knocks out atoms from lattice

sites, which ultimately lead to generation of an interstitial at the end of the recoil cascade[70]. In turn it is assumed that the number of interstitials generated from an ion implant is equal to the number of ions implanted into a material, after recombination.

3.1.2 Ion/Substrate Atomic Interactions

Looking at an atomistic level, implanted ions interact with substrate atoms in two ways: nuclear stopping and electronic stopping. Nuclear stopping is a direct or indirect collision of two atoms, while electronic stopping is interaction of a moving atom with the electron cloud of the lattice, which can have a drag-like slowing effect on the ion[71]. Total stopping, and ultimately the ion implanted range can be determined from these two stopping types.

$$\frac{dE}{dx} = -N[S_n(E) + S_e(E)] \tag{3-1}$$

Equation 3-1 is the rate at which energy is lost by an implanted ion in a crystal lattice[34] N is the target atom density, S_n and S_e are the nuclear and electronic stopping power respectively ($eVcm^{-2}$). If we know both the nuclear and electronic stopping power, then we can calculate the range of an implanted ion. Head-on nuclear interactions are commonly approached using two body collision theory. Using a Thomas-Fermi model, the Coulomb potential (V_r) between two atoms can be defined as[72]:

$$V(r) = \frac{Z_1 Z_2}{r} \exp\left(-\frac{r}{a}\right) \tag{3-2}$$

Z_1 and Z_2 are the atomic numbers of the respective interacting atoms and r is the distance between them. The screening parameter *a* accounts for the “blocking” or reduction of the interatomic potential due to screening of inner shell electrons. Firsov approximated this parameter measured potentials with respect to distance and fit using Equation 3-2 above resulting in[73,74]:

$$a = \frac{a_0}{\left(Z_1^{\frac{1}{3}} + Z_2^{\frac{1}{3}}\right)^{\frac{2}{3}}} \tag{3-3}$$

With larger and larger atoms, the screening parameter increases, thereby decreasing the columbic potential between the two atoms. Both nuclear and electronic stopping are events that eventually bring the incident ion and recoiling substrates to rest, resulting in a region of extrinsic point defects and disorder of the lattice.

3.1.3 Dynamic Annealing

Another factor to consider when carrying out ion implantation is the temperature of the substrate during ion bombardment. Dopant diffusion as well as damage evolution, is a temperature-dependent process. Fewer and fewer residual point defects would remain with a higher temperature of implantation, due to the greater mobility of atoms to recombine with generated vacancies. At room and elevated temperatures, this active annihilation of damage during implant is referred to as dynamic annealing, and can lead to acute effects on dopant activation and diffusion.

3.1.4 Channeling

Channeling is another phenomena as observed in ion implanted samples, where a dopant “tail” forms at the end of the doping profile. This is due to implanted ions traversing through openings in a lattice, where they primarily experience electronic stopping, rather than nuclear stopping. Implanting at a random, off axis angle is one method to prevent this, where 7 degrees is a common angle used [24]. Figure 3-3 is an example of ion channeling of Si^+ in InGaAs implanted at 300°C. The substrate retained greater crystallinity during implant, allowing more Si ion to experience electronic stopping in openings in the material, resulting profile broadening or “tails” to occur.

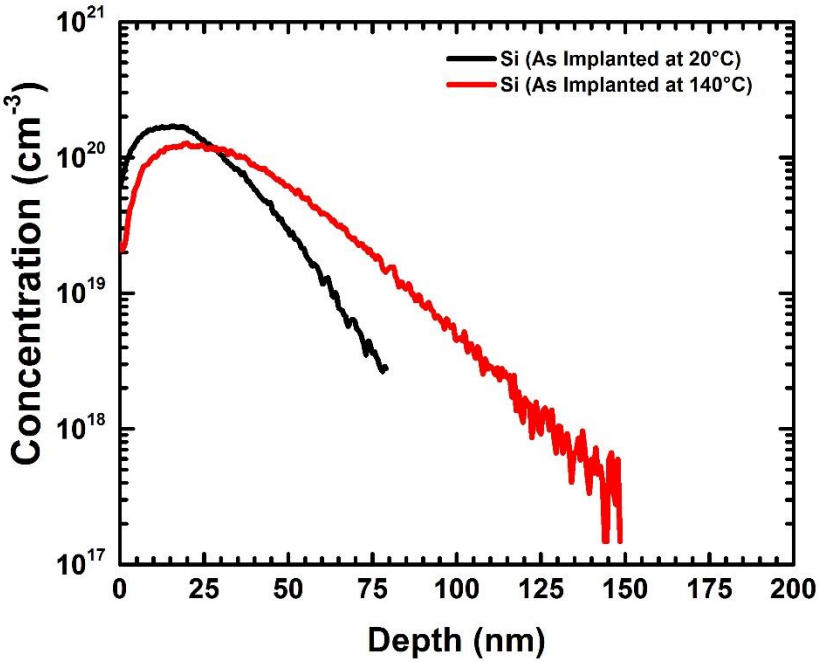

Figure 3-3. Illustration of Ion Channeling in InGaAs implanted with $5\times10^{14}cm^{-2}$ at 300°C.

3.1.5 Dual Pearson Moments for Profiles

A large number of atoms are usually introduced into a material during an implantation, and a set approach can be used to characterize and model the resulting profiles. A semi-empirical dual Person approach has been developed and used to model and predict implant profiles in software package such as PearsonDS or Dupex. The four distribution parameters that were first proposed by Brice and Winterborn in 1975 are: projected range (R_p), straggle (σ), skewness (γ) and kurtosis(β) are parameters that are used[66,75]. Equations 3-4 through 3-8 describe the different moments.

$$R_P = \sum_i \frac{x_i}{N} \tag{3-4}$$

Projected range is the average lateral displacement (x_i) of N implanted ions in the direction perpendicular to the material surface. Often this is in the peak region of the as-implanted curve in a depth profile.

Variance is the average squared difference of an ion and the projected range.

$$\sum_i \frac{\Delta x_i^2}{N} \tag{3-5}$$

Where

$$\Delta x_i = (x_i - R_P)^2 \tag{3-6}$$

Straggling is commonly termed as the standard deviation of the projected range, and is also in units of length.

Skewness is a unitless parameter that indicates which directed a profile is skewed. If skewness is negative, the profile is skewed towards the surface, or positive when the profile is skewed towards the bulk.

$$\gamma = \frac{<\Delta x^3>}{<\Delta x^2>^{3/2}} \tag{3-7}$$

Finally, Kurtosis is a unitless distribution parameter that indicates how broad a distribution tail is for a profile. A Kurtosis of 3 indicates that the profile is a perfect Gaussian, while above this value the profile tails are considered to be broader.

$$\beta = \frac{<\Delta x^4>}{<\Delta x^2>^2} \tag{3-8}$$

In programs like Dupex, there is a fifth parameter that is used to fit channeling tails of profiles, which is usually a fraction between 0-1. If the channeling parameter is set to 1.0, the profile is considered to have no channeling effects.

The majority of implants for this study were completed by Christopher Hatem at Applied Materials. High energy MeV implants into InGaAs were completed by Russel Gwilliam at the University of Surrey Ion Beam Centre.

3.2 Molecular Beam Epitaxy

Ion implantation is the initial and primary method of dopant introduction for the given study. Another doping method is needed that does not have implant-like damage

in order to have clearer, more definite study of fundamental dopant behavior. Molecular Beam Epitaxy (MBE) is a layer by layer method to grow a material with desired dopants in ultra high-vacuum conditions that does not introduce extrinsic concentrations of Frenkel pairs.

The specific conditions during growth, such as temperature, vapor overpressure and fraction of precursors all have an effect on the resulting material quality and composition. Since arsenic is known to outgas, growth of III-Arsenides are commonly done in As_2 overpressure in the growth chamber. This outgassing effect is why several III-V papers consider the As-rich and Ga Rich conditions when accounting for relative abundance of point defects. The integrated amount of dopant grown into a material by MBE is not called a “dose” as this term is usually reserved for ion-implanted species. Despite this, controlling the concentration and thickness of doped layers is of great importance not only for device applications, but for diffusion and activation experiments.

Figure 3-4 is an illustration of the inside of an MBE chamber, where the desired material is grown in ultra high vacuum on single crystal substrate, and the alloying and doping element compositions are closely controlled through the opening and closing of effusion cells over time. Other characterization tools, such as reflection high energy electron diffraction (RHEED) are included inside the chamber to determine material quality during growth.

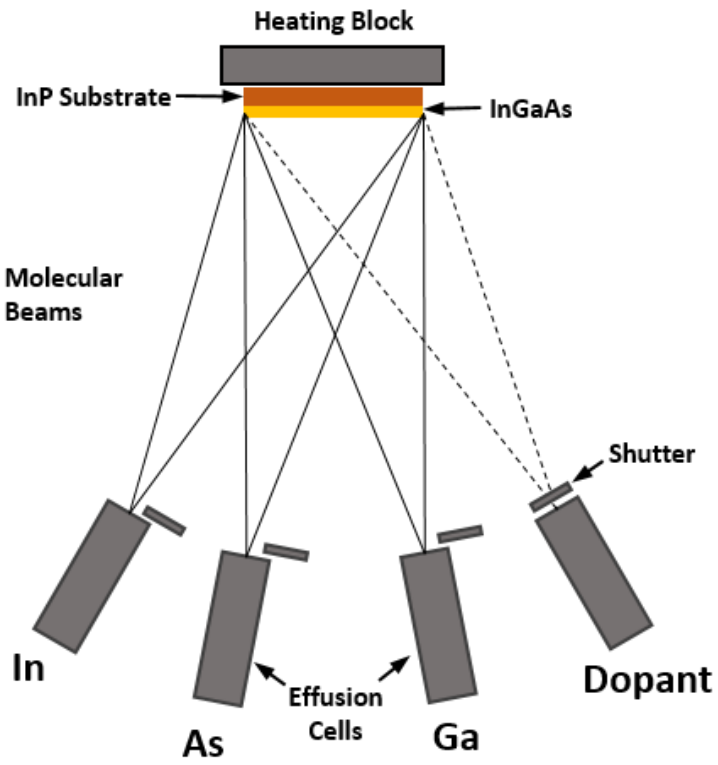

Figure 3-4. Schematic of inside a MBE growth chamber.

In this work, all $In_{0.53}Ga_{0.47}As$ samples were grown by MBE, at the University of Delaware by Cory Bomberger, who is a member of Dr. Joshua Zide research group. A semi insulating InP substrate was used as a substrate. Lattice-matched $In_{0.53}Ga_{0.47}As$ films were grown at 490°C using band edge thermometry at a rate of 0.5-0.8µm hr^{-1} in a 10:1 As:Group III overpressure. Using these samples as a comparison to ion-implanted results helped delineate what dopant behavior was due to the doping process, such as ion implantation, or innate characteristics and limitations of the material.

Another growth method that was used for growth of a minority of the InGaAs samples was metal organic chemical vapor deposition (MOCVD). This method uses organometallics such as trimethylgallium and trimethylaluminum in a hydrogen carrier gas for material growth. A few major differences of MOCVD vs MBE growth conditions

include: higher growth temperatures (700°C vs 500°C), higher chamber pressures, and faster growth rates (0.1um min^{-1} for MOCVD vs 0.01 um min^{-1} for MBE) [76]. It has also been observed that MOCVD grown samples can have significant amounts of residual carbon due to the use of organic precursors.

3.3 Surface Passivation and Degradation Prevention

Before additional annealing techniques are discussed, the importance of surface quality, for III-Arsenides in particular, will be mentioned. Maintaining desired stoichiometry and lack a of stable native oxides of compound semiconductors as mentioned in Chapter 1 complicate the required approach used for thermal processing of these materials. Preservation of the material surface is of paramount importance, as arsenic outgassing was cited as a major issue in this family of materials[77,78].

Interface Defect Densities: III-Vs are known to have significant surface defect densities (D_{it}), which also affect the carrier mobilities, especially with high surface area channels like in FinFETs and nanowires[79]. These defects can cause Fermi level pinning at the surface, making it more challenging to invert the channel with an electric field. As illustrated by Robertson in Figure 3-5, formation energies of specific defects such as cation dangling bonds and As-As dimers is significantly reduced near the conduction band edge.

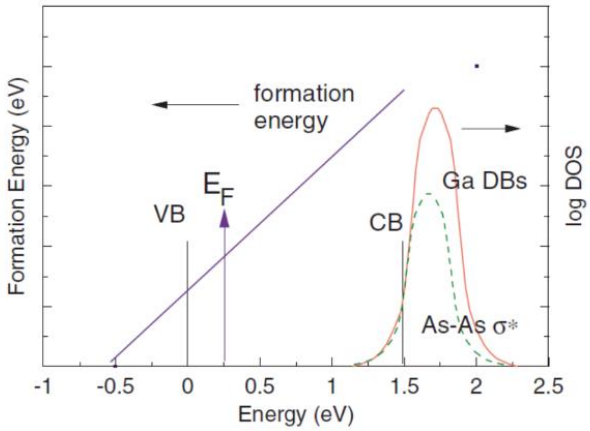

Figure 3-5. Formation energies of Dangling Ga bonds and As-As dimers with respect to fermi level [80].

Researchers have overcome the issue of defect-laden surfaces by passivating the III-V material surface. Examples would include using InAlSb cap for an InGaSb channel device, or a plasma nitride passivation step[81,82]. Another possible method to passivate the surface of III-V materials is through a self-cleaning of the semiconductor surface using atomic layer deposition (ALD) of a dielectric. It has been proposed that this ALD step causes donor traps to be predominant on the surface, which enabled higher drive currents for $In_{0.53}Ga_{0.47}As$ MOSFETs using this approach [83].

For this project, several different capping materials were applied, and compared on which provided the highest quality preservation of the InGaAs surface upon annealing. The caps that were tried, include: GaAs proximity caps, PECVD SiO_2, SiN_x and ALD Al_2O_3. Out of all methods tried, the ALD Al_2O_3 caps provided superior preservation of the InGaAs surface, as shown in Figure 3-6. Pitting was observed for both samples, but this result was considered a worst case scenario, since most processing would not exceed 750°C for the entire project. Unlike PECVD caps, the amorphous alumina cap provided more uniform coverage and is removable with HF.

Al_2O_3 caps 15nm thick were subsequently used for all sample sets to preserve the InGaAs surface during thermal processing. The caps were applied at the University of Florida Nanoscale research facility (NRF), using a Cambridge Fiji 200 ALD in exposure mode at 200°C, with 1.1Å deposited per pulse.

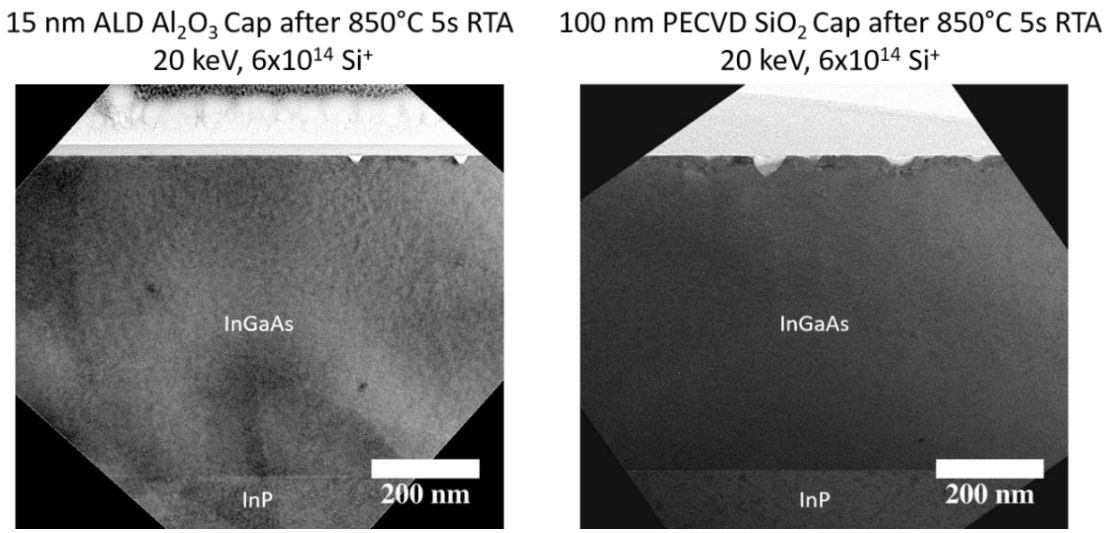

Figure 3-6. XTEM images of InGaAs, comparing surface degradation between 15nm Al_2O_3 (left) and 100nm SiO_2 cap (right).

3.4 Thermal Treatment Techniques

Thermal processing is a needed step which provides dopants the mobility to occupy substitutional lattice sties and enhance activation of a given regions. Also, it is a method to remove any residual damage or disorder generated by ion implantation. Two main methods were used in this work: furnace and rapid thermal annealing, both of which have their own time scales, caveats and methods of successful use. Despite their differences, they both utilize free flowing argon as an inert gas during anneals, to prevent any unwanted oxidation to occur on the InGaAs surface. In addition, all capped sides of interest were place face down onto a carrier wafer to further preserve the InGaAs surface during processing.

3.4.1 Furnace Anneals

Furnace anneals may perhaps be of less industrial relevance at the current cutting edge development at around 14 to sub-10nm nodes, but still retains its fundamental value for better understanding physics and trends of dopant behavior in a material. Furnace anneals were by far the most heavily used for diffusion studies in the project, to observe the long-term characteristics of silicon diffusion. A tube furnace was the one primarily used, with the glass sample boat placed in the middle of the tube. The shortest annealing time used for the furnace was about 10 minutes. As the anneal time becomes shorter than that, the impact of heating and cooling rates is considered to be non-negligible.

3.4.2 Rapid Thermal Anneals

Rapid thermal annealing is more relevant at present since it uses shorter time anneals, ranging from a few seconds to a few minutes, thus preventing dopants from diffusing excessively. Instead of a tube furnace with heating elements, a series of halogen lamps are used to rapidly heat a sample, with the capability of running argon ambient. Figure 3-7 illustrates the relative importance of heat up and cool down rates on furnace and RTP anneals. Since RTAs are generally shorter in duration, the heating and cooling rates play a proportionally larger role on dopant diffusion and activation than in their furnace counterparts. Subsequently these parameters were measured and accounted for in the annealing modelling project. Since cooling is parabolic, this rate was set as a linear fit for the simulations.

Two rapid thermal annealers were used in these studies: an AG Associates Heatpulse 4100 was primarily used for Si-doped samples while a Solaris150 at the University of Florida Nanoscale Research Facility (NRF) was used primarily for Be-

doped InGaAs samples. Both furnace and RTA methods have their imperfections, including accuracy of temperature. A major caveat of the RTA approach is that the thermocouple is usually placed on the back side of a carrier wafer, away from the heat source, and could lead to a read temperature difference between measured and actual. These temperature differences were estimated and taken into account.

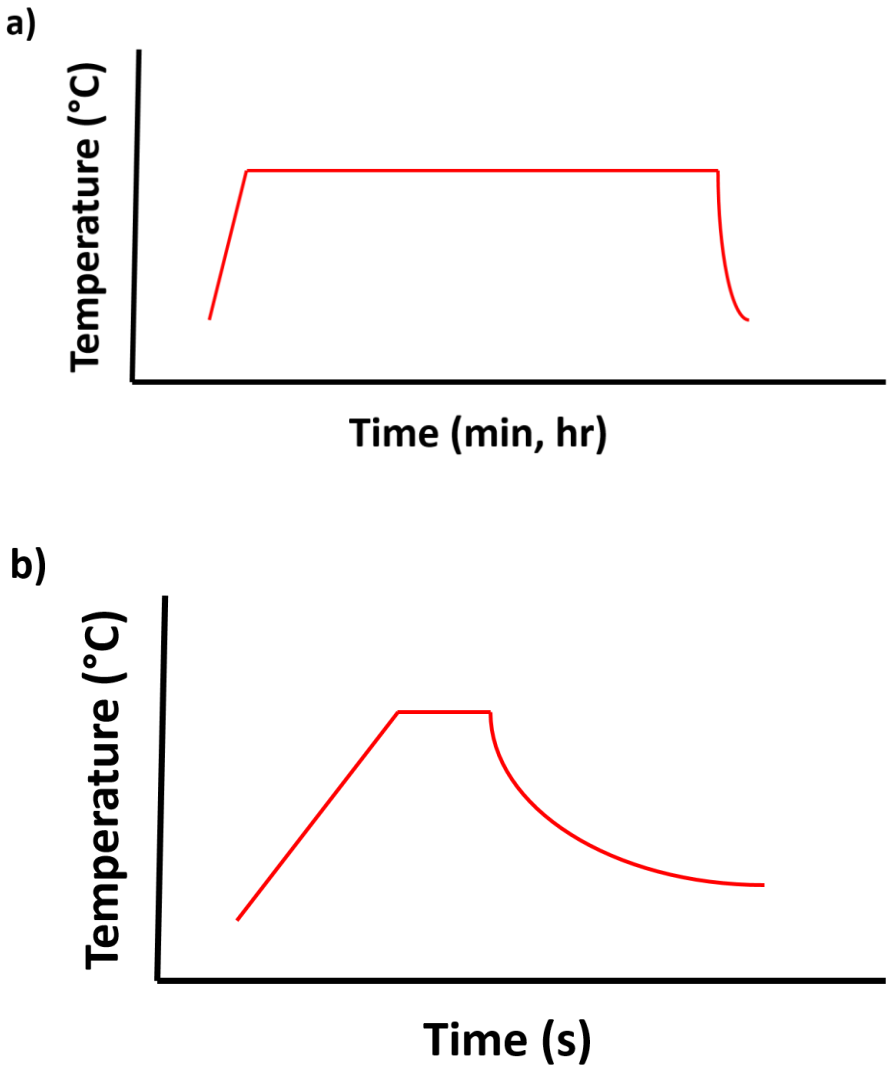

Figure 3-7. Illustration of time vs temperature profiles for a)Furnace Anneal and b)Rapid thermal Anneal.

3.5 Secondary Ion Mass Spectrometry

SIMS is an analytical technique that is used in the microelectronic industry to obtain the composition profile of a sample. It has been commonly used to study diffusion of impurities and has matured toward more widespread use in other fields including identification of organic moelcules[84]. Previous diffusion studies dealt with scales that were on the order of several hundred microns, where capacitance-voltage (C-V) measurements alone were considered adequate for measuring the presence activation and redistribution of dopants in a medium upon thermal processing. Currently even migration of a few nanometers are of critical interest in device design and manufacturing. SIMS is a high-sensitivity technique that can detect concentrations down to part per million of impurities. It can also resolve down to 1-2 nm spacial resolution, which is still relevant at the semiconductor industry at present. Due to the use of sputtering, exact site occupation of species are not determined with this analytical technique. Despite this one caveat, SIMS profiling, along with experimental activation data, is an indispensable resource for modelling development in this project.

The principle of SIMS involves sputtering of the sample with an ion beam, usually either oxygen or cesium ions at 5-10keV in ultra-high vacuum, usually $1x10^{-9}$ Torr. Certain sputtering primary ions provide greater sensitivity of given elements to be analyzed, and is largely dependent on the charge state of the resulting secondary ions[85]. Cesium ions are used to obtain negatively charged secondary ions, while oxygen ions are used to obtain positively charged secondary ions. The resulting ions are directed with an electric field to a mass spectrum analyzer and are separated using a mass charge ratio of the ions, and then reach a detector. Figure 3-8 is a schematic of a typical dynamic SIMS setup, and Figure 3-9 illustration of sputtering of the sample.

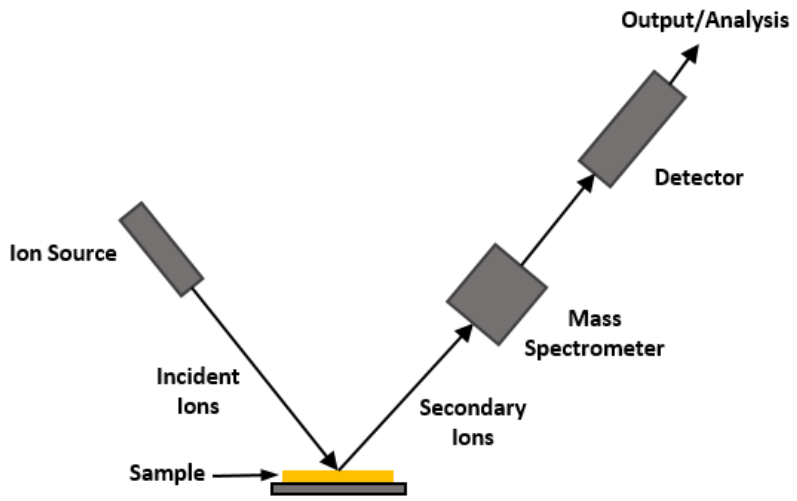

Figure 3-8. Simplified schematic of a SIMS setup.

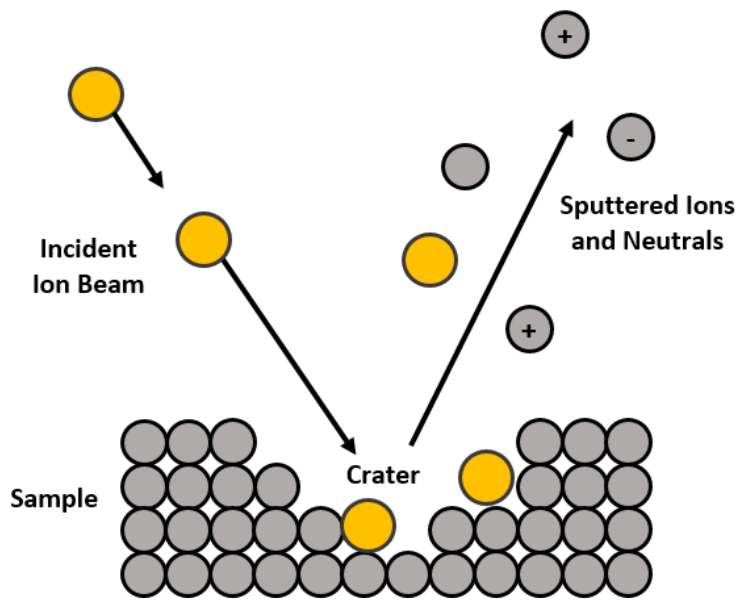

Figure 3-9. Close-up illustration of crater sputtering during dynamic SIMS.

3.5.1 Static SIMS

There are two major operation modes of SIMS: Static and Dynamic. Static SIMS is used to determine the composition of sample surfaces, usually affecting only the top monolayer. Static SIMS uses a very low ion dose and current densities, where the top monolayer could have a lifetime of several hours under bombardment[86]. Unlike dynamic SIMS, the size of the primary ion has a major effect on the reading, due to the

fewer number of ions bombarding the sample surface. Despite lack of depth profiling capability static SIMS is a valuable tool in determining composition at the surface nondestructively.

3.5.2 Dynamic Time of Flight SIMS

Dynamic SIMS also is affected by the specific incident ion species, but a lesser extent than static SIMS. Dynamic SIMS is a destructive technique that obtains a depth profile through sputtering of a sample surface, generating a crater. Time of Flight (TOF) SIMS is when sputtered ions are accelerated and then collected in a detector. The time the ions arrive at the detector indicate the respective species from the material based on their mass. Lighter ions arrive faster, and while heavier ions or clusters take longer to arrive. Dynamic SIMS involves generation of a crater in the sample, and a slew of parameters must be monitored and set correctly for proper attainment of data, as shown in the flowchart included in Figure 3-10. Ultimately, the goal is to obtain species concentration with respect to depth, but requires conversion of counts per time using profilometry, known sputter rates, and known standards.

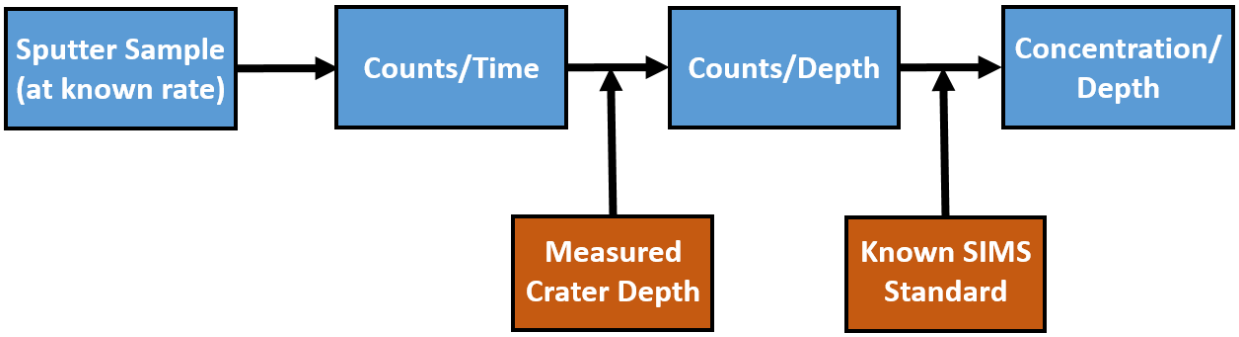

Figure 3-10. Flow diagram of obtaining depth vs concentration profiles of a sputtered species in SIMS.

Possible issues with Dynamic SIMS: Some issues that can occur with SIMS depth resolution is surface roughness, which is induced by sputtering. The shape of the crater being sputtered can distort the depth profile acquired as illustrated by Hu in

Figure 3-11[87]. The bottom of the pit is the output for a given time during sputtering. When asymmetrical craters are formed, less of the actual bottom of the crater would register, leading to a broadening of the profile towards the sample surface.

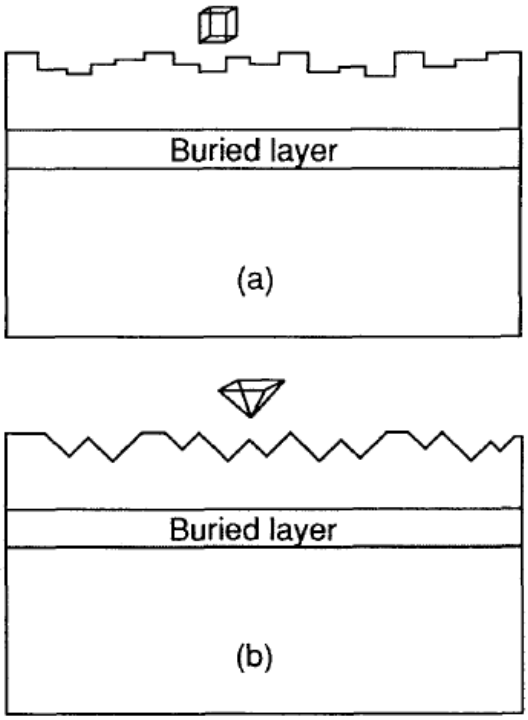

Figure 3-11. Schematic of pit geometry, where symmetrical pits lead to symmetrical outputs, while non symmetrical pits leads to distortion of resulting profile[87].

Another issue to take into consideration is the possibility of knock-on damage, which leads to the broadening of otherwise steep profiles. Figure 3-12 illustrates how the Si doped InGaAs/non doped InGaAs interface deeper in the bulk is experiencing knock-on damage, where Si is being knocked deeper into the material due to the incoming sputtering ion and registered there instead of their actual unsputtered locations. Substrate and ion-specific models have been developed to correct the effect of knock-on damage on generated SIMS outputs. A method to mitigate distortion due to surface roughness and knock on damage is to lower the sputtering energy, and adjust the angle of primary ion bombardment.

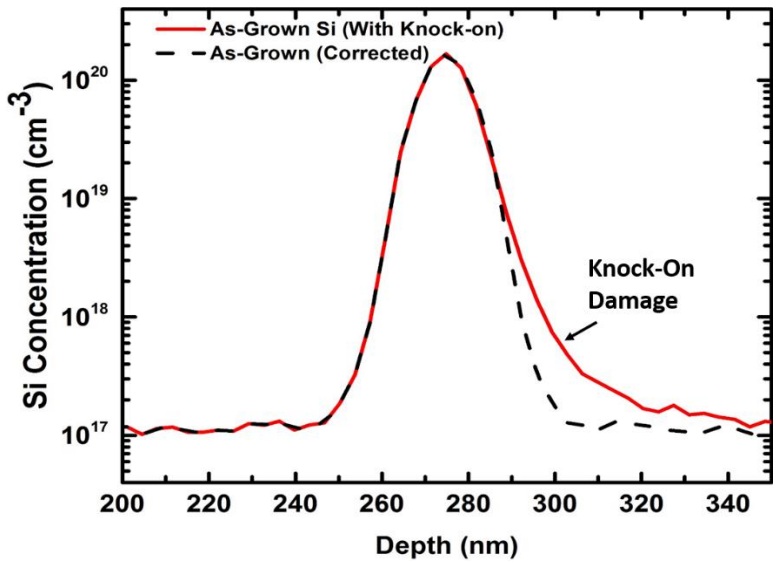

Figure 3-12. Illustration of SIMS knock-on damage caused by ion sputtering.

3.5.3 SIMS standards and Relative Sensitivity factor

As shown on Figure 3-10, a standard is needed in order to obtain actual concentrations of a given species in a material via SIMS. An ion- implanted sample is often used, since the depth and concentrations in a material are usually known. The relative sensitivity factor (RSF) is a primary ion and substrate dependent value used to convert ion signal to a concentration for a given matrix of a known composition. If the RSF for a given matrix/impurity pair is known, and the counts of each species are collected, a concentration of that given element can be estimated. The concentration of an impurity C_E is given by[88]:

$$C_E = RSF \frac{I_E}{I_M} \tag{3-9}$$

Where I_E and I_M are the intensity of counts for the impurity and the matrix species respectively. Different RSFs for different impurities and substrates can be obtained from literature or use of sample standards.

The vast majority of SIMS for the studies of this work were carried out by Evans Analytical Group (EAG). The primary ion commonly used was a 350eV Cs^+ ion beam to sputter the samples. A small number of SIMS were also carried out at the Materials Characterization Facility at the University of Central Florida. These samples were a part of the Be marker layer study as described in Section 4.3.3. A 3keV Cs^+ ion beam was used for sputtering this set of samples.

3.5 Hall Effect

It is of great importance to measure activation, to determine which processing conditions lead the greatest net Si activation. A primary method used was Van Der Pauw Hall Effect, which can determine carrier type, mobility and active sheet number of carriers (cm^{-2}) in a given sample. The basis of Van der Pauw Hall effect involves use of four equally spaced probes that have ohmic contact with a sample, which ideally is a perfect square. Figure 3-13 is a diagram of a typical Van Der Pauw Hall effect setup.

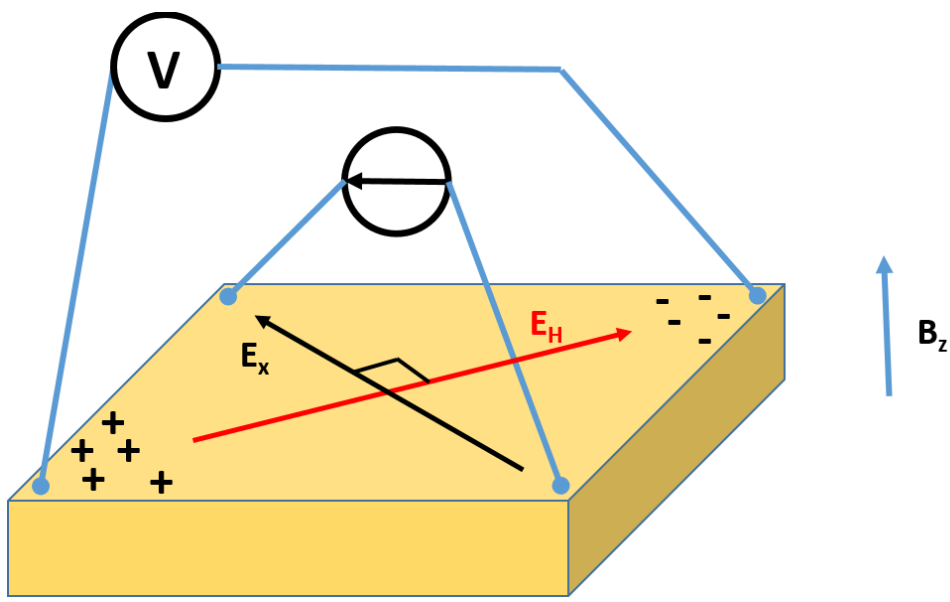

Figure 3-13. Illustration of Van Der Pauw Hall Effect.

Current is passed through one pair of contacts, while voltage is measured through the other pair. Average resistance is calculated using the Equation 3-10 below, where the voltage drop along one pair corresponds with the current of the other pair for the calculation of a given resistance[89]:

$$R = \frac{1}{4}\left[\frac{V_{12}}{I_{34}} + \frac{V_{23}}{I_{41}} + \frac{V_{34}}{I_{12}} + \frac{V_{41}}{I_{23}}\right] \tag{3-10}$$

Where the numbered subscripts correspond to the voltage or current the respective pair of contact points. While sheet resistance R_s is calculated by:

$$R_S = \frac{\pi}{\ln(2)} F(Q) R \tag{3-11}$$

F(Q) is a correction factor for geometry of the sample. If the probes are placed on four corners of a perfect square, then this value is one. When a magnetic field is applied to a particle with charge *q* at a velocity *v*, the particle experiences a Lorenz force F[14].

$$F = qv \times B \tag{3-12}$$

In the case of electrons, the Lorenz force would push the electrons in the negative y direction. Accumulation of negative charge at the top right and positive charge at the bottom left of sample generates a Hall field E_H perpendicular to the electric and magnetic fields. At equilibrium the resulting Hall Field and hall Field would be equal to the magnetic field force in the negative y direction, preventing further accumulation of electrons.

$$E_H = \left(\frac{1}{en}\right) J_x B_z \tag{3-13}$$

When the given current, magnetic field and electric field in y direction are known, the carrier concentration of the sample can be calculated.

$$R_H = \frac{E_y}{J_X B_Z} = -\frac{1}{en} \tag{3-14}$$

Conversion of Measured Sheet Numbers to electrical solubility: It is important to note that additional steps were used for calculating the actual peak activation of dopants in a material for this project. The sample thickness was a set value in the Van Der Pauw setup, and produced a sheet number (cm^{-2}) for each sample. Corresponding SIMS data and a mathematical solving package was used to calculate electrical solubility (cm^{-3}). A program was written to input a SIMS profile, a guessed maximum solubility limit, and integrate under that concentration of the profile. The max solubility was then guessed iteratively until the integrated area was equal the measured sheet number from Hall effect. The process is visually illustrated in Figure 3-14.

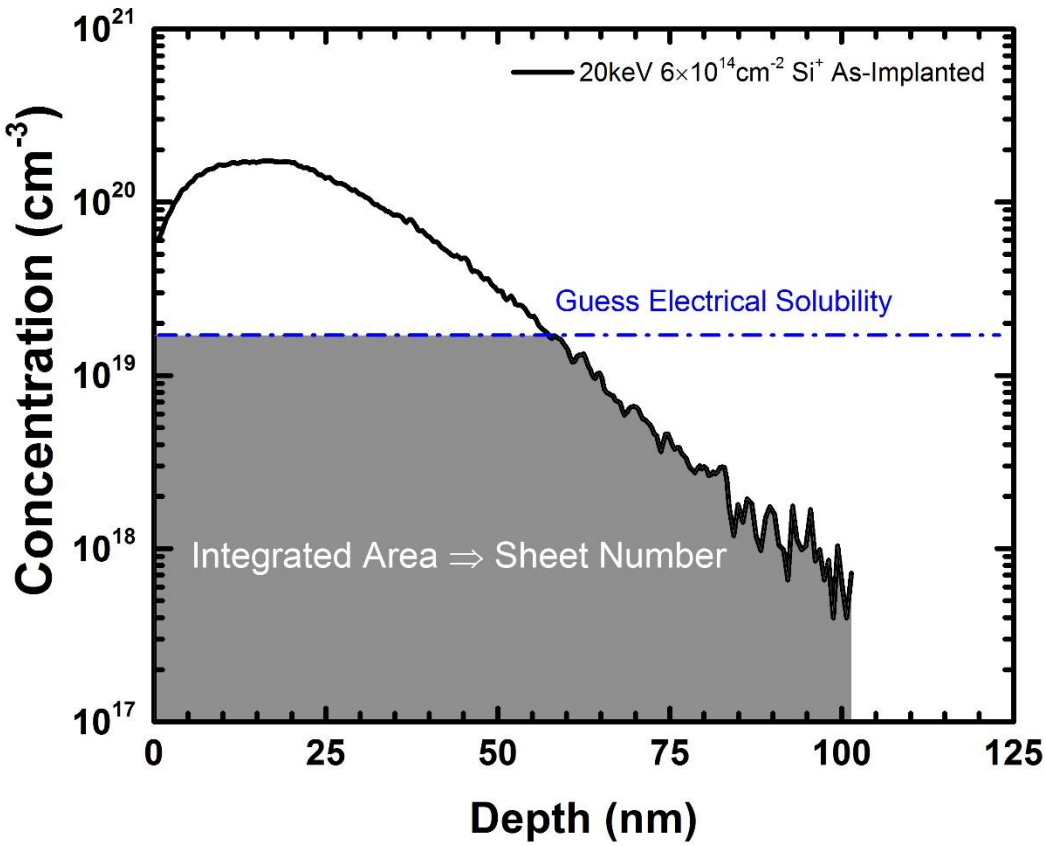

Figure 3-14. Illustration of Integration method used to obtain electrical solubility from measured sheet numbers[90,91].

CHAPTER 4
EXPERIMENTAL RESULTS

4.1 Activation Studies of Si^+ in InGaAs

4.1.1 Effect of Implant Temperature on Si^+ Activation

Initial work involved measuring activation of ion implanted Si into InGaAs and better understanding the right conditions to maximize activation. As discussed in Chapter 3, this doping method comes with its own set of characteristics upon thermal processing, most notably the implant damage introduced. One of the major takeaways from these preliminary studies indicates that implantation temperature plays a major role. Prevention of amorphization was a high priority, since SPER of III-Vs can lead to regrown material of poor electrical and crystalline quality [67,92]. As shown in Figure 4-1, implantation at 80°C obtained significantly greater activation and lower sheet resistances than lower (20°C) and higher (140-300°C) implantation temperatures. Figure 4-2 illustrates the amount of residual damage of each implantation- indicating that the sample implanted at 20°C was amorphized, while the higher temperature implants have better crystallinity. This “sweet spot” in activation at 80°C could be attributed to a combination of more crystalline damage while also avoiding amorphization, allowing more vacancies into which Si can activate[90].

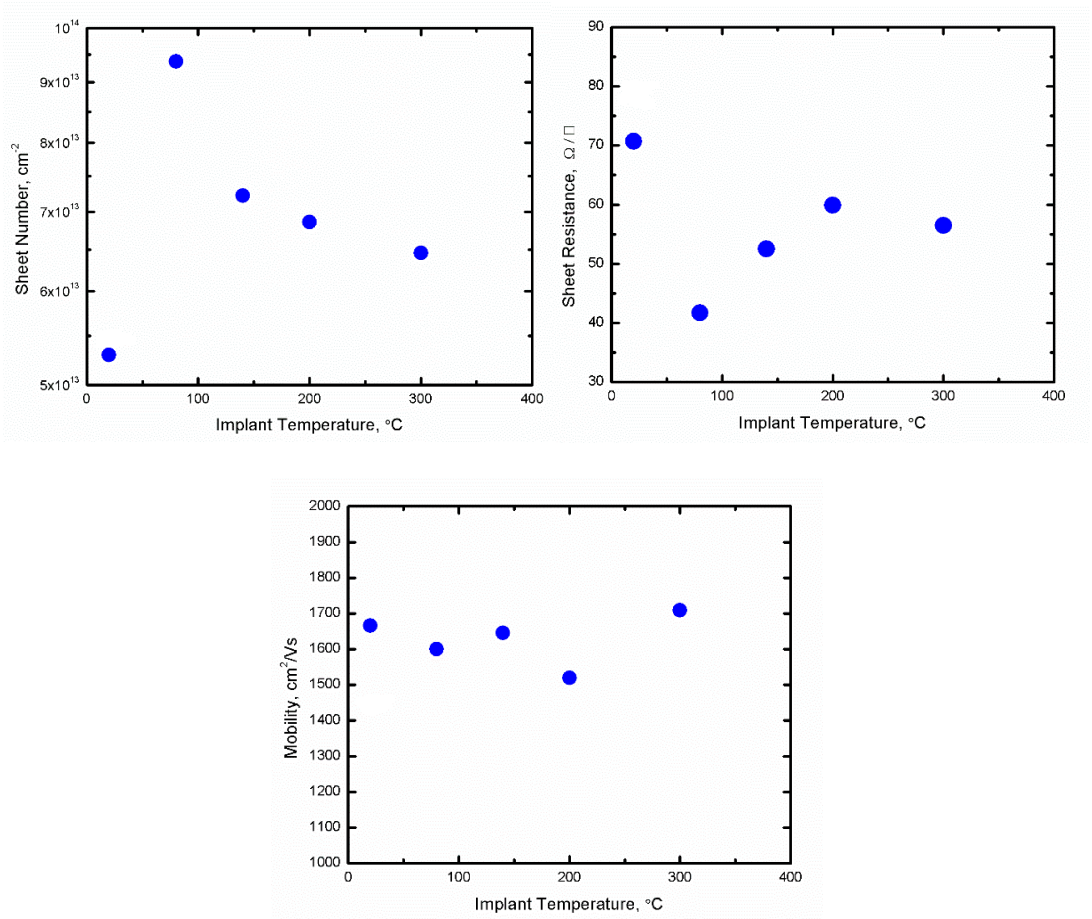

Figure 4-1. a)Sheet number, b)sheet resistance and c) mobility of InGaAs following a 20 keV, 6×1014 cm^{-2} Si^{+} implant after 750°C, 5s RTA.

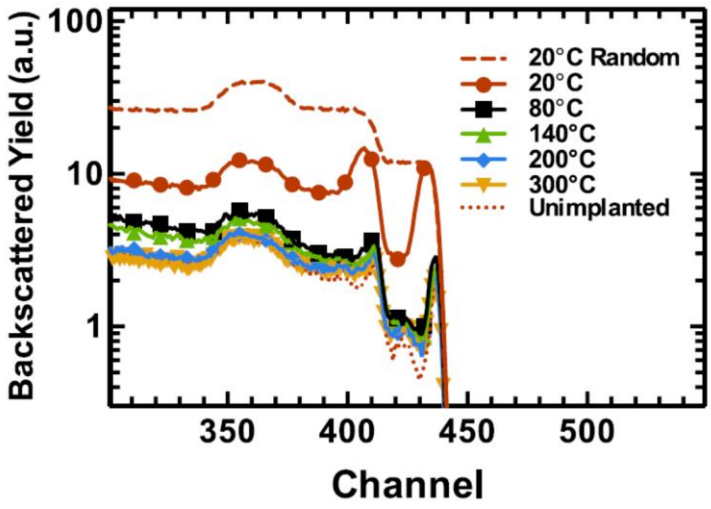

Figure 4-2. RBS/C spectra showing the backscattered yield versus channel number for $In_{0.53}Ga_{0.47}As$ specimens Si^{+} implanted at 20 keV to a dose of 6.0×10^{14} cm^{-2} at implantation temperatures of 20–300°C.[90]

4.1.2 Implant Temperature Effect on Amorphization and Extended Defect Evolution

It is known that solid phase epitaxial growth (SPEG) in III-Vs are of lower quality than elemental semiconductors, therefore should be avoided. An amorphous layer ranging from 14-30nm was observed to consistently form in InGaAs implanted with 20keV $6\times10^{14}cm^{-2}$ Si^{+} at 20°C. A set of elevated-temperature implants ranging from 20-300°C were then carried out with same silicon implant dose and energy to determine the minimum required temperature to prevent amorphization[90]. XTEM images of the ion-implanted smaples in Figure 4-3 indicate that formation of an amorphous surface layer was prevented when implanted at 80°C.

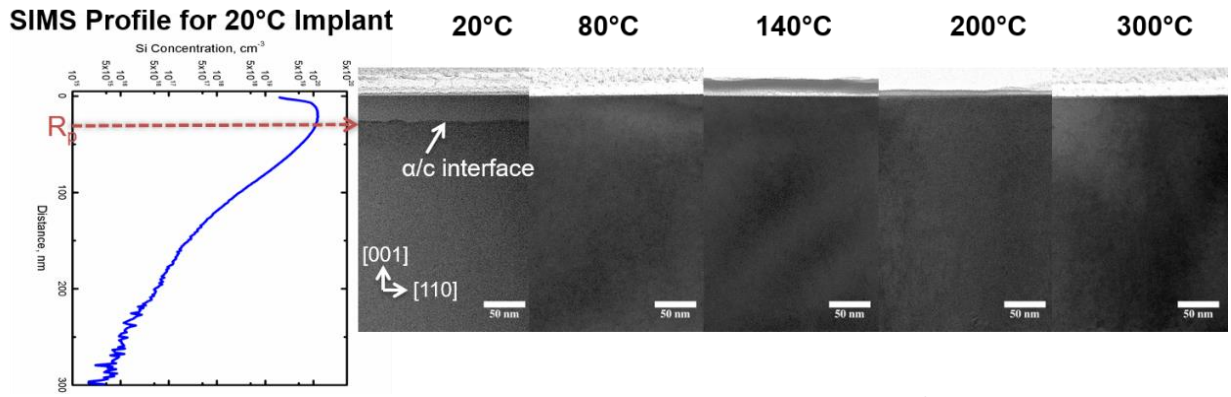

Figure 4-3. XTEM images of InGaAs implanted with Si 6×10^{14} cm^{-2} 20keV implanted between 20-300°C. SIMS Profile of as-implanted Si is included for comparison.

Extrinsic interstitial loops have been observed upon thermal annealing of ion-implanted InGaAs, but are considered less stable than their silicon counterparts. In this project most loops have been observed to dissolve with a thermal budget greater than 5s 750°C. A set of samples implanted with Si at different temperatures were subsequently annealed in RTA to determine the implantation temperature with the least extrinsic defects. Figure 4-4 indicates that InGaAs ion implanted at 80°C had fewer extrinsic loops than that of higher temperature implants.

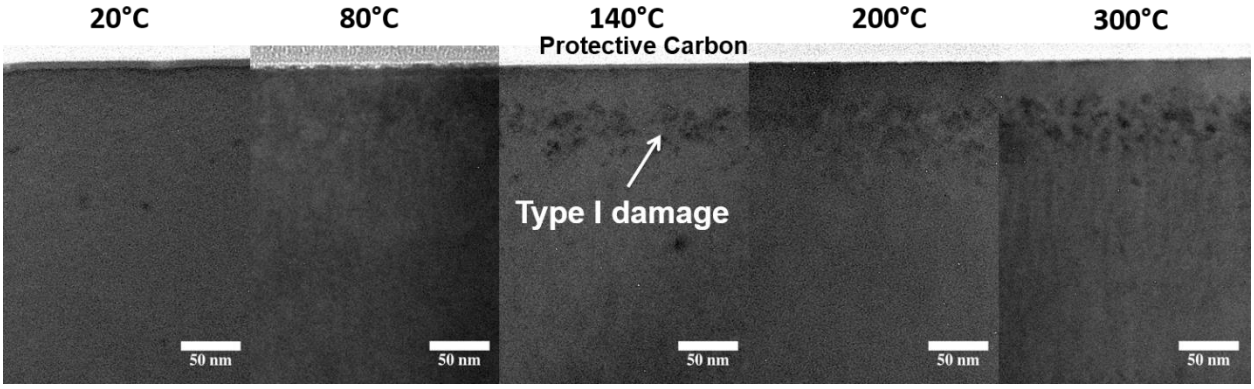

Figure 4-4. XTEM images of InGaAs implanted with 6×10^{14} cm^{-2} 20keV Si^{+} dose between 20-300°C, then annealed at 750°C for 5s.

4.1.3 Implant Dose Effects on Si^{+} Activation

Activation of varying implant dose is shown in Figure 4-5. A deviation from 100% activation became more pronounced with increasing dose, likely due to increased compensation, either from defects generated through fermi level effects, or Si occupying anion lattice sites. Most implant doses for subsequent studies were $5\text{-}6\times10^{-14}$ cm^{-2} as an upper limit to prevent amorphization of the InGaAs surface.

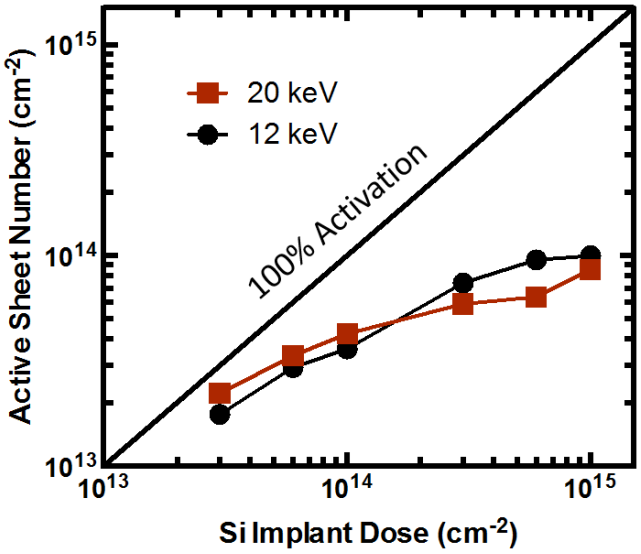

Figure 4-5. Sheet number with respect to Si implant dose following a 750°C, 5s RTA.

4.1.4 Implant Energy Effects

Usually with higher implant energy at a given dose, the Si activation was increased compared to lower energy implants, while mobility decreased as expected for larger doses, shown in Figure 4-6. This is likely due to the fact that, at higher implant energies, the implanted dose is spread over a larger region, providing additional lattice locations for the implanted species to activate. Also in line with constant implant dose results, activation was consistently higher for the 80°C substrate temperature.

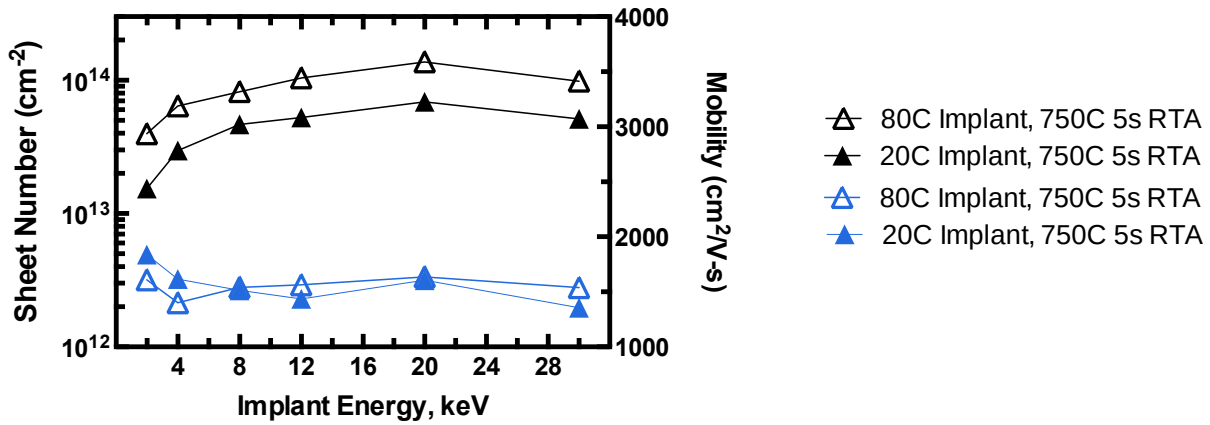

Figure 4-6. Measured Sheet number (black) and mobility (blue) vs Si^+ implant energy into InGaAs for both 20°C and 80°C implant temperatures.

From the several exploratory experiments, ideal parameters were found to obtain the highest activation of ion-implanted Si in InGaAs. A “sweet spot” of 80°C obtained a peak active concentration of ~$1.710^{19}cm^{-3}$, regardless of annealing temperature and time as illustrated in Figure 4-7.

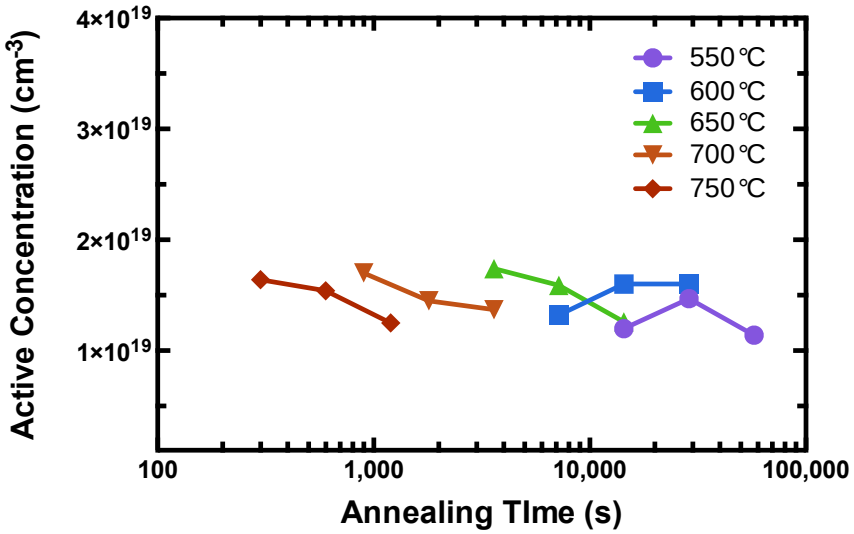

Figure 4-7. Calculated Peak carrier concentrations using hall effect data for 10 keV, 5×10^{14} cm^{-2} Si^{+} implanted at 80°C then annealed at 550-750°C for various times.

4.1.5 MBE, Grown-in Si Activation Results

Ion-implanted InGaAs had shown consistent activation results, leading to electrical saturation with a large enough thermal budget to anneal out initial disorder. Additional studies were carried out with MBE doped InGaAs, to better understand the fundamental diffusion and activation behavior or Si in InGaAs, eliminating the damage that is invariably linked with implantation.

Activation of Si for MBE doped InGaAs were significantly higher than our commonly converged value observed upon annealing implanted samples, with a net carrier concentration of $2.4\times10^{19}cm^{-3}$. For MBE doped samples, a deactivation trend was consistently observed, where net activation values decreased to $1.7\times10^{19}cm^{-3}$. These results indicate that grown-in doping higher than converged levels are metastable as shown in Figure 4-8.

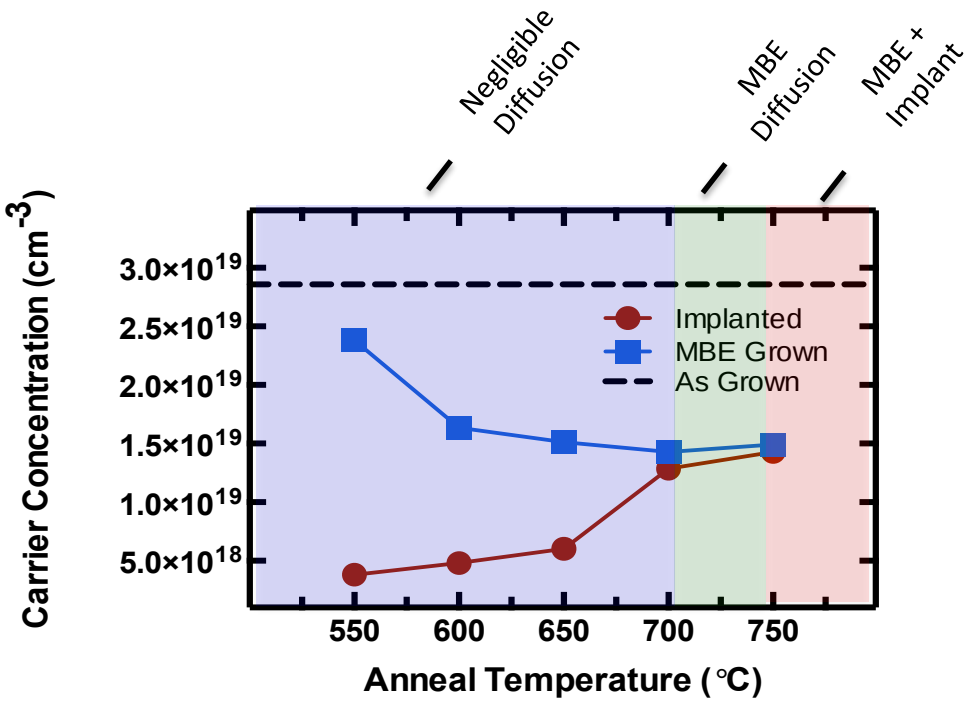

Figure 4-8. Calculated electrical solubility of Si in ion-implanted and MBE doped InGaAs, after 10min anneals ranging from 550 through 750°C.

Complimentary SIMS profiles of both Implanted and MBE-grown samples in the study by Lind et al. are included in Figure 4-9 below[93]. It is important to note that the regimes where there is little to no diffusion is when there is significant activation or deactivation, while when silicon is moving appreciably, the activation is nearly converged.

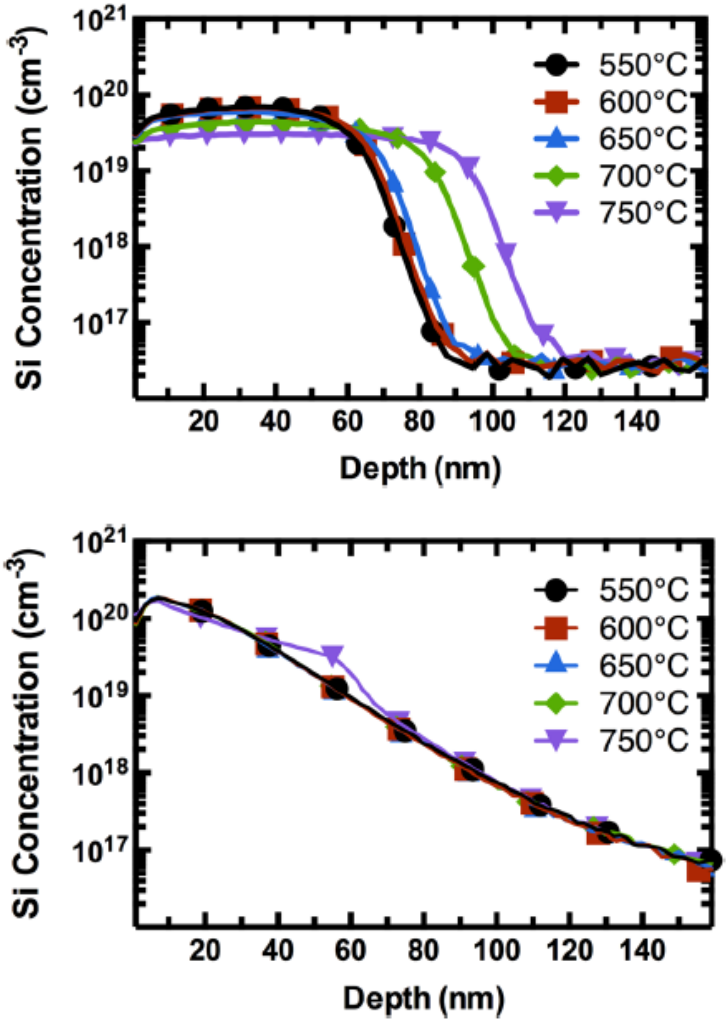

Figure 4-9. SIMS profiles of MBE doped (left) and $5\times10^{14}cm^{-2}$ 10keV Si^{+} implanted (right) InGaAs before and after10min anneals ranging from 550 through 750°C[93].

4.1.6 Co-implant Study

Given that inherent activation limits have been observed with Si as the sole dopant for both implanted and MBE grown InGaAs, co-implantation was explored in an attempt to overcome this limitation. Past work suggested that co-doping enhanced activation of carbon-doped InGaAs with two distinct atoms would cause both to preferentially occupy certain sites, both activating, and preventing amphoteric behavior[94]. Another group suggested that by implanting with Al, enhanced SI activation[95].

Ultimately, this was not observed for a comprehensive co-implantation study under this task, as the activation results were not additive[96]. Figure 4-10 shows the expected trends to be observed with co-implanting InGaAs, and Figure 4-11 presents the experimental results. These results indicate there is not a strong preferential occupation of lattice sites that occur when co-doping via ion implantation. The activation increase is not drastic, and implant order (for P^+ and Si^+ co-implantation) does not improve activation.

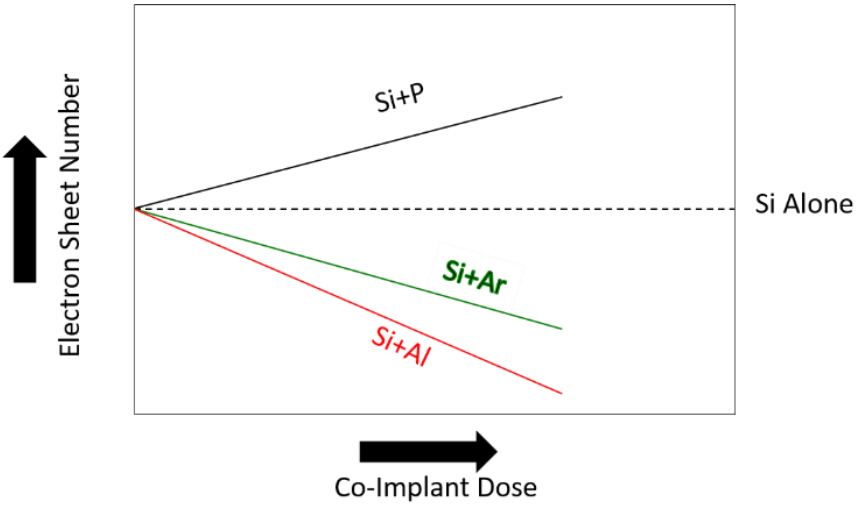

Figure 4-10. Expected co-implant activation trends with increasing co-implant dose.

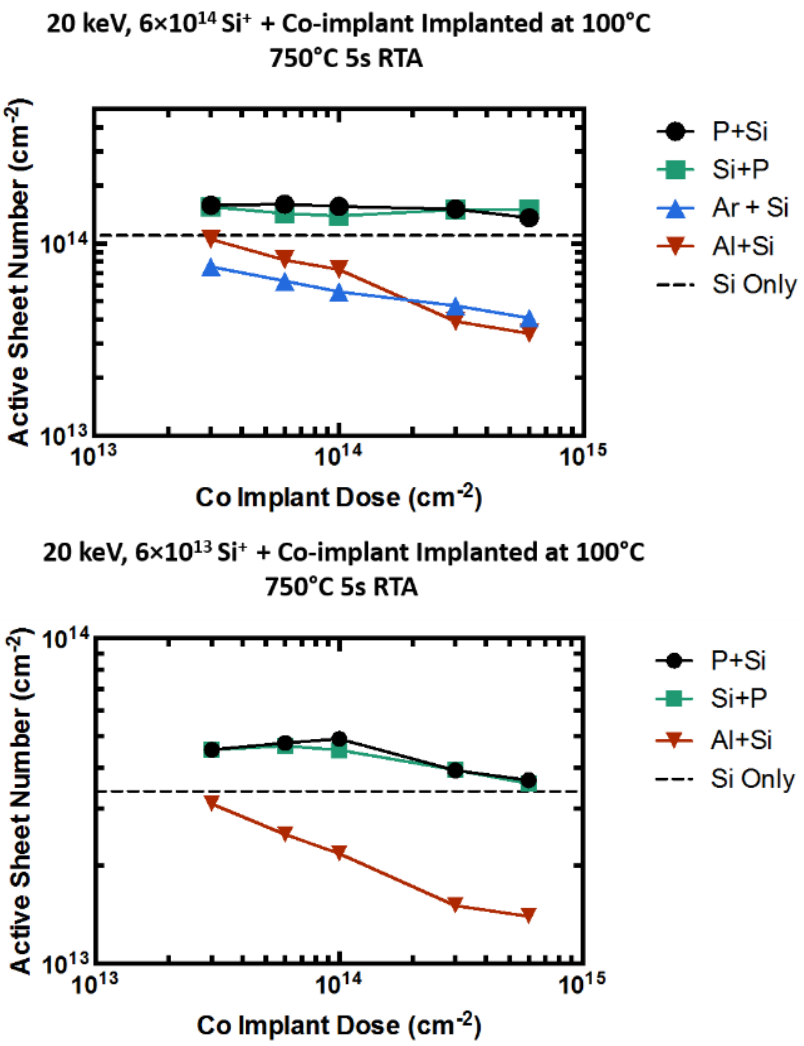

Figure 4-11. Measured Sheet number vs co-implant dose for a) $6\times10^{14}cm^{-2}$ and b) $6\times10^{13}cm^{-2}$ Si^{+} implant annealed for 5s 750°C.

These results clearly differ from previous co-implant studies in III-Arsenides, where significant % activation improvement was reported. A few major difference between this current work and previously reported co-implant work are the implant energies and doses used. Lower implant energies (20keV vs several hundred keV) and generally higher (6×10^{13}-6×10^{14} vs 1×10^{14} and below) lead to higher as-implanted doping concentrations and higher concentration net defects. In line with the compensating defect model, these higher doping regimes lead to the formation of cation

vacancies that have a stronger impact on net activation at these higher concentrations than any possible site preferences that may exist.

4.2 Ion-Implanted Diffusion Results

4.2.1 Ion-Implanted Si Diffusion Studies- Furnace and RTA

Activation was the initial and primary focus of this work, in light of previous literature reporting that Si diffusion is negligible in InGaAs. Upon observation of rapid diffusion from SIMS data, characterizing this diffusion phenomena became a major point of interest and focus for the project. Ion channeling is very pronounced for ion implanted InGaAs, as illustrated from Figure 4-12a, where displacement of ~21 nm was observed for an identical implant dose and energy but with substrate implantation temperatures ranging from 20-300°C.

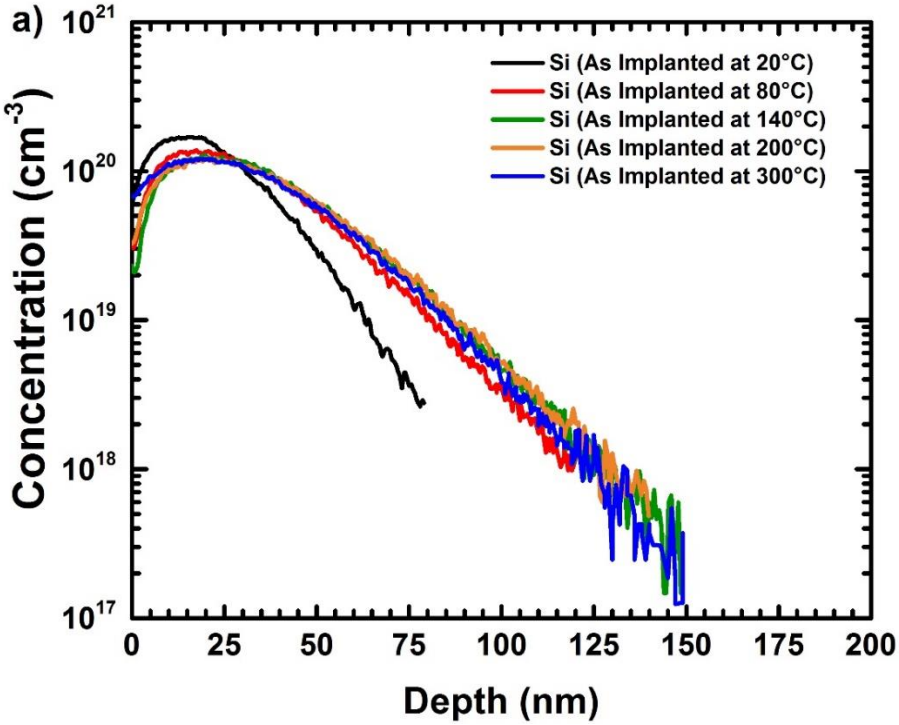

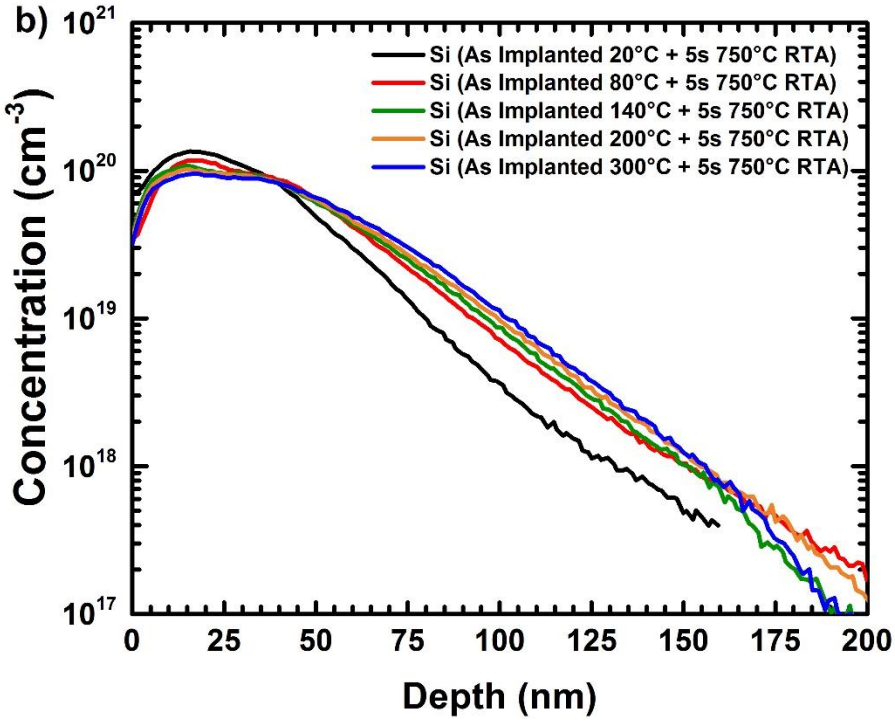

Figure 4-12. SIMS profiles of 10keV 5×10cm^{-2} Si^{+} in InGaAs a) As implanted, b) Post 5s 750°C RTA for SI implants ranging from 20-300°C.

Exponential-like profile broadening shown in Figure 4-12b and 4-13 was observed when the respective samples were subsequently annealed at 750°C for 5 seconds. A likely mechanism for this this initial behavior is a result of significant channeling that was observed for as-implanted samples. Those very implanted silicon ions that helped constitute the implant “tail” likely continue to diffuse interstitially until a substitutional site is available.

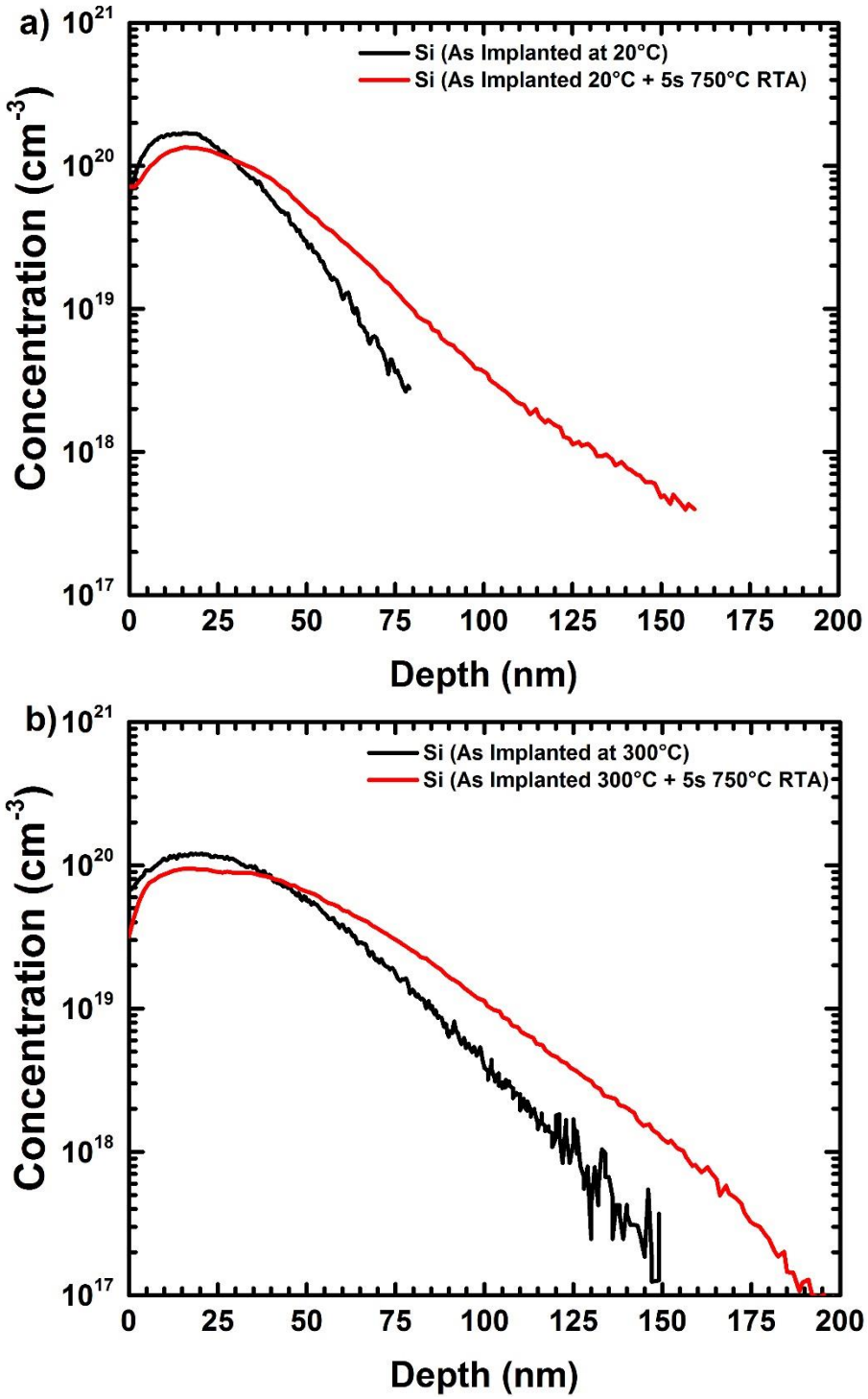

Figure 4-13. As-implanted and post anneal SIMS profiles of 10keV 5×10cm^{-2} Si^{+} in InGaAs for a)20°C implant and b) 300°C Implant.

4.2.2 Diffusion Studies – RTA and Furnace Anneals

Upon longer diffusion times starting at 10s, sharp shouldering profiles evident of concentration-dependent diffusion were observed. Figures 4-14 and 4-15 illustrate this fact with longer time RTAs and furnace anneals. Concentration-dependent behavior was observed up to the furnace anneals with the greatest thermal budgets, suggesting that this is a distinct diffusion regime that occurs after the initial tail-broadening regime. When quantifying the ion-implanted silicon diffusion using the fitting parameter model, the decrease of diffusivity with anneal time was not considered significant enough to be transient enhanced diffusion, where diffusivity would characteristically drop several orders of magniture[97]. The Fickian and concentration-dependent components of the diffusivities extracted using the scaling factor model as described in Section 5.4.6 is displayed in Figure 4-16.

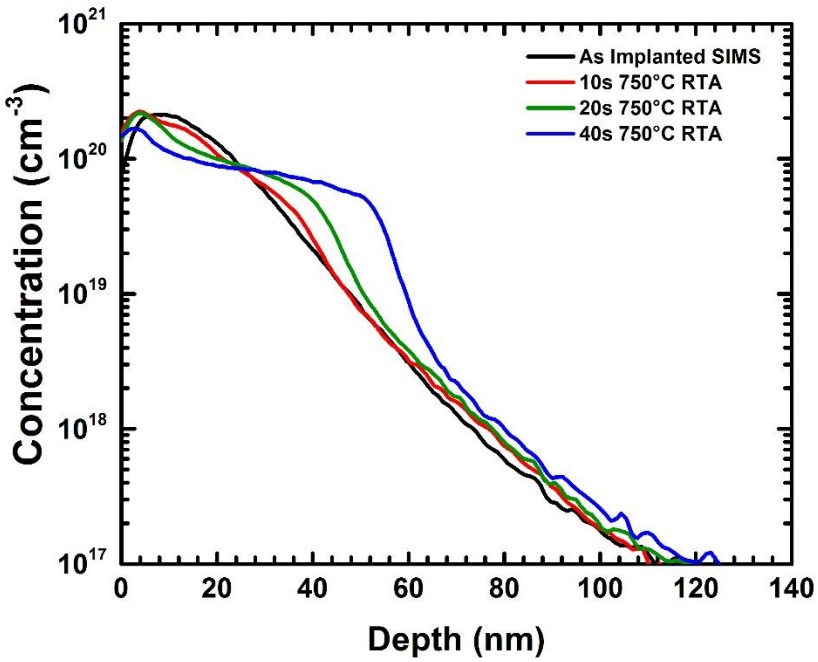

Figure 4-14. As-implanted and RTA SIMS profiles of 10keV $510^{14}cm^{-2}$ ion-implanted silicon in InGaAs.

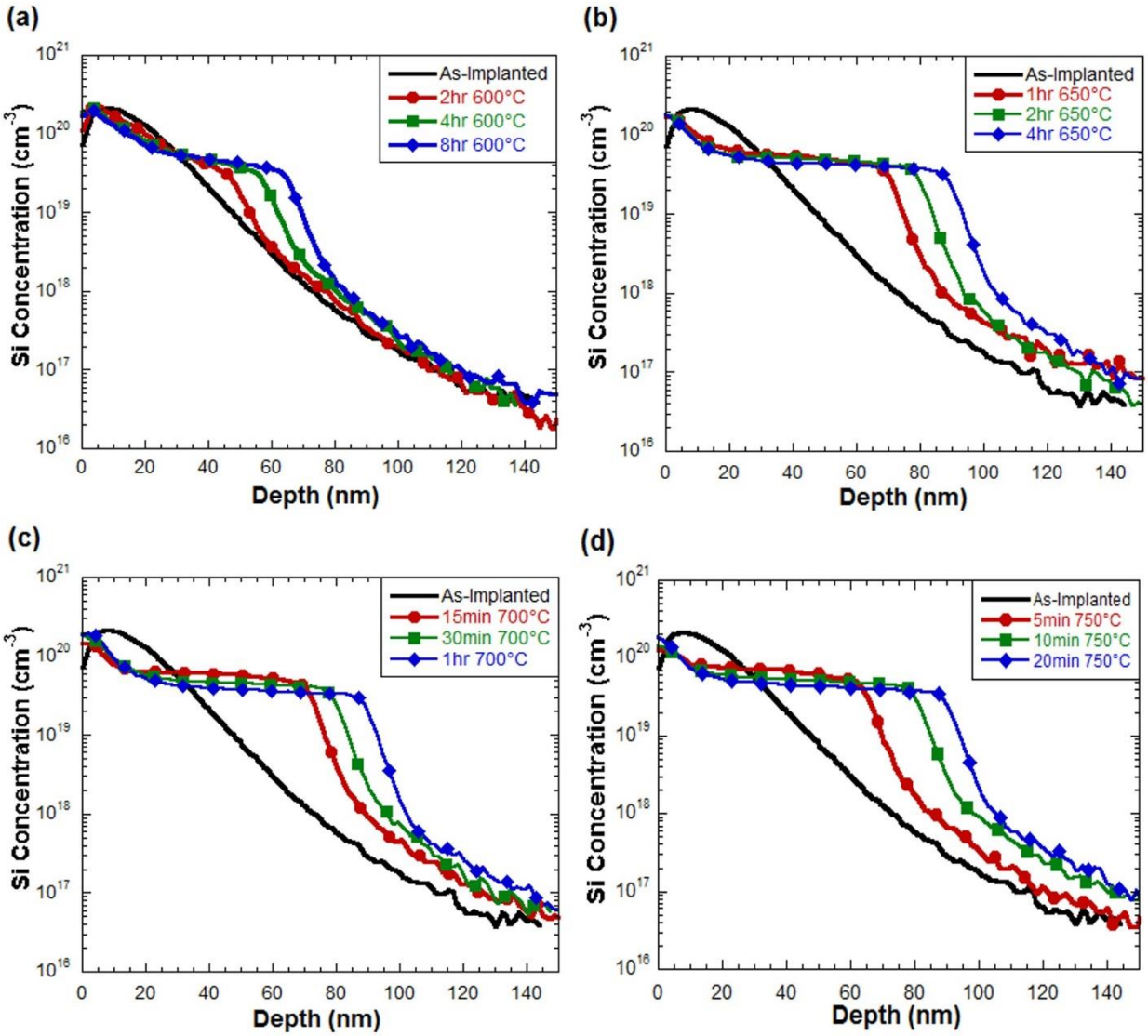

Figure 4-15. SIMS profiles of as-implanted and annealed 10 keV $5\times10^{14}cm^{-2}$ Si implants for (a) 600°C, (b) 650°C, (c)700°C, and (d) 750°C furnace anneals at varying times.[98]

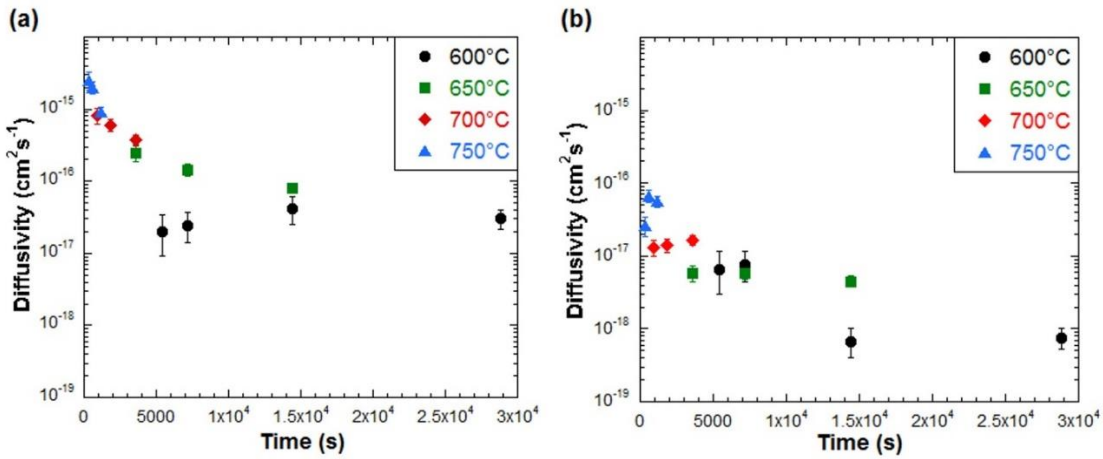

Figure 4-16. Extracted Fickian and Concentration-dependent diffusion coefficients for $5\times10^{14}cm^{-2}$10keV Implanted InGaAs at 80°C. [98]

4.2.3 Co-Implant Study Diffusion Results

The diffusion behavior mirrored results as discussed in Section 4.1, where no major deviations in behavior occurred. There were little differences in Si diffusion behavior with and without the co-implant species, including P and Al. A main difference was how far the concentration dependent shoulder evolved with time, with greater reduction with increasing co-implant dose, as summarized by Figure 4-17.

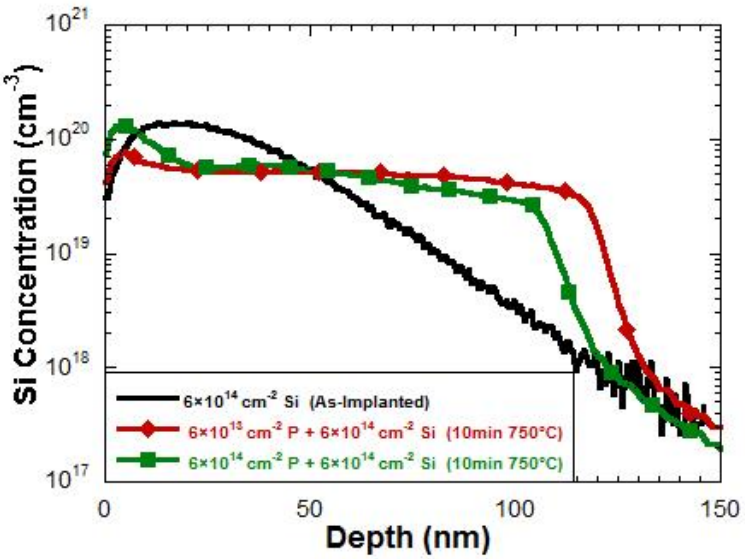

Figure 4-17. SIMS profiles of $6\times10^{14}cm^{-2}$ Si^{+} co implanted with P^{+} and annealed for 10m 750°C. Si diffusion retardation observed due to increasing P^{+} co-implant dose.

2.4.3.1 Sulphur Co-implants

It is also important to note that sulphur had significant diffusion in all annealed samples, so much that large portions were piling up at the InGaAs/InP interface, as shown in Figure 4-18. This rapid diffusion is characteristic of interstitial diffusion, where dopants diffuse rapidly through interstitial locations in the lattice, and eventually find a substitutional site, as shown in Equation 4-1[99].

$$S_i + As_{As} \leftrightarrow S_{As} + As_i \tag{4-1}$$

Where sulphur would diffuse interstitially until kicking out an arsenic atom. Fortunately, the extracted sulphur effective diffusivity from this work is roughly in agreement with that of literature, at about $4.0\times10^{-13}cm^2s^{-1}$, whereas literature values ranged from 3×10^{15} to $4\times10^{14}cm^2s^{-1}$ at the same temperature, as shown in Figure 4-19[100–103]. With increasing sulphur dose, there was retardation of the advancing silicon shoulder at a concentration of $2\times10^{19}cm^{-3}$, which can be attributed to the greater disorder caused by the greater co-implant dose, similar to other co-implanted species.

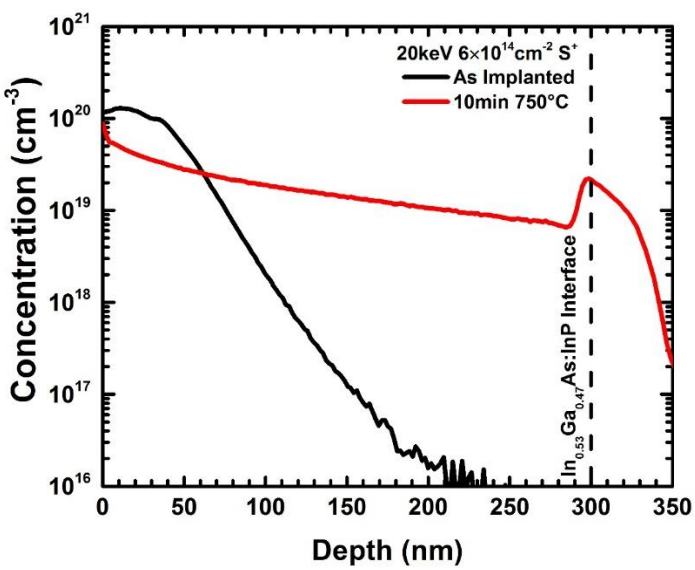

Figure 4-18. Significant sulphur diffusion of $6\times10^{14}cm^{-2}$ 20keV implant annealed at 10min 750°C in InGaAs, with pileup at InGaAs:InP Interface.

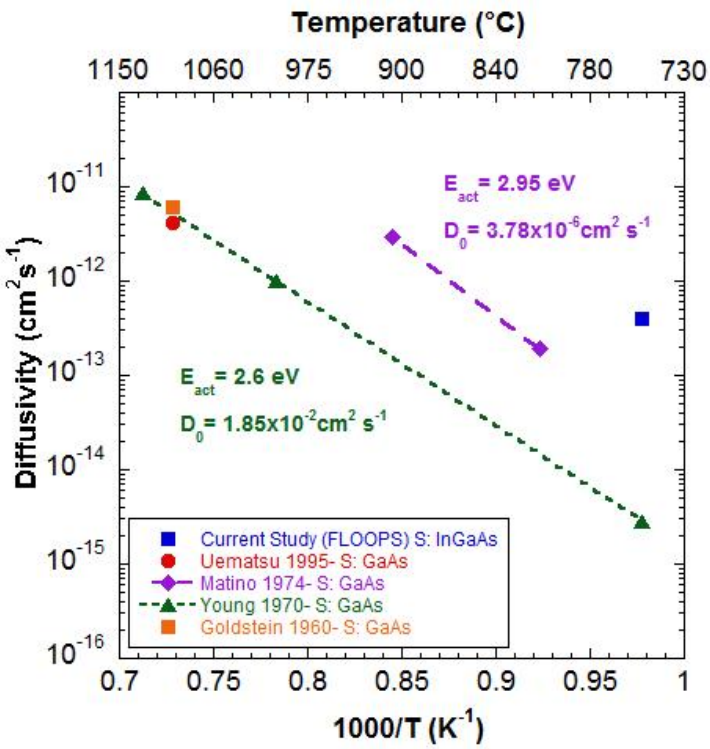

Figure 4-19. Comparison of extracted S diffusivity in InGaAs, compared to reported values of sulphur in GaAs[100–103].

2.4.3.2 Argon Co-implants.

The main purpose of using Ar as a co-dopant as part of this study was to observe the effect of pure implant damage upon silicon activation and diffusion, since it is a noble gas. Unexpectedly, Ar seemed to have more than just a damage effect. As seen in Figure 4-20, there was significant retardation of the diffused Si profiles as the Argon dose increased from $5\times10^{13}cm^{-2}$ up to $6\times10^{14}cm^{-2}$. The highest dose almost completely inhibited the characteristic evolution of the concentration dependent Si diffusion front. Likewise, the electrical solubility of silicon in also decreased with increasing argon dose. Having both of these behaviors strongly following a similar trend with respect to argon dose point to some difference that the presence of Ar introduces in the lattice.

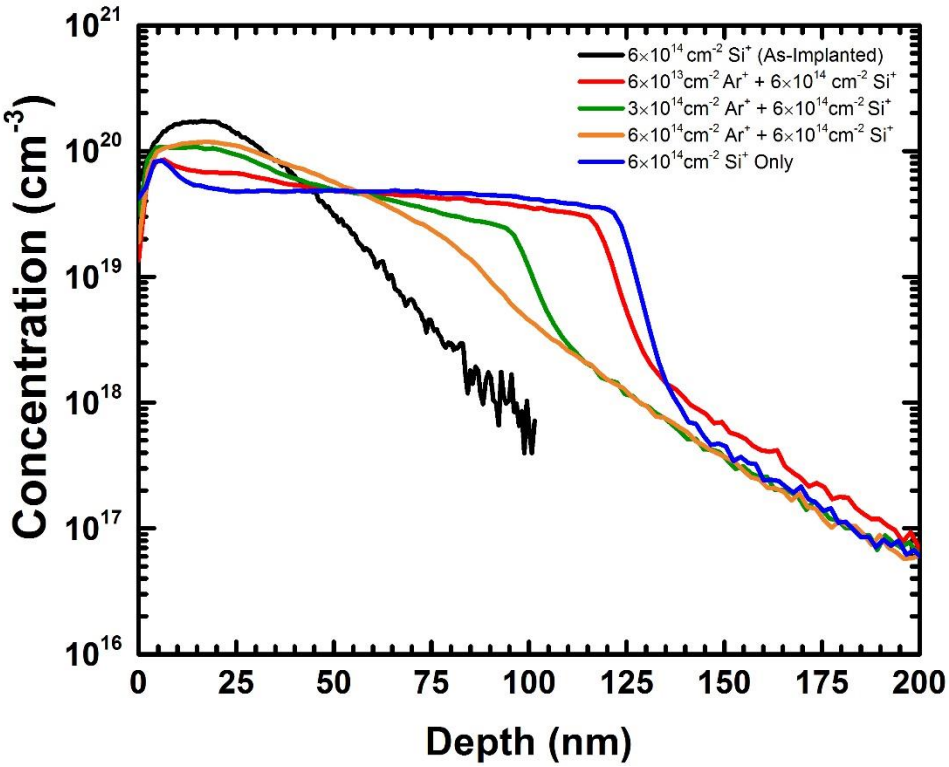

Figure 4-20. SIMS Profiles of Ar and Si in InGaAs implanted with 6×10^{14}cm^{-2} 20keV Ar^+ implant and 6×10^{14} 20keV Si^+ implant annealed at 10min 750˚C.

There has been instances where argon was reported to actually increase the electrical activation of dopants in GaAs like that of Liu et al[63]. They used a much higher 750keV Ar^+ implant into InGaAs, followed or preceded by a 200keV Si^+ implant. The activation ratio θ (N_A/N_D) decreased consistently with increasing Ar dose. This effect is likely due to the lower peak concentration of Ar achieved with the high energy implant, effectively preventing the formation of voids.

It is unlikely that the Argon is actually pairing with silicon or other dopants to prevent their activation; rather there is likely to be disruption of the lattice due to the generation of inert gas voids, and eventually formation of bubbles as the vacancies coalesce. Bubbles of ranging from 3 to 5nm in diameter have been observed in GaAs implanted with argon, indicating that it can form in other III-Vs as well[104]. A probable mechanism for this gettering-like behavior is the reliving of stress of interstitial argon

atom in the lattice, by interacting with a vacancy. More of this stress is relived with the addition of another neighboring vacancy, lowering the overall energy of the system. As more vacancies are aggregated, microvoids are known to form.

Several works have studied this effect on dopants in silicon. Milgram et al, had observed similar activation and diffusion inhibition for ion implanted B and Ar into silicon[105]. Other groups compared the different effects that noble gases have on silicon. There have even been groups that proposed that Ar was responsible tri atom complexes[106]. There is clearly redistribution and activation inhibition of dopants in the presence of argon, and is likely why argon implantation has been used for electrical isolation and gettering centers.

4.3 Silicon Marker Layers in InGaAs

4.3.1 Unimplanted Si Marker Layer Diffusion

There was clear and repeatable concentration-dependent diffusion behavior in ion-implanted silicon in InGaAs, and Si marker layers were grown in InGaAs via MBE to observe Si redistribution without Implant damage as illustrated in Section 4.1.5. Another potentially impactful variable is proximity of the doped layer to the surface, so a Si marker layer 275nm below the surface was grown to minimize any potential effects it would have on Si diffusion. Significant concentration dependence was observed for marker layers grown to a chemical Si concentration of $2\times10^{20}cm^{-3}$, as shown in Figure 4-21a. Lower concentration marker layers were grown to determine where this threshold or range where concentration dependent diffusion manifested. A peak concentration of $1\times10^{19}cm^{-3}$ annealed at 240m 700°C yielded significantly different results, with hardly any redistribution (Figure 4-21b). Using diffusivity extractions in FLOOPS, the effective

diffusivity of the high concentration regime was determined to be 11 times greater than the lower concentration $1\times10^{19}cm^{-3}$ peak concentration marker layers.

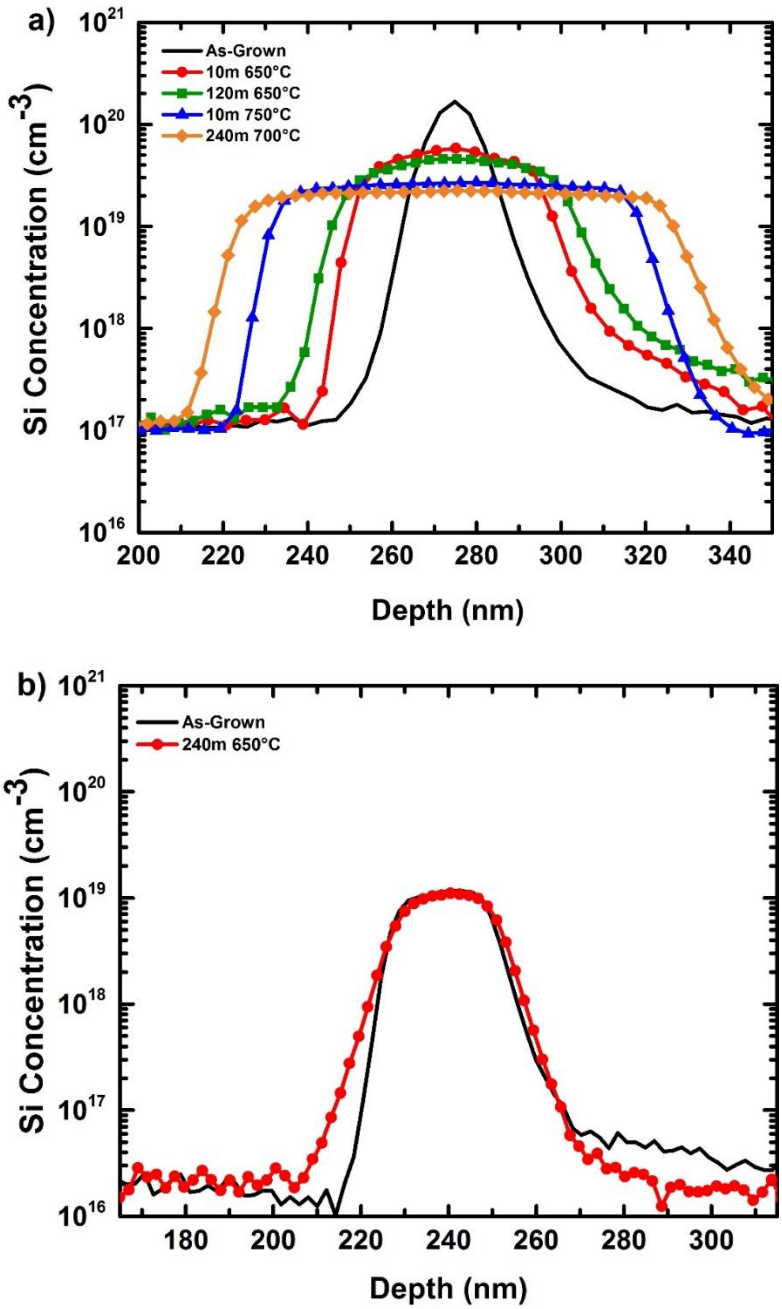

Figure 4-21. SIMS profiles of as-grown and annealed Si marker layer with $1\times10^{20}cm^{-3}$ peak concentration, ranging from 10min to 240min at 650°C to 750°C. b) SIMS profiles of as-grown and 240min 650°C annealed Si marker layer with $1\times10^{19}cm^{-3}$ peak concentration.[107]

4.3.2 Implanted Si Marker Layers in InGaAs

Another marker layer study was carried out to further understand and model the Si diffusion mechanism in InGaAs. Different types of isoelectronic Ga^+ implants were carried out to generate excess point defects in the vicinity of the Si marker layer. A Boltzmann Transport Code as described in Chapter 5 was used to predict defect concentrations around the layer and was used to select implant conditions as shown in Figures 4-22a and 4-23a. A set of samples received a shallow, 100keV 5×10^{13} cm^{-2} Ga^+ implant to introduce an excess of interstitials near the marker layer, to see if there was any notable enhancement or retardation of Si diffusion. Likewise, a high-energy 2MeV implant was carried out at the same dose to introduce excess vacancies around the marker layer to observe their effect on Si diffusion. As shown in Figure 4-22b, there is slight retardation of about 4-5nm of the SI marker layer in the 100keV Ga^+ implanted sample, suggesting that enhanced diffusion of silicon is retarded by excess interstitials. The observed retardation is well within the special resolution limits of SIMS, which is usually 1-2nm for the data from this work. This is further evidence that Si diffuses via a vacancy mechanism at higher concentrations in InGaAs.

The 2MeV implants yielded less-clear results, with vastly different diffusion behavior than expected, shown in Figures 4-23 b and c. There was significant scrambling of the layer due to penetration of gallium ions, where most come to rest deeper into the material (R_P=950nm). This led to a completely different profile evolution for the shorter, 10min 650°C anneal, reminiscent of the post-implantation tail broadening of silicon profiles observed initially, suggesting a different, possibly interstitial mechanism. Longer 240min anneals at 650°C indicate that the characteristic shouldering of the concentration dependent diffusion mechanism was recovering,

indicating that implant-generated disorder was being annealed out with time. It is important to note that although a net vacancy concentration was predicted around the layer post-implant, there was still a sizeable, nearly equal interstitial concentration, which could have also influenced the results.

One of the major takeaways from this work is that the dynamics and effects of isoelectronic implants into InGaAs seems to have a less pronounced effect on dopants in InGaAs, than that observed in Si substrates[91,108–110], likely due to differences in periodic lattices and possible dopant-defect interactions (second nearest neighbor vs first nearest neighbor pairings). Additionally, the low concentration broadening similarly seen in short RTAs of ion implanted samples further supports the existence of a rapid initial diffusion regime that occurs with implantation damage.

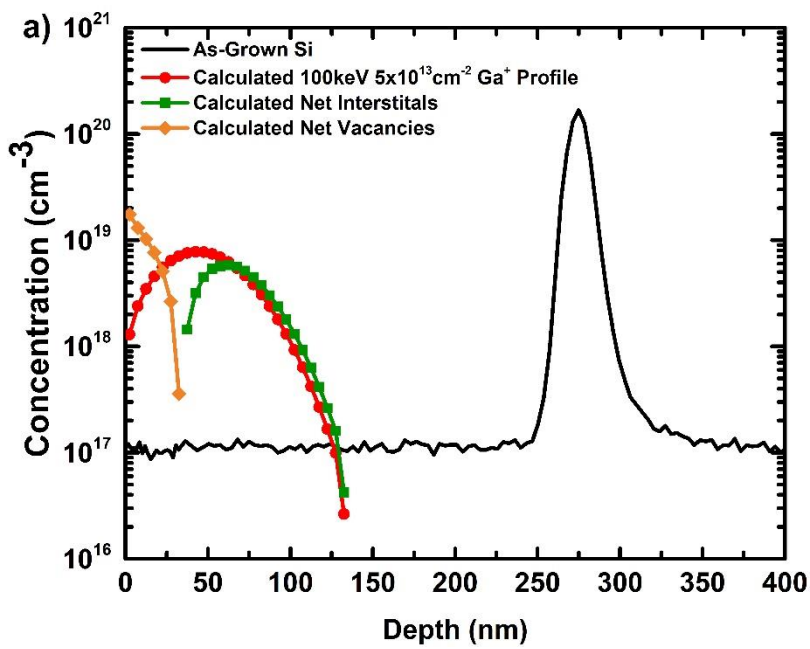

Figure 4-22. a) Predicted Boltzmann Transport Equation (BTE) profiles of as-implanted ions and net defects for 100keV $5\times10^{13}cm^{-2}$ Ga^{+} Implant overlaid with as-grown Si SIMS profile.

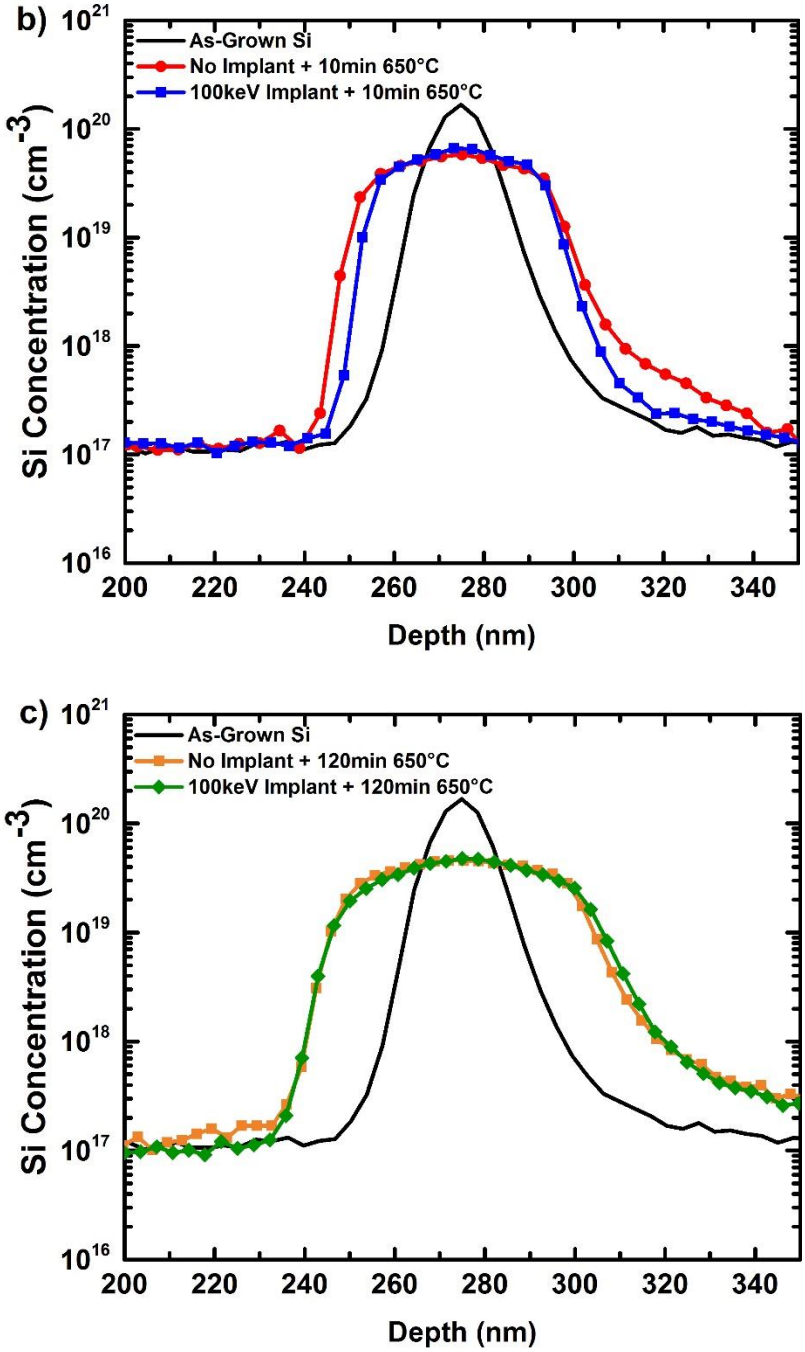

Figure 4-22 (continued). b) Effects of 100keV $5\times10^{13}cm^{-2}$ Ga^{+} Implant on Si profile evolution for 10min and c) 120min 650°C anneals.

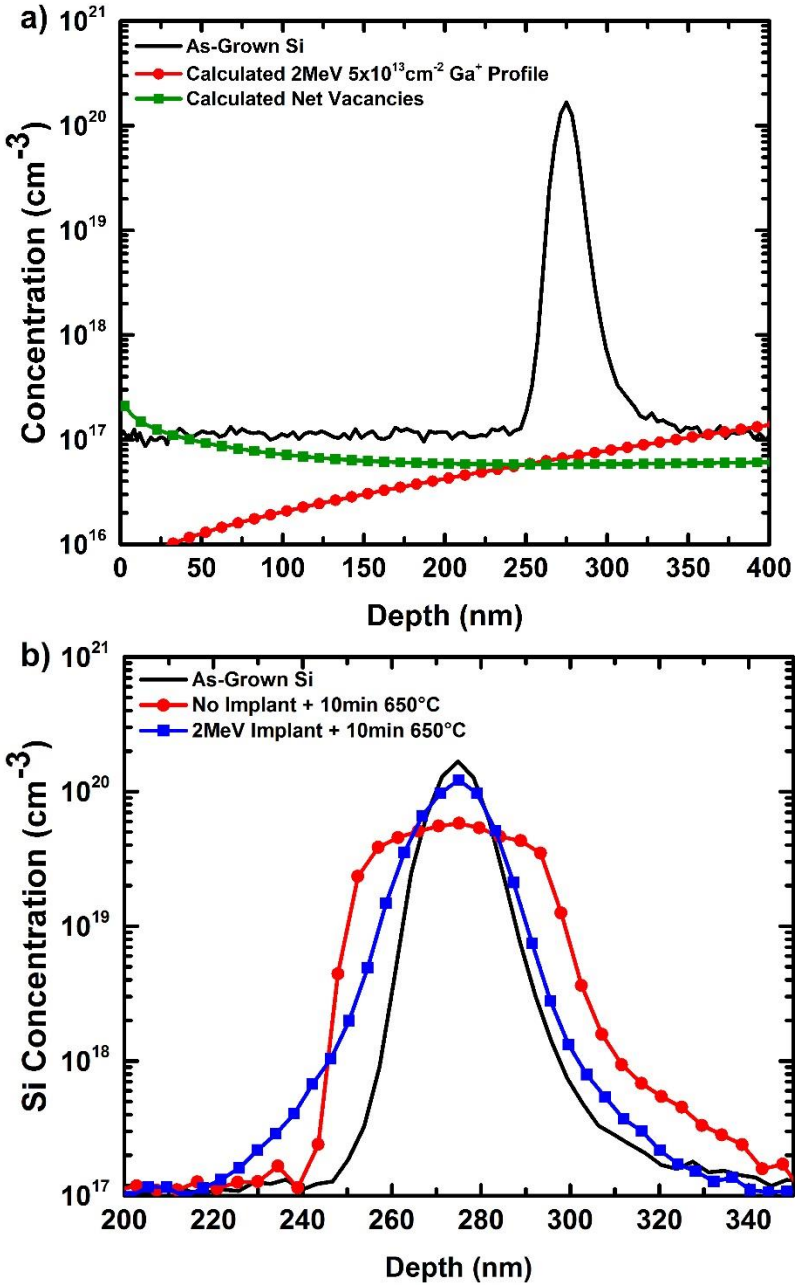

Figure 4-23. a) Predicted BTE profiles of as-implanted ions and net defects for 2MeV $5\times10^{13}cm^{-2}$ Ga^{+} implant overlaid with as-grown Si SIMS profile. b) Effects of 2MeV $5\times10^{13}cm^{-2}$ Ga^{+} Implant on Si profile evolution for 10min

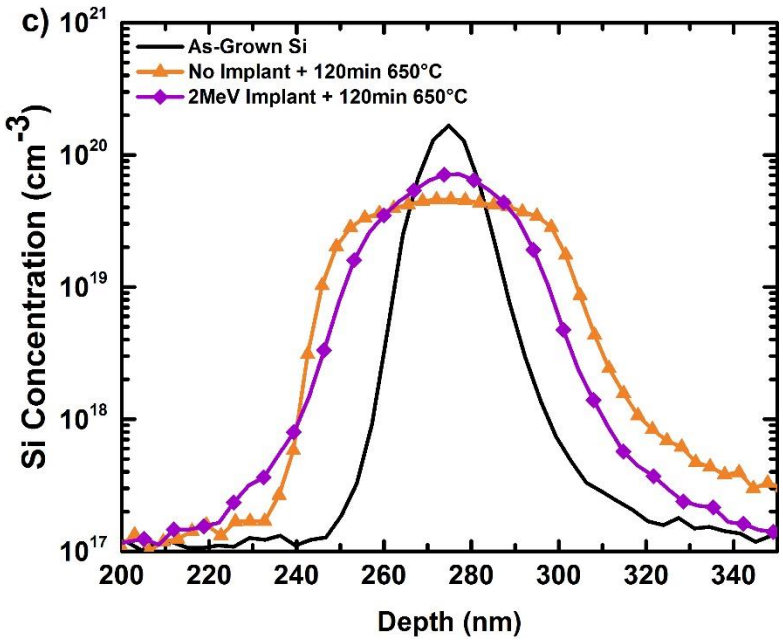

Figure 4-23 (continued). c) Effects of 2MeV 5×10^{13}cm^{-2} Ga^{+} Implant on Si profile evolution for 120min 650°C anneal.

4.3.3 Be Marker Layer Studies

Ion Implanted and MBE grown silicon at high concentrations exhibit box-like diffusion upon annealing, which has been shown to be vacancy-mediated. The formation of vacancies that enable this rapid diffusion need to be accounted for. As mentioned in Section 2.4.2, previous works have suggested that Frenkel pairs are produced in heavily n-type GaAs, where the generated interstitials enhanced neighboring Zn-doped regions[49,50].

The proposed primary mechanism for diffusion enhancement involved the generation of Frenkel pairs in the heavily Si doped region[49]:

$$Ga_{Ga} \rightarrow V_{Ga}^{-} + I_{Ga}^{+} \tag{4-2}$$

Where the interstitials would diffuse into the Zn-doped layer, enhancing Zn diffusion via a kick out mechanism:

$$Zn_{Ga}^{-} + I_{Ga}^{+} \rightarrow Zn_{i}^{2+} + 2e^{-} \tag{4-3}$$

This Frenkel pair generation was the mechanism claimed to be responsible for rapid broadening of adjacent zinc-doped, p-type regions, compared to p-type regions that were not adjacent to n-type regions.

An analogous study was carried out in InGaAs, using a Be Marker layer as an indicator of a flux of interstitials, since Be is considered and previously modelled as an interstitial diffuser[111–116]. A silicon doped surface layer was grown on one set of samples to see if Frenkel pairs were formed as silicon diffuses via concentration-dependent diffusion. Another set of samples were grown exactly the same as the first, but without Si doping at the InGaAs surface to serve as a control. The schematic of the Si-doped samples are illustrated in Figure 4-23.

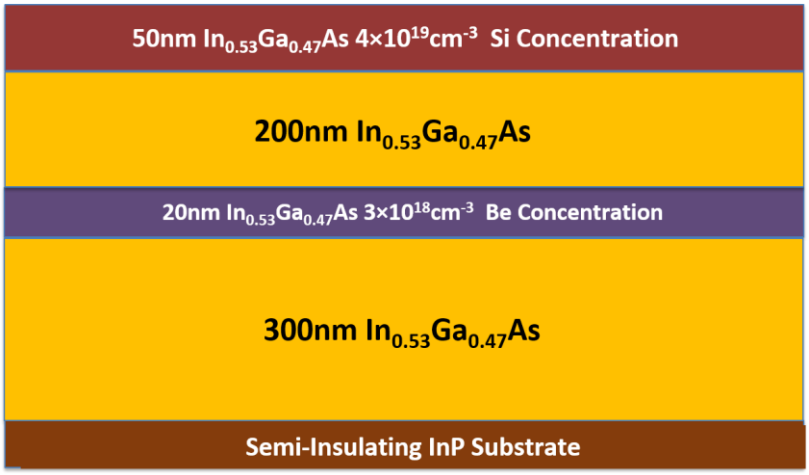

Figure 4-24. a) Schematic of MBE grown InGaAs structure with Si and Be marker layers.

Similar to Equation 4-3, the enhancement of the Be marker layer was expected to be observable with SIMS analysis due to the increase in the local interstitial concentration. There was no enhancement of the Be Marker Layer compared to non-Si doped control for all anneals, ranging from 10min at 600°C to 40min at 750°C. The Be marker layers of the two different sets were overlaid on each other to discern if there

was a notable difference in the two different conditions as shown in Figure 4-25. The most likely explanation for this lack of an enhancement effect in the Si-doped case is that interstitials are not very mobile in InGaAs, and haven't reached the Be marker layer with the given anneal times.

Using the distances as determined by SIMS in Figure 4-25, the interstitial diffusivity would need to be at least $3.75 \times 10^{-13} cm^2 s^{-1}$ in order to reach the Be layer, about 300nm away, in an identical 40min 750°C anneal. For comparison, previous Be simulation work have resulted in values for interstitial diffusivity in InGaAs ranging from 2.3×10^{-14}-$1.7 \times 10^{-11} cm^2 s^{-1}$ [114,116] at 750°C. Thorough experimental characterization of interstitial diffusion is needed in addition to simulation parameters, to be clear on how far interstitials can redistribute in InGaAs upon annealing. From this study, the possibility of Frenkel pairs being generated by the heavily Si-doped region cannot be ruled out, and is likely to be of more immediate significance for adjacent doped regions rather than features hundreds of nanometers away.

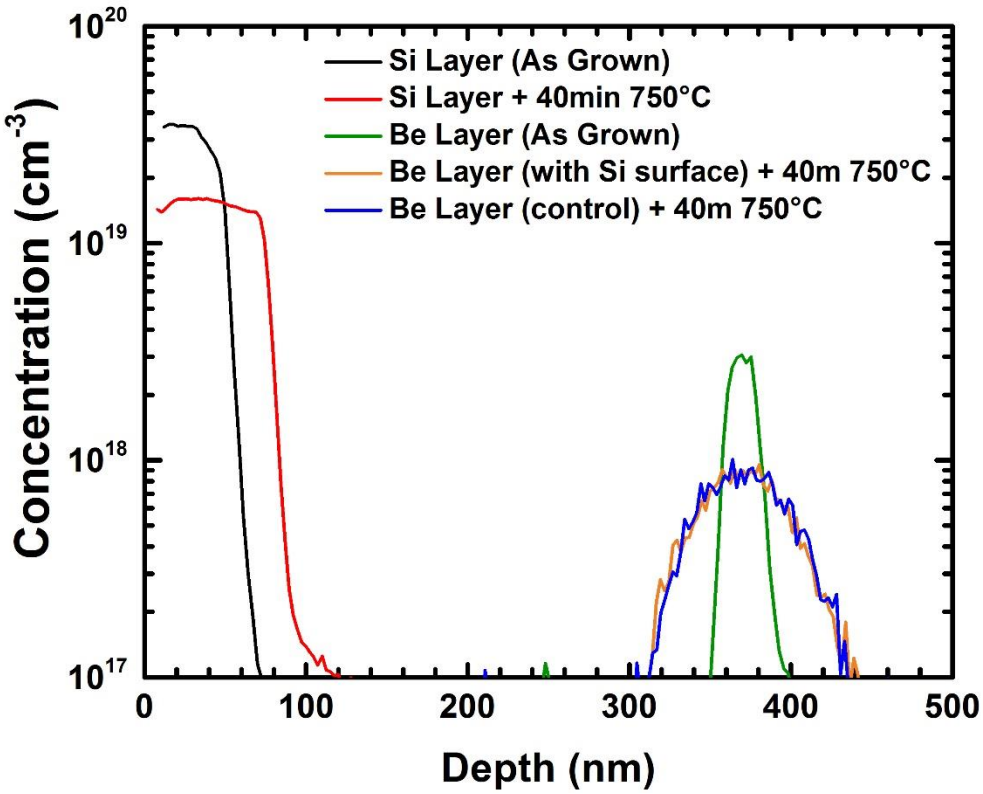

Figure 4-25. SIMS profile of Si Marker Layer before and after 40m 750°C anneal, and Be Marker Layer profiles with and without silicon surface doping for the same anneal.

4.4 Comparison Si Diffusion by Different Doping Methods

All ion implanted silicon into InGaAs obtained a notable as-implanted “tail” portion of profiles upon implant, which were then followed by an advancing concentration dependent diffusion shoulder at high concentrations with enough thermal processing. In contrast, the grown-in silicon by MBE did not exhibit this low concentration tail, but still had significant concentration dependent diffusion with enough thermal processing. Comparison of different doping methods were quantified through fitting the SIMS profiles using a finite difference solver approach that will be discussed in Chapter 5. According to the activation and diffusion results, it would be more advantageous to have

silicon grown-in, rather than implanted for initially steeper junctions, and less processing required for high activation.

4.5 Supplemental Point Defect Studies

Further experimental evidence points to the existence of significant concentrations of vacancies present in heavily Si doped regions of InGaAs by overserving the evolution of extrinsic interstitial loops[117]. Two sets of InGaAs samples received an non- amorphizing 20keV $6\times10c^{14}m^{-2}$ P^+ implant to generate damage, which formed a layer of extrinsic interstitial loops near the ion projected range. One set was nominally undoped InGaAs, while the other set has a 60nm $7\times10^{19}cm^{-3}$ Si-doped layer grown by MBE near the surface. Both were annealed at 650°C for 400 seconds, and a clear difference in the concentration and loop size of the Si-doped samples that these loops are being annihilated by vacancies as silicon diffuses deeper into the bulk as shown in Figure 4-26.

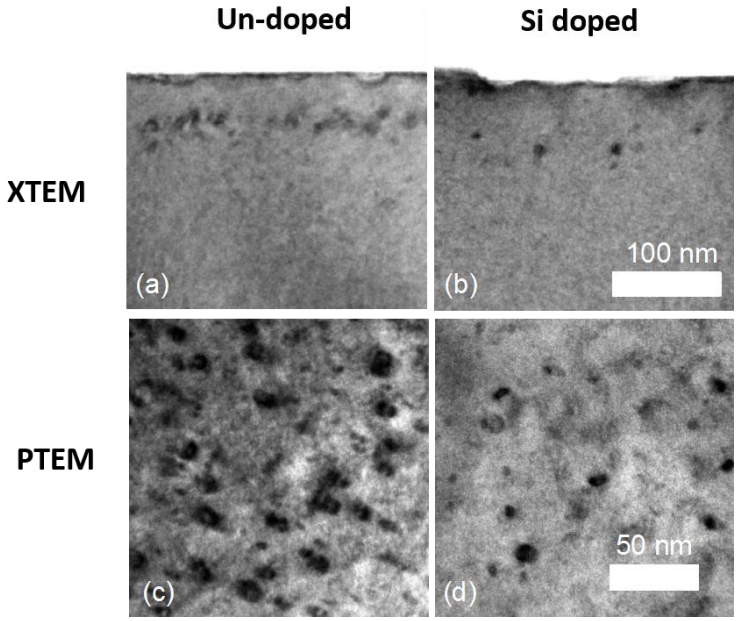

Figure 4-26. XTEM and PTEM images of InGaAs implanted with 20keV $6\times10^{14}cm^{-2}$ P^+ at 80°C with a) no Si surfaced doped region (XTEM), b) 60nm $7\times10^{19}cm^{-3}$ Si doped surface layer both annealed for 400sec at 600°C[117].

Another study was carried out with two separate types of implants that follows a similar trend between Si-doped and non-Si doped InGaAs samples. A 20keV $6\times10^{14}cm^{-2}$ P^+ implant while another set was implanted with Si in place of P with the same parameters. With greater annealing time, the loops in the Si-implanted InGaAs dissolved, while the loops in the phosphorus implanted samples coarsened with time, illustrated in Figure 4-27. Clearly having such a stark difference in the evolution of the loop layers by these different sample sets exposed to the same thermal processing suggests that vacancies are present in large quantities accompanying heavily doped Si regions in InGaAs.

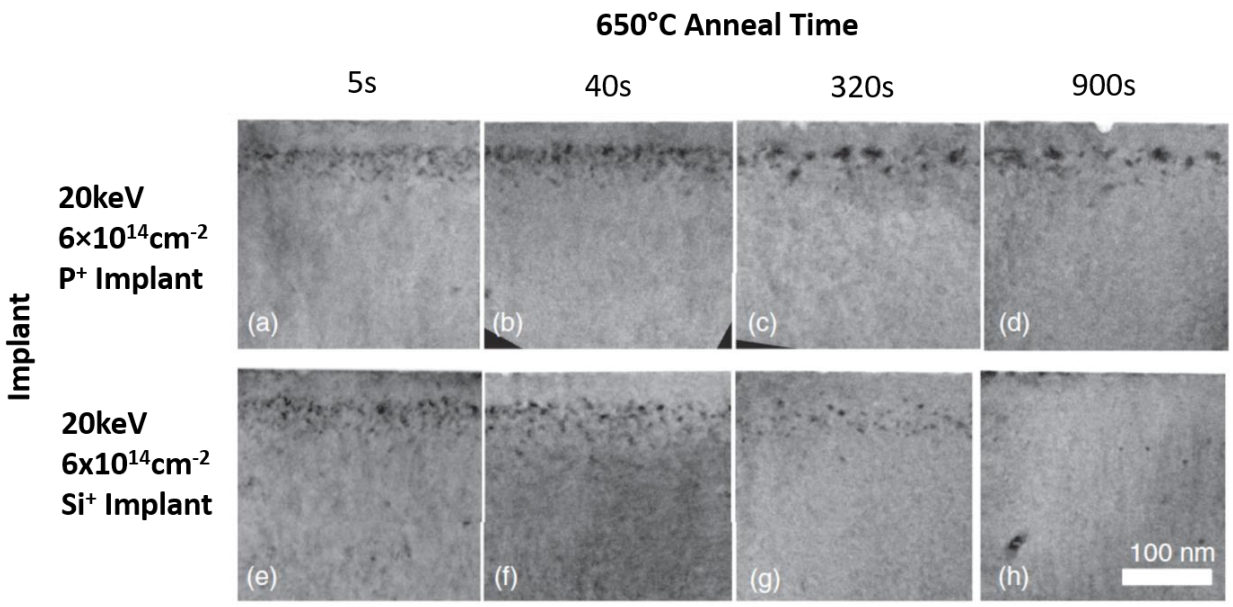

Figure 4-27. XTEM and PTEM images of InGaAs implanted with 6×10^{14} cm^{-2} 20keV Si^+ dose between 20-300°C, then annealed at 750°C for 5s[117].

4.6 Experiment Summary and Conclusions

A few points are quite clear from all of these experimental results. Si diffusion cannot be considered negligible in InGaAs, even for short-term rapid thermal anneals. There are clear tradeoffs for implanting with silicon and annealing in InGaAs, including

where significant channeling and subsequent broadening of the tail portions are observed. This channeling and rapid tail broadening of the profile is not observed for Si grown in by MBE which could make it preferable over implantation for ultra shallow junctions. In line with more recent diffusion models and ab-initio calculations, the project experimental results serve as further evidence that the concentration-dependent diffusion of silicon in InGaAs is mediated by vacancies, likely formed by increases in the local fermi level due to doping.

Finally, there is a close connection between the concentration threshold of this diffusion enhancement (1-3×$10^{19}$$cm^{-3}$) and the stable net activation of Si in InGaAs (1.7×$10^{19}$$cm^{-3}$) . For both and ion implanted MBE doped samples, there is an initial rapid activation or deactivation with negligible diffusion, then followed by significant concentration-dependent diffusion, as illustrated in Figure 4-8. The initial regime is likely where additional acceptor type defects (vacancies) are formed or Si is being compensated by them. Their existence then enables silicon to redistribute up to tens of nanometers deeper into the bulk, as the net activation approaches the stable value. It is likely that the diffusion of Si would be halted when the chemical concentration dips below the threshold of enhancement (1×$10^{19}$$cm^{-3}$), leading to a decrease in the concentration of cation acceptor vacancies that enables diffusion.

CHAPTER 5
FLOOPS and TCAD TECHNIQUES

5.1 TCAD/FLOOXS Introduction

In many fields and industries, it is advantageous to have a simulator or program to model and predict behavior of the system or materials of interest. Doing so saves significant amounts of time, cost, material and other finite resources for system or material development[118]. For example, groups studying metals or superalloys have programs like Thermocalc, NASA's COSIM, and others to predict what phases are most likely present, or predict the lifetimes of certain machine components[119]. For semiconductor device processing and operation, there are variety of programs developed, but the ones used for this work involved modelling and predicting ion implantation, dopant diffusion and activation in our material of interest, InGaAs.

5.2 SRIM

Ion Implantation, as described previously, is a semiconductor processing step that introduces impurities into a substrate or target material. Predicting the implant damage, ion distribution and other factors from an implant are invaluable capabilities provided by implant simulator programs. The Stopping and Range of Ions in Matter (SRIM) is such a program developed by James Ziegler that is used to predict the implanted ion depth and damage introduced for different substrates. It is a Monte Carlo-based program, which utilizes random numbers to help calculate an unknown value or set of values [120]. This type of approach was aptly named after the European city that is famous for its gambling facilities. A random number seed is used to obtain different calculations for every simulated ion implanted. If this was not included, the exact same output would occur for every incident ion[121]. A few of the simulated outputs include:

implanted ion range, straggle, kurtosis, phonons, and atoms transmitted or sputtered. Utilizing its graphical user interface, a user can specify the incident ion, energy, angle of implantation and the chemical composition, layers, and densities of a target material. Example outputs of the ion profile and vacancy profiles are included in Figure 5-1. It is important to note that the outputs are normalized per ion, so in order to get an actual concentrations (defects or ions per cm^3) the output must be multiplied by the actual implant dose. Since predicted accuracy is important, the simulation should run at least 100,000 ions to get sound statistical outputs from the simulation.

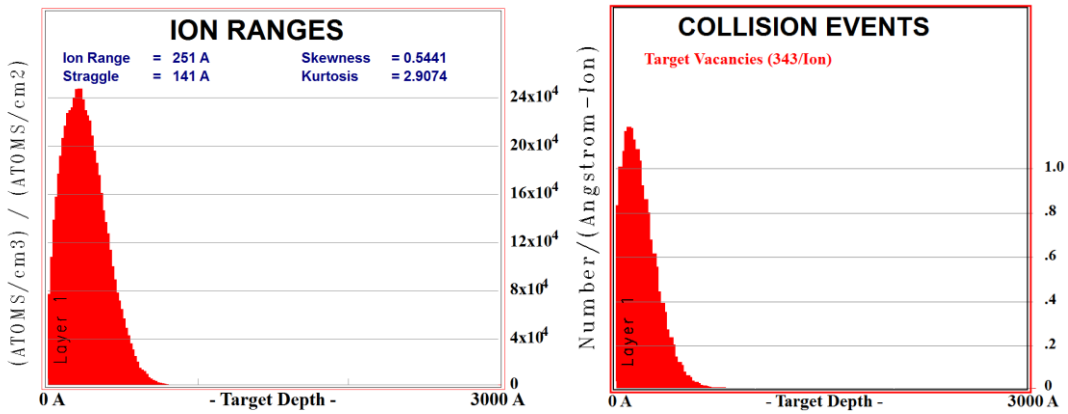

Figure 5-1. Examples of normalized a) ion range, and b) vacancy SRIM outputs for a 20keV Si^+ implant into $In_{0.53}Ga_{0.47}As$.

Two other notable parameters that SRIM uses for simulation is displacement energy and surface binding energy. As discussed previously displacement energy is the amount of energy required to move an atom one atomic spacing. If an atom does not have energy equal to the displacement energy, it will return to its original position in the lattice and release its recoil energy as phonons into the bulk. Sputtering is governed by the surface binding energy, which accounts for surface roughness, damage, and relaxation that can occur during implantation. Determining the number of defects generated by ion implantation are interconnected, and different defects formed

(interstitials and vacancies) can be determined based on collision and cascade events during implantation[121].

$$Displacements = Vacancies + Replacement\ Collisions \tag{5-1}$$

$$Vacancies = Interstitials + Transmitted\ and\ Sputtered\ Ions \tag{5-2}$$

Equation 1 ensures that all atomic displacements, interstitials, vacancies, and atoms lost from the substrate balance out. The first and most simple calculation mode for SRIM is Ion Distribution and Quick Calculation of Damage, which obtains the resulting ion profile using Kinchin-Pease model[122,123]. The model estimates the number of displaced atoms (N_d) by primary knock on atoms of energy E as summarized in Equation 5-3 below:

$$N_d = \begin{cases} 0 & \\ 1 & 0 < E < E_d \\ \frac{E}{2} E_d & E_d < E < 2E_d \\ \frac{E_1}{2} E_d & 2E_d < E < E_1 \\ & E_1 < E < E_\infty \end{cases} \tag{5-3}$$

Where no displacements occur when the given knock-on energy is less than the displacement energy (E_d). When E is greater than E_d, but less than energy E_1, the primary method of stopping occurs by nuclear scattering, and the amount of displacements correspond more closely with the number of ions implanted. Above the threshold value E_1, electronic stopping is the primary stopping method.

Another more computationally expensive model is titled “Detailed Calculations with Full Damage cascades”, which follows the trajectory of each ion and atom in the resulting recoil cascade. Output files, such as “Collision.txt” store this data for every ion, and can quickly become several gigabytes in size.

One of the major caveats of SRIM is that fact that it does not assume a crystalline target material; therefore effects such as ion channeling are not predicted. Another aspect to consider when using SRIM is that the implantation events are assumed to be at 0K. Dynamic annealing and annihilation of excess defects due to temperature of implantation is not taken into account, but can be a substantial factor in resulting implant damage. It is stated as a rule of thumb by Ziegler that ~99% of implant damage is removed during room-temperature implantation[121]. All profiles used from this program were adjusted accordingly for this entire project. Despite these caveats SRIM is a useful program to determine ion ranges and damage events in an implanted material or layers of a material.

5.3 Boltzmann Transport Equation Program

Despite the usefulness of SRIM and its relative ease of use, additional details from implantation were needed to design experiments and better understand the damage evolution in the substrate. A Boltzmann- Transport Equation Ion implantation program written by Martin Giles was used to obtain additional damage details for this work. Unlike SRIM, this FORTRAN code directly predicted damage profiles for both vacancies and interstitials, and included the option of simulating channeling tails of ions. An example output of the program is included in Figure 5-2, where vacancy-rich surface regions and interstitial-rich regions deeper in the bulk and can be predicted.

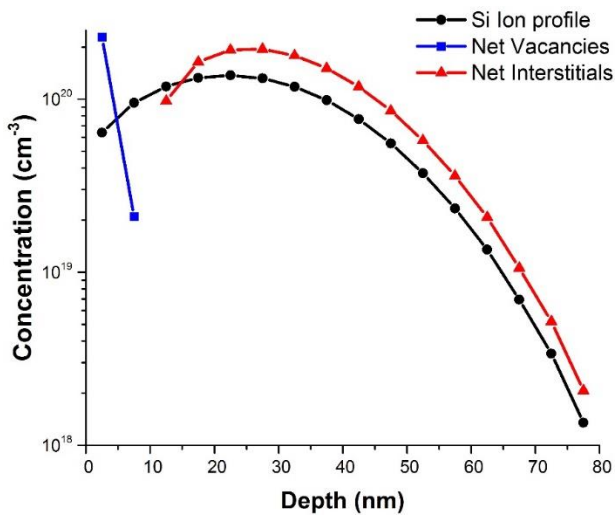

Figure 5-2. 20keV 6×10^{14}cm^{-2} Si Implant ion and net defect profiles predicted by Giles BTE code.

The primary Boltzmann transport equation is integrated to obtain the resulting profile of particles with respect to substrate type and primary ion energy[124]:

$$\frac{\partial F(p)}{\partial z} = N \int \left(\frac{F(p')d\sigma(p'\rightarrow p)}{\cos\theta_{p'}} - \frac{F(p\ \ )d\sigma(p\rightarrow p)}{\cos\theta_{p}} \right) + Q(\mathbf{p}) \tag{5-4}$$

Where p and p' are the initial and post scattering momentum values and N is the lattice density of the target material. When a particle is below a set momentum value, it would be considered stopped, leading to the resulting ion and damage profiles. Q is the generation term that allow particles to be created from rest. Cosine terms are used in the denominator to account for the distance an atom travels in the z direction (direction of implant) at an angle θ.

With lower implantation energies more commonly used, the effects of ion backscattering from the surface become more significant[123]. A multipass approach is used in the BTE code to track and account for the backscattered ions in the target, updating the energy-angle matrix on every pass. All atoms that scatter at an angle θ equal to greater than 90 degrees are considered backscattered, and their energy and

direction are stored and accounted for the next pass, where it will transfer energy to other atoms. This cycle would continue until all motion has stopped. Nuclear cross sections were calculated following the approach presented by Wilson et al. [125] and electronic stopping values were used from LSS theory[126]. All ion-implanted simulations in this project started with either initial defect profiles generated from SRIM or the aforementioned BTE code.

5.4 FLOOPS

The Florida Object Oriented Process and Device Simulator (FLOOXS), is a tool to simulate Semiconductor processing and device operation steps. The wildcard “x” is a placeholder for the interchangeable Process or Device functions of the program. A precursor to this tool was the Stanford University Process Modelling Program (SUPREM). FLOOXS has had several releases and commercial versions since its first completed version in 1993, including Synopsis Sentaurus Process and Interconnect. Each FLOOXS variant and release added new capabilities and changes. FLOOPS has capability to simulate implants, oxidation, thermal processing, deposition, etching and other processing steps.

5.4.1 Finite Difference

In order to solve for potential or continuity equations of dopants electrons, holes or other components of interest, partial differential equations (PDEs) for the species and are solved using difference techniques at each node for the various time steps. The two main approaches are finite difference and finite element discretization. Previous versions of FLOOXS utilized the finite difference approach to solving a series of differential equations for simulations. In this project, finite difference approach was used. A representative approach for finite difference is illustrated in Equation 5-5[127]:

$$\left.\frac{d\psi}{dx}\right|_{x=x_i} = \frac{\psi(x_{i+1}) - \psi(x_{i-1})}{\Delta x_{i+1} + \Delta x_i} - \frac{\Delta x_{i+1} - \Delta x_i}{2} \left.\frac{d^2\psi}{dx^2}\right|_{x=x_i} + \frac{(\Delta x_{i+1})^2 - \Delta x_{i+1}\Delta x_i + (\Delta x_i)^2}{6} \left.\frac{d^3\psi}{dx^3}\right|_{x=\zeta} \tag{5-5}$$

Where the differential operators are converted to an algebraic expression at every node using a Taylor series expansion. We can further simplify Equation 5-5 by neglecting the second and third terms on the right hand side of equation.

$$\left.\frac{d\psi}{dx}\right|_{x=x_i} = \frac{\psi(x_{i+1}) - \psi(x_{i-1})}{\Delta x_{i+1} + \Delta x_i} \tag{5-6}$$

The sum of those neglected values is the local truncation error (LTE), which is the difference between the calculated value and the actual value of a parameter at a given point. Spacing between points directly affects the local truncation error. The greater the number of points, and smaller the spacing, the smaller the LTE for a given simulation**.** Usually, LTE is roughly the value of the grid spacing squared. When the spacing is decreased by half, the LTE decreases by a factor of four.

More recent versions of flooxs (including the 2014 version) utilize a finite element approach to solving differential equations, particularly for the 2D and 3D simulations. The main difference between finite element and finite difference is in the way that algebraic equations are derived from the differential terms and in one dimension result in the same final expressions.

5.4.2 Grid Spacing

Having additional grid points can lead to more accurate results, as indicated through the decrease in local truncation error (LTE) as discussed in the discretization techniques. This additional accuracy comes at a price, as it is important to balance simulation accuracy with computation time. One way to do this is the adjust the node

spacing for different simulated regions, for example having 1nm spacing near the surface, and 5nm spacing deeper into the bulk for a shallow implant processing step. An illustration of grid variation is included in Figure 5-3 where finer node spacing is set closer to the silicon wafer surface during an oxide deposition step. Finer spacing results in more algebraic calculations, leading to more computation time and resources. Also, it is important to have a smooth transition of grid spacing in order to have successful convergence of solved variables during simulation.

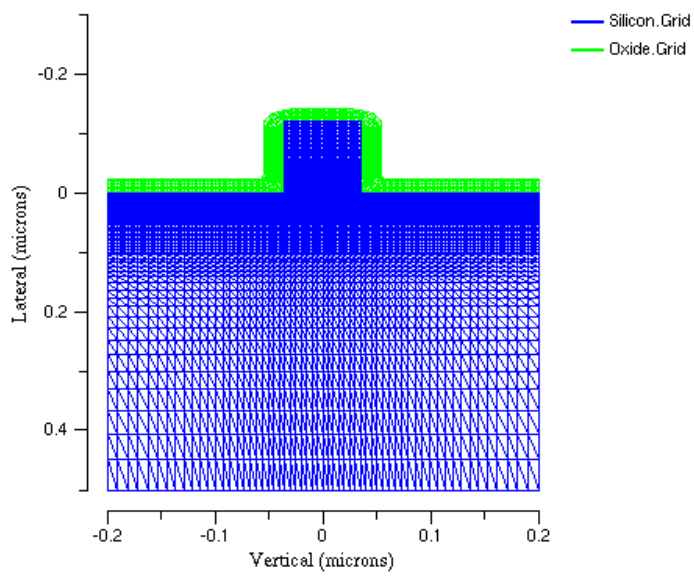

Figure 5-3. Example FLOOPS simulation illustrating gradual changes in node spacing for an oxide deposition simulation step, with larger grid spacing deeper into the bulk[128].

5.4.3 Defect Continuity Equations

Simulation of point defects are critical for process modelling, so the bulk and surface kinetics of point defects can also be can be accounted for in FLOOPS. The interstitial and vacancy continuity equations excluding surface effects are illustrated in equations 5-7 and 5-8:

$$\frac{d(I)}{dt} = \nabla \cdot (D_I * \nabla(C_I)) - Kr * (C_I * C_V - C_I^* * C_V^*) \tag{5-7}$$

$$\frac{d(V)}{dt} = \nabla \cdot (D_V * \nabla(C_V)) - Kr * (C_I * C_V - C_I^* * C_V^*) \quad (5\text{-}8)$$

Equilibrium concentration of defects and local concentration of defects are $C_{I,V}^*$ and $C_{I,V}$ respectively. Surface ($g_{I,V}$) generation terms can also include in the continuity equation, which can be adjusted to account for generation or annihilation of defects at material interfaces. The bulk interstitial-vacancy recombination rate (K_r) is calculated as:

$$Kr = 4 * \pi * R_c * (D_I + D_V) \exp\left(-\frac{E_a}{k_B T}\right) \quad (5\text{-}9)$$

Where R_c is the Interstitial-Vacancy capture radius, D are the diffusivity of interstitials and vacancies and E_a is the barrier to I-V recombination. For second nearest-neighbor pairs, R_C is $\frac{\sqrt{3}}{4}$ times the lattice constant[26]. If E_a is set to zero, then the recombination of interstitials and vacancies are limited by the rate at which defects can reach the capture radius, which is governed by defect diffusivities. In contrast, if the recombination barrier is non-negligible, then the I-V rate would be reaction-limited. Due to the consistent nature of silicon diffusion regardless of proximity to the surface, this surface generation term was included but was of less importance in the presented diffusion model.

$$g_{X,S1} = -K_{surfX} * (C_{X,Side\,1} - C_X^*) \quad (5\text{-}10)$$

It is clear from these relations that the generation of point defects at the surface and in the bulk is largely governed by the local deviation from equilibrium conditions. The further the concentration from equilibrium, the larger generation or annihilation of that respective point defect in the bulk or at the material surface.

5.4.4 Fermi Level Dependent Equilibrium Defect Concentration

Local concentration of charged point defects are governed by the local fermi level, and should be accounted for, especially in heavily doped regions. Additional

parameters were added in floops to account for this local dependence, through varying equilibrium concentrations. A method of determining equilibrium concentration of neutral defects with respect to fermi level was derived from Tan et al. and used in the diffusion model [29]:

$$C_{V0Ga}^{eq} = 0.293\ P^{\frac{1}{4}} T^{-\frac{5}{8}} \exp\left[-\frac{h_{V0Ga}^{f} + \delta_{hAs}}{k_B T}\right] \tag{5-11}$$

Where h (standard enthalpy of formation) and δ_{hAs} (difference of binding enthalpy of As atom in InGaAs and As_4) are 2.606 eV and -0.3659eV respectively. These specific values were obtained from tabulated data[129] and used in a method described by Van Vetchen [130]. The arsenic pressure (P_{As4})is a vital parameter that determines relative abundance of defects in III-Arsenides, and is often included in several models dealing with abundance of defects on certain sublattices [29,131–133]. In order to find equilibrium concentration of charged defects, the neutral defect equilibrium values were multiplied by specific ratios based on the ionization energies:

$$\frac{C_{V_{Ga}^{3-}}^{eq}}{C_{V_{Ga}^{0}}^{eq}} = \exp[-(E_{a3} + E_{a2} + E_{a1} - 3E_F)\,/k_B T] \tag{5-12}$$

Where the acceptor level energies were determined from Komsa et al[131]. E_{a1}, E_{a2}, and E_{a3} were calculated to be 0.09488, 0.4666, and 0.7594 eV respectively, assuming roughly equal fraction of indium and gallium content. The starting profiles of interstitials and vacancies for all MBE-grown samples were calculated using this method, and saved as an input file to start diffusion simulations in FLOOPS. Since the actual samples were grown at 490°C, the starting defect profiles were calculated using the starting silicon concentrations, and resulting local fermi levels over those regions.

5.1 Dopant Diffusion models

5.4.5 Constant Diffusion Model

In the simplest of cases, impurities in a material can be modeled using a constant diffusivity, which leads to a simple broadening Gaussian profile.

$$\frac{\partial C_A}{\partial t} = \nabla \cdot (D_{A0} * \nabla(C_A^+)) \tag{5-13}$$

Where C_A^+ is the total impurity concentration, C_A^+ is the active and mobile concentration of an impurity and D_{A0} is its respective diffusivity in a medium. A recurring assumption for semiconductor process modelling is that the only impurities that are mobile are electrically active[134]. Both the activation behavior and mobility are considered one in the same, which is commonly governed in the model by a smoothed solubility limit, as illustrated in Equation 5-14.

$$C_A^+ = \frac{\mathrm{C_{A,Sol}(T)*C_A}}{\mathrm{C_{A,Sol}(T)+C_A}} \tag{5-14}$$

Where the smoothing function involves the temperature-dependent solubility limit $\mathrm{C_{A,Sol}(T)}$. As will be discussed later, changes were needed to account inactive yet mobile species. This was carried out using a different variable, called mobile dopant concentration $C_{A,mob}$ in place of electrical solubility, which accounted for the mobile, yet inactive concentrations observed through experiment.

5.4.6 Initial Scaling Factor Diffusion Model

Upon first noticing concentration dependent diffusion, a series of anneals were carried out in a tube furnace in argon ambient to further characterize this diffusion, with anneals ranging between 550°C to 750°C for 5 seconds to several hours. An initial model was developed and used to extract migration energies of the Fickian (D_f) and concentration-dependent (D_c) components that were quantified[98]. The initial model included and described in this work did not account for point defects, or their

interactions with silicon atoms. Equation 5-15 illustrates how the effective Si diffusivity term (D_{eff}) was calculated. Equation 5-16 was the dopant flux incorporated for Si redistribution through the simulated InGaAs matrix.

$$D_{eff} = \mathrm{D_f} + \mathrm{D_c}\left(\frac{\mathrm{C}}{10^{19}}\right)^{\mathrm{n}} \tag{5-15}$$

$$\frac{\partial C_A}{\partial t} = D_{eff} \times \nabla\left(C_{Si,mob}^{+}\right) \tag{5-16}$$

A sensitivity fitting parameter of 10^{19} was used to account for the high concentrations of silicon, since it was the same magnitude at which the Si plateaus consistently developed. Very high (n≥4) powers of concentration dependence were used to obtain appropriate fits with the diffusion data. Since significant amounts of silicon was mobile yet inactive due to convergence to 1.7×10^{19} cm^{-3} active concentration, a mobile concentration term ($C_{Si,mob}$) was used, in deviation with conventional assumptions that only active species are mobile, as used in silicon based systems[135]. A smoothing function analogous to Equation 5-14 was also implemented, since abrupt profile changes would inhibit convergence of the finite difference solving approach used in FLOOPS. C_{Si} is the chemical (total) concentration of silicon at a given location in the medium. Arrhenius relationships of mobile concentrations for all major sample sets are included in appendix B. Examples of fits using the initial model is included in Figure 5-4, as well as extracted Fickian and concentration dependent terms in Figure 5-5.

$$C_{Si,mob} = \frac{\mathrm{C_{Si,mob}(T)} * \mathrm{C_{Si}}}{\mathrm{C_{Si,mob}(T)} + \mathrm{C_{Si}}} \tag{5-17}$$

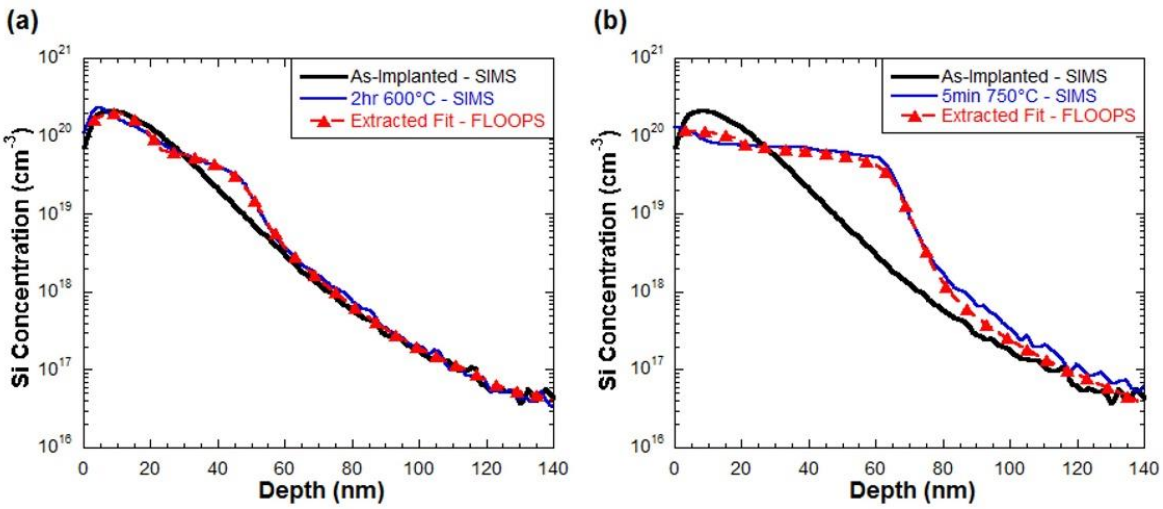

Figure 5-4. a-b: Example profile fits using preliminary scaling model[98]

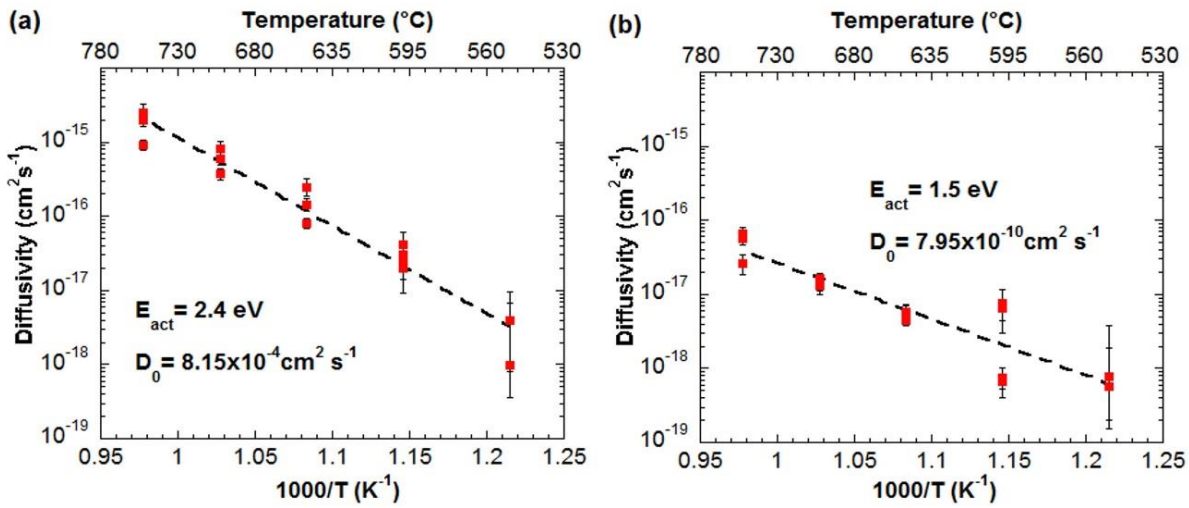

Figure 5-5. a-b: Extracted Fickian and Concentration dependent diffusivity components and migration energies using preliminary sensitivity factor diffusion model[98].

5.4.7 Fermi Model

The scaling factor diffusion model was an adequate start, but does not account for charge and electric field effects of doping. The Fermi diffusion model developed in FLOOPS accounts for local fermi level variations in the bulk due to doping through the use of Poisson's equation. One limitation of this model is that it does not account for individual point defects in dopant diffusion; it is primarily accounting for a Fermi level

effect using concentration-dependent terms(D_{Az}) in addition to a Fickian diffusion term (D_{A0}). These components are included in the impurity flux equation:

$$\frac{\partial C_A}{\partial t} = \frac{\left(D_{A0} + \sum_z D_{Az}\left(\frac{n}{n_i}\right)^z\right)}{\left(\frac{n}{n_i}\right)} \times \nabla\left(C_A^+ \times \left(\frac{n}{n_i}\right)\right) \tag{5-18}$$

Where C_A^+ term is determined by solid solubility or mobile concentration limit as described previously.

5.4.8 Charge Neutrality and Poisson's Equation

One of the fundamental parameters to solve for in a semiconductor process or device simulation is the free carrier concentration throughout the simulated material. Despite changes in temperature, doping concentration, and doping type, charge neutrality should always be preserved[136]. The fundamental relationship used to account for this in the diffusion simulation is Poisson's equation. It accounts for changes in potential within given space, taking charge (q), dielectric permittivity of the material (ε), concentration of holes and electrons (n, p), and immobile donors and acceptors (N_D^+ , N_A^-) into account.

$$\nabla^2\psi = -\frac{q}{\varepsilon}\left(p - n + N_D^+ - N_A^-\right) \tag{5-19}$$

$$\frac{n}{n_i} = \exp\left(\frac{\psi}{kT}\right) \tag{5-20}$$

$$\frac{p}{n_i} = \exp\left(\frac{-\psi}{kT}\right) \tag{5-21}$$

Given that the net donor concentration ($N_D^+ - N_A^-$) is known, equations 5-19 through 5-21 can be solved simultaneously for the electron, hole and potential values in the material. The net donor concentration consistently converged to ~1.7×10^{19} cm^{-3} for silicon in InGaAs upon annealing, which served as the upper limit of net activation for the Si:InGaAs system.

Calculation of intrinsic carrier concentration: Intrinsic carrier concentrations were calculated using empirical relations developed by Paul et al, and fit into an Arrhenius relationship for use in the simulation. The temperature and composition-dependent relationship used is included in equations 5-22 and 5-23[137]:

$$n_i(x,T) = 4.8327 \times 10^{15} \left[(0.41 + 0.009x)^{\frac{3}{2}} + (0.027 + 0.047x)^{\frac{3}{2}}\right]^{\frac{1}{2}} \times$$

$$(0.025 + 0.043x)^{\frac{3}{4}} \times \left[T^{\frac{3}{2}} e^{-\frac{\epsilon}{2}} \left(1 + \frac{3.75}{\epsilon} + \frac{3.2812}{\epsilon^2} - \frac{2.4609}{\epsilon^3}\right)^{\frac{1}{2}}\right] \quad (5\text{-}22)$$

Where

$$\epsilon = \frac{E_g}{k_B T} \quad (5\text{-}23)$$

And the variable x corresponds to the fraction of gallium on the cation site, following the form $In_{1-x}Ga_xAs$ of a ternary alloy of InAs and GaAs of varying concentration. As seen from Equation 5-23, band gap is a variable that influences the intrinsic carrier concentration in the material. Band gap narrowing is a real phenomenon observed for heavily doped materials like InGaAs, and can affect device operation, notably carrier tunneling [138–140]. For simplicity, band gap narrowing was not accounted for in the diffusion model.

5.4.9 Dopant-Defect Pair Diffusion Model - Dilute Concentration Approximation

The next layer of complexity involves dealing with point defect and dopant interactions to serve as the driving force for dopant redistribution, referred as the “pair” model in floops[135]. Usually this deals with the pairing of a dopant with a type of defect, or number of defects- for example an interstitial coupled with a boron atom, or an antimony atom paired with a vacancy in silicon. A common approach for dopant-defect pair modelling is to carry out the dilute concentration approximation (DCA). This

approach assumes that the number of dopant-defect pairs is much less than the total number of defects present in the medium, and that the dopant-defect reaction is in thermal equilibrium. The binding term K_{AV} quantifies the relative concentrations of AX pairs and isolated dopant and defects through the relation:

$$K_{AX}(T) = \frac{[A][X]}{[AX]} \tag{5-24}$$

Given that the reaction is:

$$A + X \leftrightarrow AX \tag{5-25}$$

K_{AX} can be solved for a specific dopant defect pair in a specific medium using the given relation outlined by Fahey [26]:

$$K_{AX} = \frac{\theta_{AX}}{C_S} \exp\left(\frac{E_{AX}^b}{kT}\right) \tag{5-26}$$

C_S is the lattice or sublattice site density, and θ_{AX} is the number of equivalent configurations of the dopant defect pair. For InGaAs, there are 12 equivalent number of second nearest neighbor sites, and the cation sublattice density (~2×10^{22}cm^{-3}) is used. The activation energy in the exponential term is the dopant-defect binding energy, which quantifies how strongly a dopant and defect are paired. It has been characterized by the difference in the formation energy of the isolated impurity and defects and the formation energy of the AX pair [141].

$$E_b = E_A^f + E_B^f - E_{AB}^f \tag{5-27}$$

The greater difference in formation energy the greater the concentration of the AX pair. The concentration of active substitutional dopants that are not paired with a defect are calculated using the binding term as illustrated in Equation 5-28.

$$C_A^+ = \frac{C_A}{1.0 + C_V^* K_{AV}} \tag{5-28}$$

In this case the mobile concentration of dopants is governed by our mobility limit. With the dopant pair model, the resulting pair flux is the effective flux of the impurity-defect pair as shown in Equation 5-29.

$$FluxAX = \frac{\left(D_{AX0} + \sum_z D_{AXz}\left(\frac{n}{n_i}\right)^z\right)}{\left(\frac{n}{n_i}\right)} \times \nabla\left(C_A^+ \times \frac{C_X}{C_X^*} \times \left(\frac{n}{n_i}\right)\right) \quad (5\text{-}29)$$

The pair model build upon previous models by accounting for local defect concentrations as well as local fermi levels. With this added complexity, it is important to realistically account for the relative abundance of the dopants, defects, and pairs that are formed in different temperatures and doping levels.

DFT calculations of Defect Formation Energies

In order to more realistically account for defect reactions in the Si-doped InGaAs system, collaboration was carried out with the Vanderbilt University Sokrates Pantelides Group to obtain InGaAs-specific formation energies of the proposed reacting species using density functional theory (DFT) calculations. The defect formation energies were calculated using local density approximation (LDA), projector augmented wave (PAW) potentials[142], and a plane-wave basis as used in the Vienna ab-initio simulation package (VASP) code[143,144]. Supercells with 144 atoms were used for the calculations with random cation occupancy of In and Ga. Larger supercells require more time for convergence, yet allows for greater accuracy and consistency of the results given that charge neutrality and doping concentrations are being simulated in this finite volume of material. Variations of these parameters have a smaller effect on larger super cells, which is advantageous for quantifying vital parameters like formation and migration energies of species.

Resulting calculated formation energies of Si_{III}^{+}, V_{III}^{3-}, and $(Si_{III} - V_{III})$ pair with respect to fermi level are shown in Figure 5-6. Defects of different charge states become the most abundant in the material at a given fermi level, and their charge states are included those respective regimes in the Figure. As the fermi level increases towards the conduction band, formation energies of both negatively charged cation vacancies and the Si_{III}-V pair decreases. It is assumed in the model that transition from doubly to triply negatively charged cation vacancies and dopant defect pairs are instantaneous compared to diffusion phenomena.

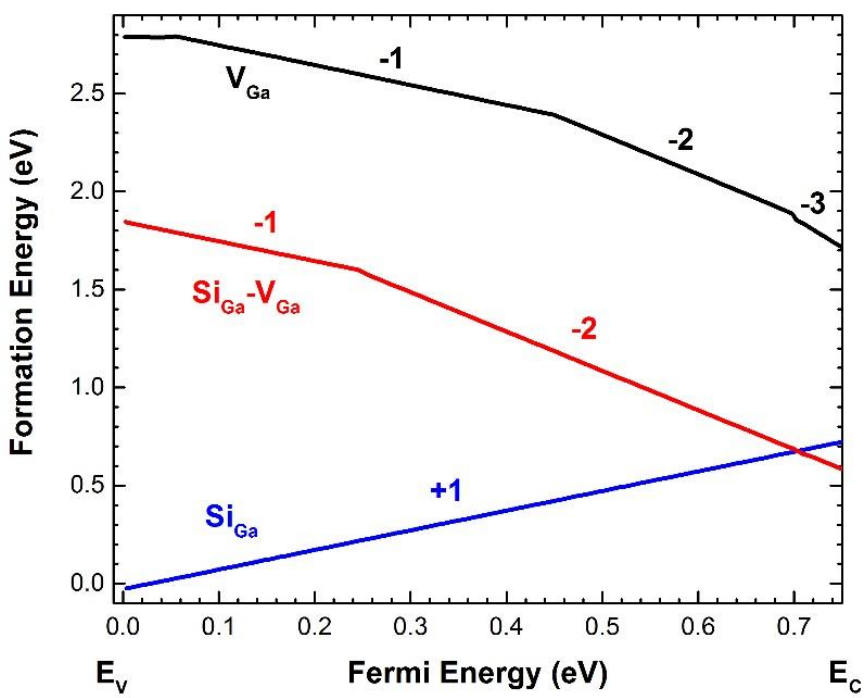

Figure 5-6. Formation energies of notable defects in Si-doped InGaAs obtained via DFT calculations [145].

Equations 5-30 and 5-31[14] were used to calculate local fermi levels (E_{Fn}, E_{Fp}) based on the doping in a given region of the material. Formation energies of all calculated species were fit to functions with respect to fermi level (included in appendix B), and were used to calculate the binding energies based the local doping levels.

$$N_d = n_i \exp\left(\frac{E_{Fn}-E_{Fi}}{kT}\right) \quad (5\text{-}30)$$

$$p = n_i \exp\left(\frac{E_{Fp}-E_{Fi}}{kT}\right) \quad (5\text{-}31)$$

For the pair diffusion model, a set Si_{III}-V_{III} binding energy 1.85eV of was used to improve convergence times of the simulations. Appendix B includes the example predicted post-anneal profiles using the unified predictive model, which is shown to be more accurate for shorter and longer annealing conditions. This unified diffusion model was a collection of the individual extracted parameters set into relationships, in an effort to predict the concentration-dependent diffusion for implanted and grown in Si in a variety of processing conditions. The specifics of different parameters for this model is included in appendix B. More exact fits were achieved to extract individual diffusivities, as demonstrated in Figure 5-7 and 5-8. Figure 5-9 illustrates the effective diffusivities of Si_{III}-V_{III} pair at a concentration of $1\times10^{19}cm^{-3}$ for comparison. A migration energy of ~4.0 eV is in support that vacancy mediated diffusion is the primary mechanism of redistribution of Si in InGaAs.

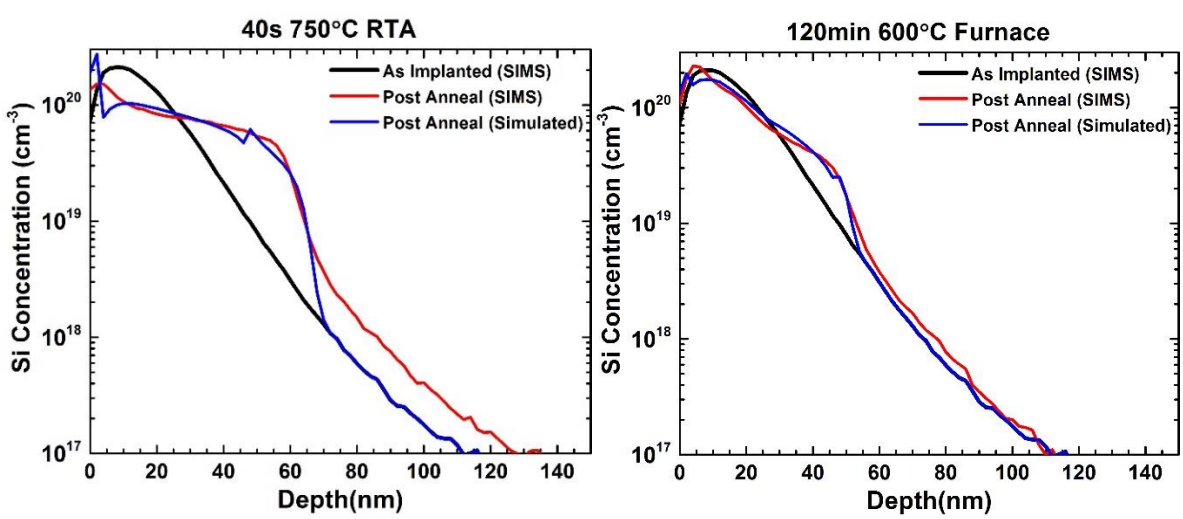

Figure 5-7. Example Dilute Pair Model Fits of 10keV $5\times10^{14}cm^{-2}$ Si^+ implant obtained in FLOOPS.

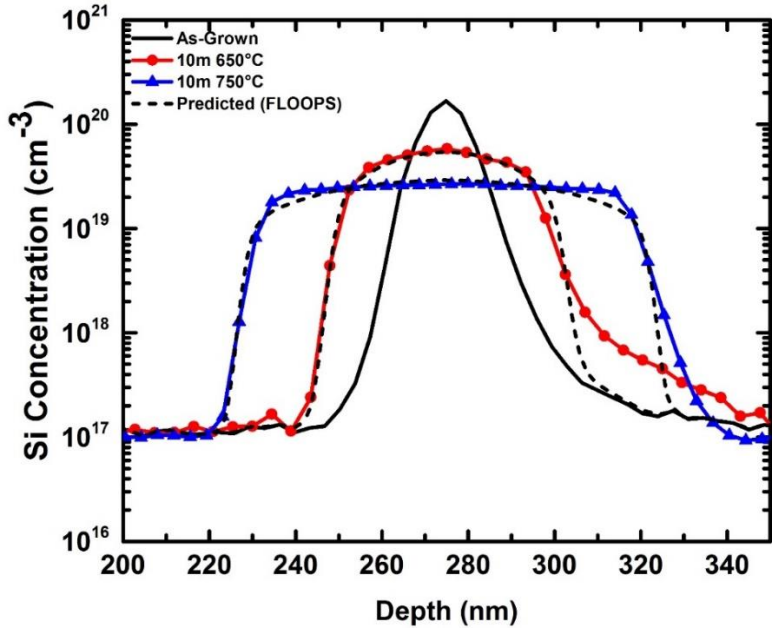

Figure 5-8: Example Pair Model Fits of 2×10^{20} cm^{-3} peak concentration Si marker layer in InGaAs[146].

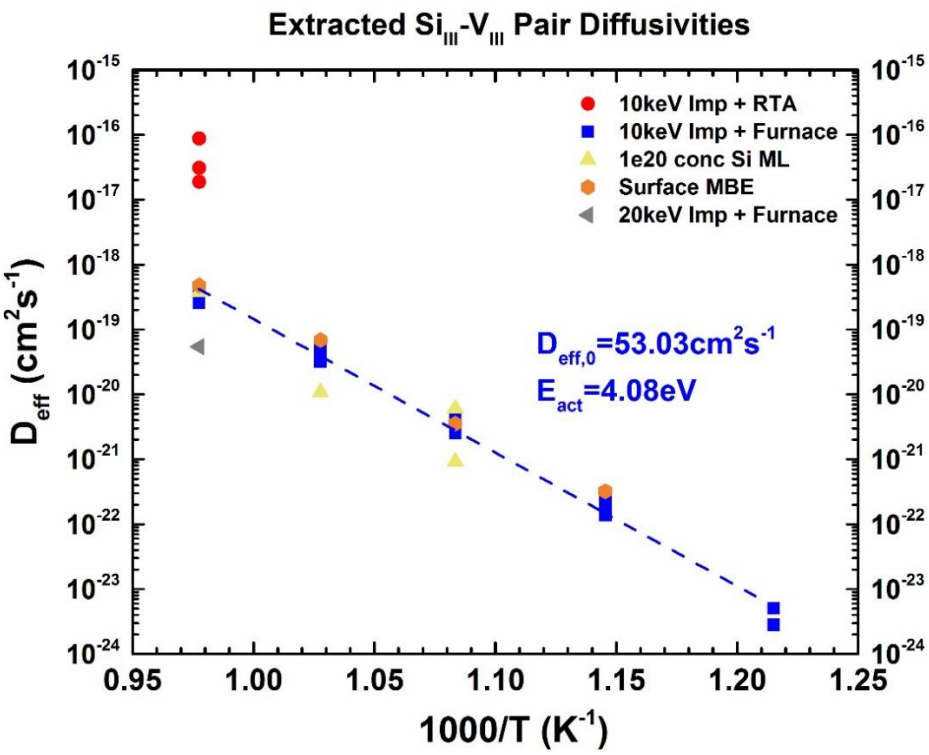

Figure 5-9. Extracted Si_{III}-V_{III} pair Effective Diffusivities with respect to inverse temperature. Arrhenius parameters of 10keV implant furnace anneals are displayed.

Coupled Activation Model

The primary approach to activation prediction in this project also deals with the primary activation convergence value (~$1.7\times10^{19}cm^{-3}$) determined experimentally. Using this value, and the variable smoothing function as found in Equation 5-14, the net activation of silicon profiles can be predicted using the “Layers” command in floops. An illustration of this approach is displayed in Figure 5-10. Accuracy of activation prediction is closely linked to how well the Si plateau is modeled with the diffusion model. Since fitting of the plateau portions of profiles was a primary focus for fitting in the diffusion model, activation prediction followed suit, consistently predicting within 20% of the measured sheet numbers of ion-implanted Si via Hall Effect. With greater Si diffusion observed, more consistent predicted net activation was predicted. The only major deviation occurred with MBE-grown samples as studied by Lind et al[93], where rapid initial deactivation occurs, not in line with the predictive model. Generally better prediction occurred when measurable diffusion is observed. A full range of activation predictions and percent difference from measured sheet numbers are included in Appendix D.

Accuracy of activation and diffusion is more accurate for longer term and high temperature anneals, where silicon diffusion is greater. Additional, in-depth study of the transient short-time anneals are needed, where silicon has not significantly redistributed. A corresponding model will be needed for this highly-transient regime in order to have an accurate and reliable prediction model for all processing regimes, especially those of technological interest today.

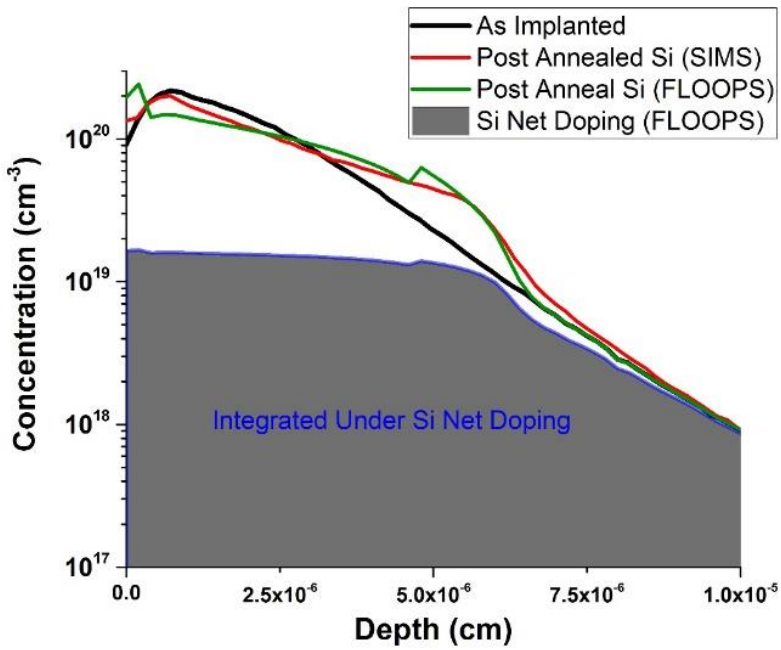

Figure 5-10. Illustration of technique used to predict active sheet number in FLOOPS. 20keV $6\times10^{14}cm^{-2}$ Si^{+} implant annealed at 10min 750°C used here

5.4.10 Non Dilute Concentration Approximation Model

The whole basis of assuming equilibrium between AX pairs and isolated dopant defects, in the dilute concentration approximation (DCA) cannot hold for the conditions we seek to model. In this approximation, it is assumed that the number of dopant-defect pairs are much smaller than the total number of defects, where $C_{AX} << C_X$ [26]. This assumption is valid only when the dopant concentration is low enough such that the bound pairs is insignificant to the total defect concentration in the material. In the case of heavily-doped InGaAs, this is likely not the case. Given the fact that there are significantly more silicon atoms, than calculated vacancies, this assumption cannot be made. A new isolated substitutional equation was derived, adding a few new terms from Law et al[147]:

$$\frac{\partial C_{AV}}{\partial t} = \left(\frac{\left(D_{AV^0} + \sum_z D_{AVz} \left(\frac{n}{n_i}\right)^z \right) K_{AV} G^{c-1} C^*_{V_{III}}}{\left(\frac{n}{n_i}\right)} \right) \nabla \left(C_A^+ \frac{C_V}{C_V^*} \frac{n}{n_i} \right) \quad (32)$$

Where a more elaborate isolated silicon equation is included below:

$$C_A^+ = \frac{C_A}{G_{V_{III}} K_{AV} C^*_{V_{III}} + 1} \tag{33}$$

All parameters have the same meaning as in previous models, and the added G term is $\left(\frac{n}{n_i}\right)^{1-c}$ where c is the charge state of the dopant-defect pair. Unlike the dilute approximation pair model, the model described above can be used to extract dopant-explicit diffusivities, rather than just the dopant-defect pair. The model was successfully adapted and run in FLOOPS for silicon in InGaAs but was not thoroughly tested. Further development of models with greater complexity, such as non-dilute approximations could further predictive model development for the Si:InGaAs system.

CHAPTER 6
SUMMARY, CONCLUSIONS AND SUGGESTIONS FOR FUTURE WORK

6.1 Project Summary and Conclusions

This project was largely divided into two parts: one focusing on experiment, and maximizing activation of silicon in InGaAs, and the other focusing on modeling experimental results, with a special emphasis on modeling Si diffusion behavior. Activation behavior from this work supports the existence of an intrinsic net activation limit in III-V semiconductors. This intrinsic limit appears to be largely governed by the material itself, rather than the type of dopants that are present and the methods they are introduced. Acceptor-type defects, notably negatively charged cation vacancies are believed to be the primary compensating defect governing the maximum net activation of silicon in InGaAs. This finding is somewhat in line with what was proposed by previous works. In contrast, it is in disagreement with previous works that suggest that amphoteric nature of dopants is not the principle method for achieving maximum activation values.

Si diffusion is a more important factor for consideration at present than in previous decades, since devices scales and geometries have decreased significantly. From this work, silicon has shown the capacity for two distinct diffusion regimes: 1) an exponential- broadening profile as a result of implant channeling, and 2) a pronounced concentration-dependent diffusion behavior for longer anneal times. Both of these diffusion regimes are observed for ion-implanted samples, while only concentration dependent diffusion is observed for Si-doped InGaAs grown in by MBE. Modelling of the concentration-dependent profiles were the major focus of the modelling efforts, and a

coupled diffusion and activation model was successfully developed with good agreement with experiment.

6.2 Suggestions for Future Work

There are several additional opportunities that could be pursued regarding this research topic. One of the major challenges of the project was the observation and study of point defects, since they are to integral to dopant diffusion and activation and cannot be directly measured or observed easily. Further ab-initio calculations have the potential to fill that gap, in order to have a comprehensive view of the activation and diffusion behavior by taking a close look at possible defects and charge states possible at different substrate conditions. It can also be particularly helpful in determining and quantifying an nth nearest neighbor range or percolation-like effect in InGaAs or related systems.

Due to the existence of different diffusion and activation observed with respect to time, it would also be beneficial to enhance the predictive models to account for dopant behavior in all time regimes. The models could be developed to better predict the window of short time anneals where there is rapid deactivation and activation, and negligible diffusion. This enhancement and improvement in activation prediction could be analogous to the development of the diffusion model by inclusion of a central point defect mechanism for longer time furnace anneals.

Non-planar transistor designs are the cutting edge geometries at present, and will subsequently require 2D and 3D simulation and predictions capabilities. Another way to build upon this modelling work would be to develop three dimensional models for application to multi-gate devices.

Many material-specific parameters for $In_xGa_{1-x}As$ are not as abundant or freely available as parameters for the silicon system. More experiments that can further support or confirm calculated values, such as cation interstitial diffusivities, would be of great benefit to process modelling of these new materials.

Si dopants grown-in by MBE seem to be the most advantageous choice for doping InGaAs with silicon, since there are higher activation values achieved despite being metastable, and have the ability to have steeper junctions than ion implanted Si, especially for smaller thermal budgets. Co-doping via ion-implantation may not have been effective for improving activation, but co-doping by MBE or other grown-in methods could be an opportunity to study the site occupation of dopants without the disruption caused by implant damage. Finally, further work with laser annealing would be of promise, coupled with MBE grown-in samples, to minimize diffusion and deactivation.

APPENDIX A
InGaAs SAMPLE GROWTH AND PROCESSING DETAILS

Table A-1. $In_{0.53}Ga_{0.47}As$ MBE Growth, Layer Thickness and Doping Conditions

Sample Set	Sample Thickness (nm)	Doping or Implant Conditions
Implanted Si^+ - Diffusion study	300	10keV $5\times10^{14}cm^{-2}$ Si^+ at 80°C
Surface doped Si Layer - activation study	380	60nm $6\times10^{19}cm^{-3}$ doped surface layer
Si Implanted - activation study	296	10keV $5\times10^{14}cm^{-2}$ Si^+ at 100°C
Si Marker Layer (high conc.)	962	50nm $1\times10^{20}cm^{-3}$ centered 273nm deep
Si Marker Layer (low conc.)	522	50nm $1\times10^{19}cm^{-3}$ centered 240nm deep
Surface doped Si Layer - Be diffusion study	750	50nm $3.5\times10^{19}cm^{-3}$ surface layer
Be Marker Layer - Be diffusion study	750	44nm $3\times10^{18}cm^{-3}$ centered 370nm deep

APPENDIX B
PARAMETERS USED FOR PAIR DIFFUSION MODEL

Table B-1. Calculated Si mobile concentration prefactors and activation energies, based on sample set.

Sample Set	Prefactor	E_{act}
10keV Implants, RTAs	6.50×10^{20}	0
10keV Implants, Furnace Anneals	5.71×10^{30}	1.82
Si Marker Layer	1.00×10^{22}	0
MBE surface Doped	1.00×10^{22}	0

Table B-2. Fickian and Concentration–dependent diffusion components and migration energies for the dopant-defect pair model. Extracted from individual profile data and fit to Arrhenius relationships.

Sample Set	Fickian (D_0)		Concentration Dependent Term(D_{n3})	
	Prefactor	E_{act}	Prefactor	E_{act}
10keV Implants, Furnace Anneals	3.196×10^{3}	4.75	8.342×10^{5}	5.68
Si Marker Layer	8.588×10^{-6}	2.91	2.447×10^{10}	6.62
MBE surface Doped	4.725×10^{1}	4.09	4.386×10^{4}	5.54

Table B-3. Binding coefficient and intrinsic carrier concentration used for Pair diffusion model.

Parameter	Prefactor	E_{act}
V_{III} Si_{III} binding coefficient K_{AV}	6.06×10^{-22}	-1.847
intrinsic carrier concentration	2.21×10^{20}	0.516

Fitted Defect Formation Energy Functions with respect to Fermi Level- from DFT calculations[145].

$$\mathrm{E}_{\mathrm{f,Si_{III}}} = 1.0024 * E_{fn} - 0.0292 \quad \text{(A1)}$$

$$\mathrm{E}_{\mathrm{f,V_{III}}} = -1.4187 * E_{fn}^2 - 0.3159 * E_{fn} + 2.7858 \quad \text{(A2)}$$

$$\mathrm{E}_{\mathrm{f,Si}_{III}-\mathrm{V}_{III}} = 8.8334 \times 10^{-7} * E_{fn}^3 - 1.88228 \times 10^{-4} * E_{fn}^2 - 2.4272 \times 10^{-3} * E_{fn} + 1.8266 \quad \text{(A3)}$$

APPENDIX C
EXAMPLE SIMS AND PREDICTED SI PROFILES USING COMPREHENSIVE PAIR MODEL

(not using individual fit values)

Figure C-1.10keV $5x10^{14}cm^{-2}$ Si^{+} Implant - 10-40s 750°C RTA

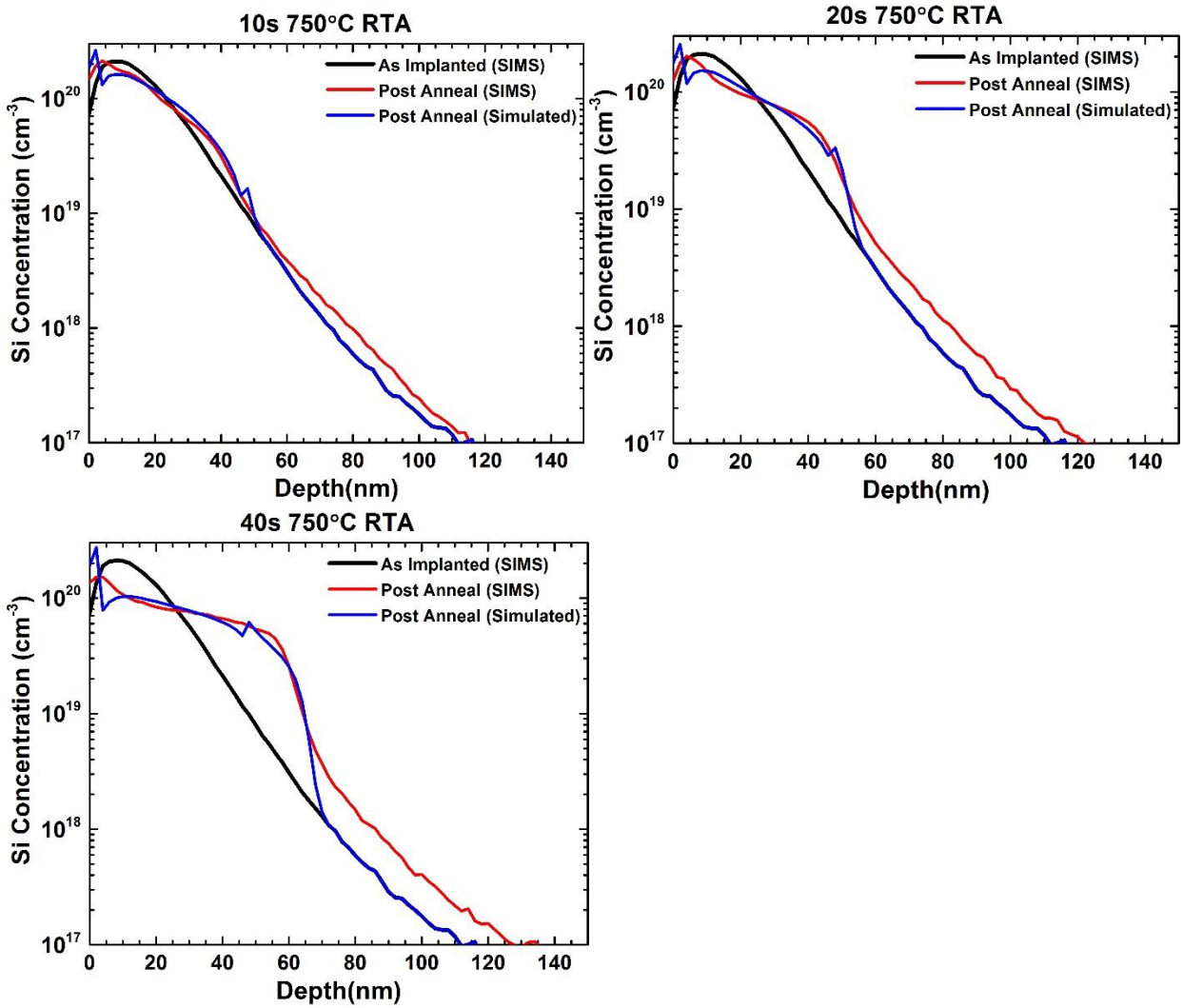

Figure C-2. 10keV $5x10^{14}cm^{-2}$ Si^{+} Implant 5min-16hrs, 550-750°C Furnace

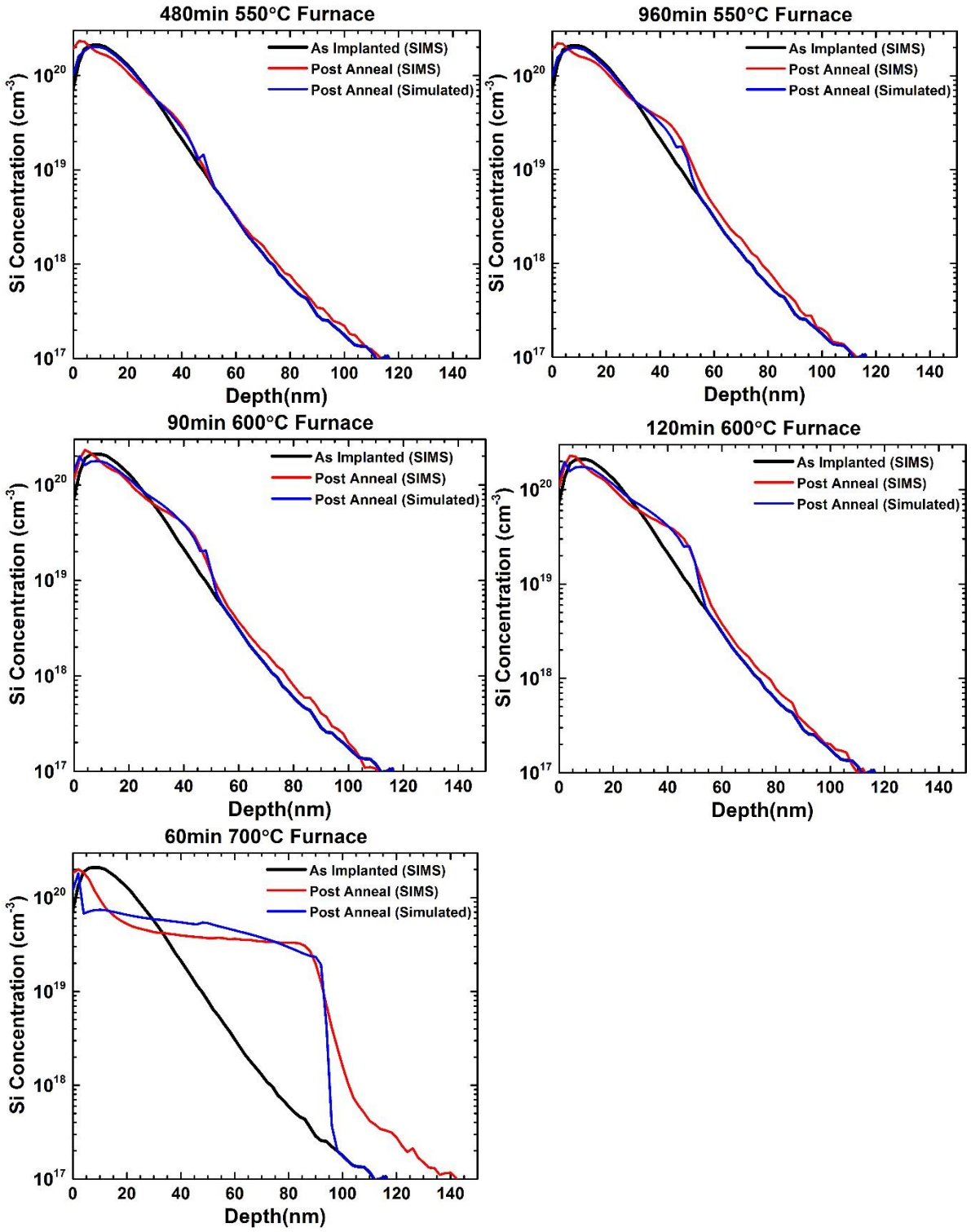

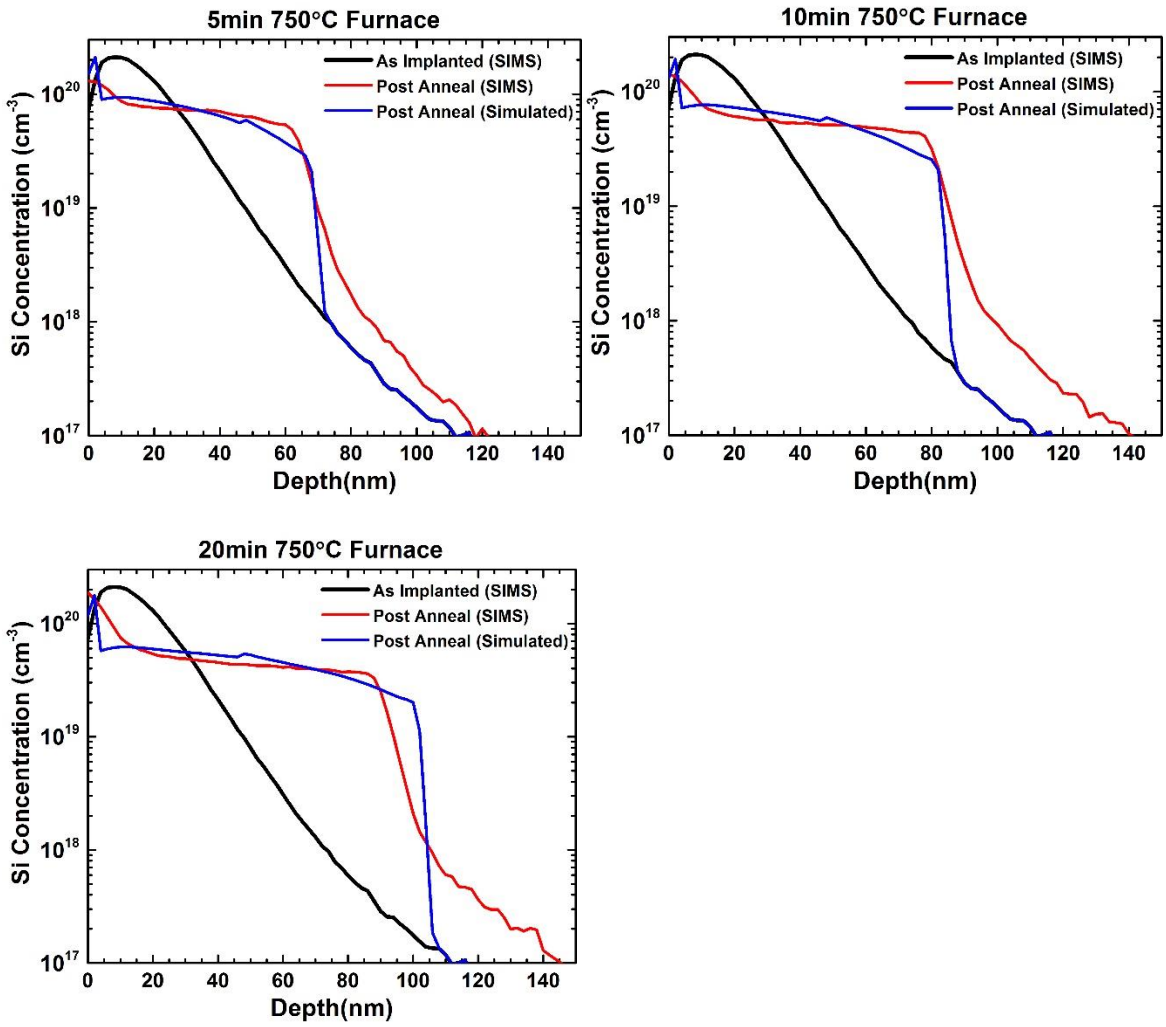
5min 750°C Furnace
10min 750°C Furnace
20min 750°C Furnace
As Implanted (SIMS)
Post Anneal (SIMS)
Post Anneal (Simulated)
Si Concentration (cm^{-3})
Depth(nm)
10^{20}
10^{19}
10^{18}
10^{17}
0
20
40
60
80
100
120
140

Figure C-3. MBE Si Marker Layer ~275 below surface

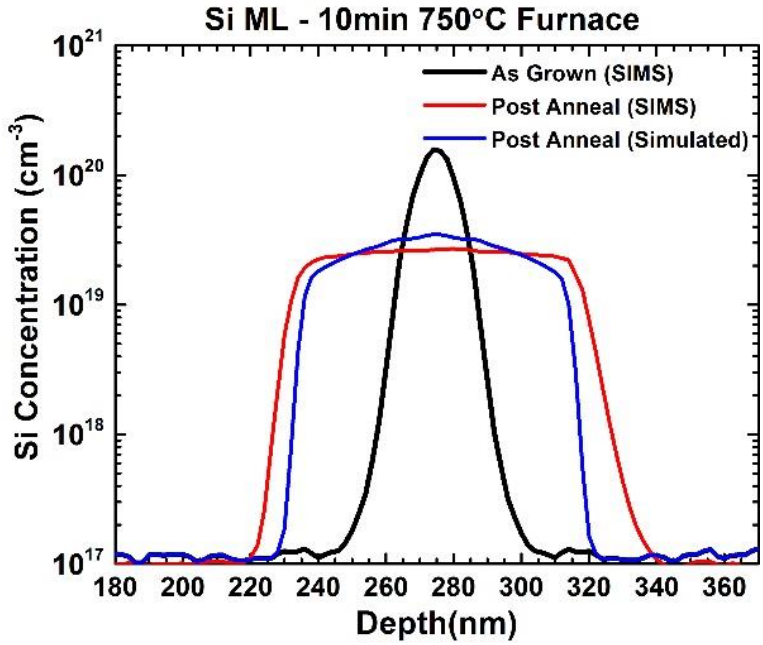

Figure C-4. MBE Si Doped surface

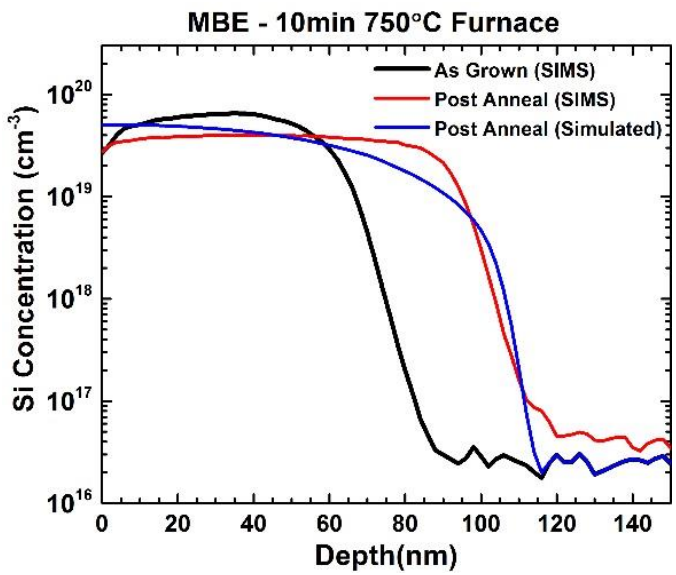

APPENDIX D
MEASURED AND PREDICTED ACTIVATION RESULTS – INTEGRATION APPROACH

Figure D-1. 10keV $5x10^{14}cm^{-2}$ Si^{+} Implant - 5-40s 750°C RTA

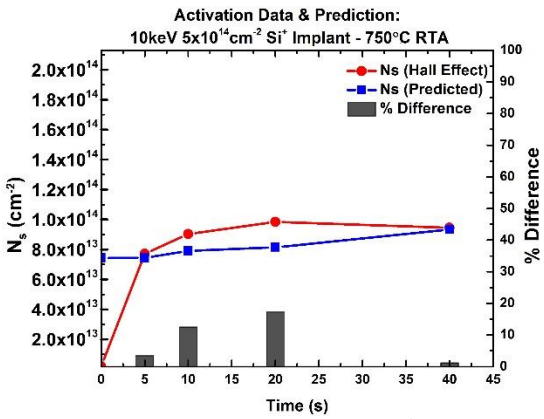

Figure D-2 10keV $5x10^{14}cm^{-2}$ Si^{+} Implant 5min-16hrs 550-750°C Furnace

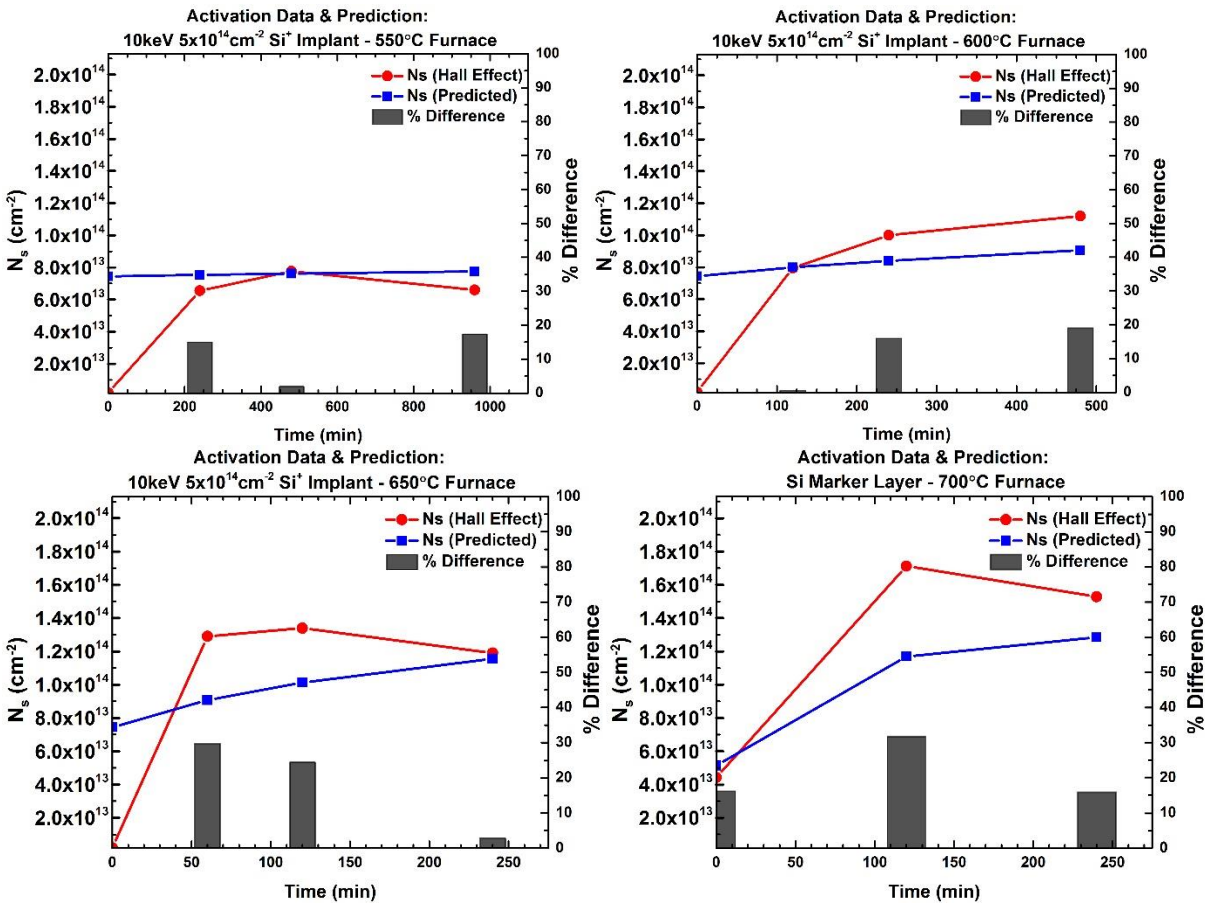

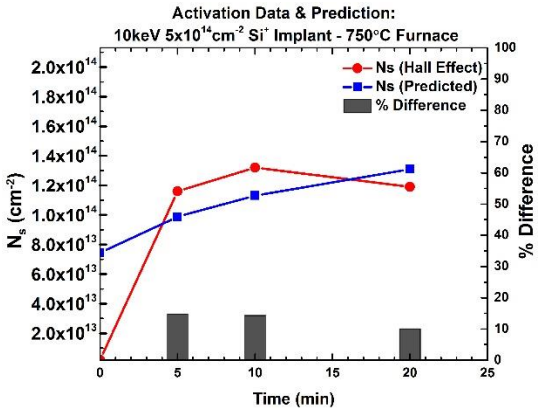

Figure D-3. MBE Si Marker Layer ~275 below surface - 10-240m 650-700°C Furnace

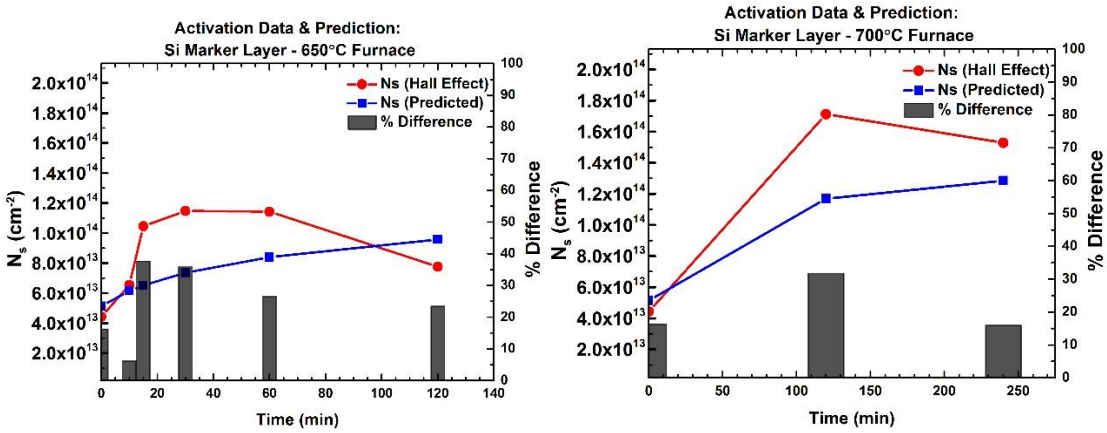

Figure D-4. MBE Si Doped surface 10min 550-750°C Furnace

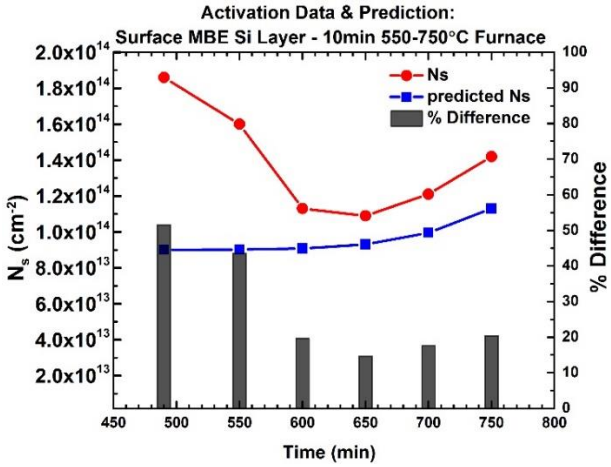

LIST OF REFERENCES

[1] G.E. Moore, IEEE Solid-State Circuits Soc. Newsl. **11**, 33 (2006).

[2] R.H. Dennard, F.H. Gaensslen, V.L. Rideout, E. Bassous, and A.R. LeBlanc, IEEE J. Solid-State Circuits **9**, 256 (1974).

[3] E.C. Jones and E. Ishida, Mater. Sci. Eng. R-Rep. **24**, 1 (1998).

[4] Y. Taur and T.H. Ning, *Fundamentals of Modern VLSI Devices*, 2nd ed (Cambridge University Press, Cambridge, UK ; New York, 2009).

[5] T. Brozek, editor , *Micro-and Nanoelectronics: Emerging Device Challenges and Solutions* (Taylor & Francis, Boca Raton, 2014).

[6]Int. Technol. Roadmap Semicond. (2016).

[7] J.A. Carballo, W.T.J. Chan, P.A. Gargini, A.B. Kahng, and S. Nath, in *2014 IEEE 32nd Int. Conf. Comput. Des. ICCD* (2014), pp. 139–146.

[8] C. Martin, Nat. Nanotechnol. **11**, 112 (2016).

[9] M.T. Bohr, R.S. Chau, T. Ghani, and K. Mistry, IEEE Spectr. **44**, 29 (2007).

[10] J.A. del Alamo, Nature **479**, 317 (2011).

[11] M. Heyns and W. Tsai, MRS Bull. **34**, 485 (2009).

[12]International Electron Devices Meeting 2015.

[13] M.J.W. Rodwell, M. Wistey, U. Singisetti, G. Burek, A. Gossard, S. Stemmer, R. Engel-Herbert, Y. Hwang, Y. Zheng, C.V. de Walle, P. Asbeck, Y. Taur, A. Kummel, B. Yu, D. Wang, Y. Yuan, C. Palmstrom, E. Arkun, P. Simmonds, P. McIntyre, J. Harris, M.V. Fischetti, and C. Sachs, in *20th Int. Conf. Indium Phosphide Relat. Mater. 2008 IPRM 2008* (2008), pp. 1–6.

[14] S.O. Kasap, *Principles of Electronic Materials and Devices*, 3rd ed (McGraw-Hill, Boston, 2006).

[15] A. Baraskar, A.C. Gossard, and M.J.W. Rodwell, J. Appl. Phys. **114**, 154516 (2013).

[16] W. Walukiewicz, Phys. Rev. B **50**, 5221 (1994).

[17] W.D. Callister, *Materials Science and Engineering: An Introduction*, 7th ed (John Wiley & Sons, New York, 2007).

[18] D. Kohen, R. Made, S. Bao, K.H. Lee, K. Lee, C.S. Tan, S. Yoon, and E.A. Fitzgerald, (2009).

[19] L. Czornomaz, N. Daix, K. Cheng, D. Caimi, C. Rossel, K. Lister, M. Sousa, and J. Fompeyrine, in *2013 IEEE Int. Electron Devices Meet.* (2013), pp. 2.8.1–2.8.4.

[20] S. Takagi, M. Sugiyama, T. Yasuda, and M. Takenaka, ECS Trans. **19**, 9 (2009).

[21] H. Mehrer, *Diffusion in Solids: Fundamentals, Methods, Materials, Diffusion-Controlled Processes* (Springer, Berlin ; New York, 2007).

[22] J.A. Nesbitts and R.W. Heckel, Metall. Trans. A **18**, 2075 (1987).

[23] Y.M. Haddara and J.C. Bravman, Annu. Rev. Mater. Sci. **28**, 185 (1998).

[24] J.D. Plummer, M.D. Deal, and P.B. Griffin, *Silicon VLSI Technology: Fundamentals, Practice and Modeling* (Prentice Hall, Upper Saddle River, NJ, 2000).

[25] Y. Nishi and R. Doering, editors , *Handbook of Semiconductor Manufacturing Technology* (Marcel Dekker, New York, 2000).

[26] P. Fahey, P. Griffin, and J. Plummer, Rev. Mod. Phys. **61**, 289 (1989).

[27] J.J. Murray, Comparison of the Diffusion Characteristics of Carbon, Silicon and Germanium in Gallium Arsenide, Ph.D., Stanford University, 1992.

[28] E.G. Seebauer and M.C. Kratzer, Mater. Sci. Eng. R Rep. **55**, 57 (2006).

[29] T.Y. Tan, H.-M. You, and U.M. Gösele, Appl. Phys. A **56**, 249 (1993).

[30] A. Alian, G. Brammertz, N. Waldron, C. Merckling, G. Hellings, H.C. Lin, W.E. Wang, M. Meuris, E. Simoen, K.D. Meyer, and M. Heyns, Microelectron. Eng. **88**, 155 (2011).

[31] E. Hailemariam, S.J. Pearton, W.S. Hobson, H.S. Luftman, and A.P. Perley, J. Appl. Phys. **71**, 215 (1992).

[32] M.V. Rao, S.M. Gulwadi, P.E. Thompson, A. Fathimulla, and O.A. Aina, J. Electron. Mater. **18**, 131 (1989).

[33] A.D. Lilak, Analysis and Modeling of Transient Phenomena in Boron -Doped Silicon, Ph.D., University of Florida, 2001.

[34] R.A. Camillo-Castillo, Boron Activation and Diffusion in Silicon for Varying Initial-Process Conditions during Flash-Assist Rapid Thermal Annealing, University of Florida, 2006.

[35] M.E. Greiner and J.F. Gibbons, Appl. Phys. Lett. **44**, 750 (1984).

[36] D.G. Deppe and N.H. Jr, J. Appl. Phys. **64**, R93 (1988).

[37] S. Yu, U.M. Gösele, and T.Y. Tan, J. Appl. Phys. **66**, 2952 (1989).

[38] R.S. Bhattacharya and P.P. Pronko, Appl. Phys. Lett. **40**, 890 (1982).

[39] M. Schultz, U. Egger, R. Scholz, O. Breitenstein, U. Gösele, and T.Y. Tan, J. Appl. Phys. **83**, 5295 (1998).

[40] T.E.M. Staab, R.M. Nieminen, J. Gebauer, R. Krause-Rehberg, M. Luysberg, M. Haugk, and T. Frauenheim, Phys. Rev. Lett. **87**, 045504 (2001).

[41] F. El-Mellouhi and N. Mousseau, Appl. Phys. A **86**, 309 (2006).

[42] E.L. Allen, J.J. Murray, M.D. Deal, J.D. Plummer, K.S. Jones, and W.S. Rubart, J. Electrochem. Soc. **138**, 3440 (1991).

[43] W. Shockley and J. Last, Phys. Rev. **107**, 392 (1957).

[44] E.L. Allen, Diffusion of Ion-Implanted Group IVn-Type Dopants in Gallium Arsenide and Gallium Arsenide-Based Superlattices, Ph.D., Stanford University, 1992.

[45] P. Mei, H.W. Yoon, T. Venkatesan, S.A. Schwarz, and J.P. Harbison, Appl. Phys. Lett. **50**, 1823 (1987).

[46] C.C. Lee, M.D. Deal, K.S. Jones, H.G. Robinson, and J.C. Bravman, J. Electrochem. Soc. **141**, 2245 (1994).

[47] A.G. Lind, T.P.M. Jr, V.C. Sorg, E.L. Kennon, V.Q. Truong, H.L. Aldridge, C. Hatem, M.O. Thompson, and K.S. Jones, J. Appl. Phys. **119**, 095705 (2016).

[48] S.J. Pearton, A.R.V. Neida, J.M. Brown, K.T. Short, L.J. Oster, and U.K. Chakrabarti, J. Appl. Phys. **64**, 629 (1988).

[49] T. Takamoto, M. Yumaguchi, E. Ikeda, T. Agui, H. Kurita, and M. Al-Jassim, J. Appl. Phys. **85**, 1481 (1999).

[50] H. Fushimi, M. Shinohara, and K. Wada, J. Appl. Phys. **81**, 1745 (1997).

[51] D. Stauffer, *Introduction to Percolation Theory* (Taylor & Francis, London ; Philadelphia, 1985).

[52] D. Stauffer, Phys. Rep. **54**, 1 (1979).

[53] D. Mathiot and J.C. Pfister, J. Phys. Lett. **43**, 453 (1982).

[54] J. Xie and S.P. Chen, Phys. Rev. Lett. **83**, 1795 (1999).

[55] H.G. Robinson, M.D. Deal, and D.A. Stevenson, Appl. Phys. Lett. **56**, 554 (1990).

[56] K.A. Gable, Boron Activation and Diffusion during Millisecond Annealing of Ion-Implanted Silicon, University of Florida, 2004.

[57] R.S. Bhattacharya, P.P. Pronko, and S.C. Ling, Appl. Phys. Lett. **42**, 880 (1983).

[58] W. Walukiewicz, L. Lagowski, L. Jastrzebski, M. Lichtensteiger, and H.C. Gatos, J. Appl. Phys. **50**, 899 (1979).

[59] A. Bindal, K.L. Wang, S.J. Chang, M.A. Kallel, and O.M. Stafsudd, J. Appl. Phys. **65**, 1246 (1989).

[60] S. Sugitani, F. Hyuga, and K. Yamasaki, J. Appl. Phys. **67**, 552 (1990).

[61] A.N. Akimov, L.A. Vlasukova, Y.A. Bumai, and K.S. Gorupa, Vacuum **63**, 491 (2001).

[62] T. Ambridge, R. Heckingbottom, E.C. Bell, B.J. Sealy, K.G. Stephens, and R.K. Surridge, Electron. Lett. **11**, 314 (1975).

[63] S.G. Liu, S.Y. Narayan, C.W. Magee, and C.P. Wu, Appl. Phys. Lett. **41**, 72 (1982).

[64] W. Walukiewicz, Appl. Phys. Lett. **54**, 2094 (1989).

[65] W. Walukiewicz, Phys. B Condens. Matter **302–303**, 123 (2001).

[66] J.F. Ziegler, editor , *Ion Implantation: Science and Technology*, 2nd ed (Academic Press, Boston, 1988).

[67] S.J. Pearton, Mater. Sci. Rep. **4**, 313 (1990).

[68] J. Werking, G. Tuttle, C. Nguyen, E.L. Hu, and H. Kroemer, Appl. Phys. Lett. **57**, 905 (1990).

[69] K. S. Jones and C. J. Santana, J. Mater. Res. **6**, 1048 (1991).

[70] M.D. Giles, J. Electrochem. Soc. **138**, 1160 (1991).

[71] Y. Chen, A Universal Species Ion Implantation Model for Implants into Topographically Complex Structures with Multiple Materials, Ph.D., The University of Texas at Austin, 2001.

[72] N. Bohr, Mater Fys Medd Dan Vid Selsk **18**, (1948).

[73] O.B. Firsov, Zh Eksp Teor Fiz 447 (1958).

[74] O.B. Firsov, Sov. Phys. JETP **7**, 308 (1958).

[75] D.K. Brice and K.B. Winterbon, *Ion Implantation Range and Energy Deposition Distributions* (Plenum Press, New York, 1975).

[76] K. Seshan, editor , *Handbook of Thin-Film Deposition Processes and Techniques: Principles, Methods, Equipment, and Applications*, 2nd ed (Noyes Publications, Park Ridge, N.J, 2002).

[77] T.E. Haynes, W.K. Chu, T.L. Aselage, and S.T. Picraux, Appl. Phys. Lett. **49**, 666 (1986).

[78] T. Haynes, W. Chu, and S. Picraux, Appl. Phys. Lett. **50**, 1071 (1987).

[79] Y. Hu, S. Li, G. Jiao, Y.Q. Wu, D. Huang, P.D. Ye, and M.F. Li, IEEE Trans. Nanotechnol. **12**, 806 (2013).

[80] J. Robertson, Appl. Phys. Lett. **94**, 152104 (2009).

[81] Z. Yuan, A. Nainani, A. Kumar, X. Guan, B.R. Bennett, J.B. Boos, M.G. Ancona, and K.C. Saraswat, in *2012 Symp. VLSI Technol. VLSIT* (2012), pp. 185–186.

[82] A.V. Thathachary, G. Lavallee, M. Cantoro, K.K. Bhuwalka, Y.-C. Heo, S. Maeda, and S. Datta, IEEE Electron Device Lett. **36**, 117 (2015).

[83] I. Thayne, R. Hill, M. Holland, X. Li, H. Zhou, D. Macintyre, S. Thoms, K. Kalna, C. Stanley, A. Asenov, R. Droopad, and M. Passlack, ECS Trans. **19**, 275 (2009).

[84] J. Griffiths, Anal. Chem. **80**, 7194 (2008).

[85] M. Sardela, *Practical Materials Characterization* (Springer, 2014).

[86] A. Benninghoven, F.G. Rüdenauer, and H.W. Werner, *Secondary Ion Mass Spectrometry: Basic Concepts, Instrumental Aspects, Applications, and Trends* (J. Wiley, New York, 1987).

[87] S.M. Hu, Mater. Sci. Eng. R Rep. **13**, 105 (1994).

[88] Evans Analytical Group, *SIMS Theory Tutorial* http://www.eag.com/mc/sims-relative-sensitivity-factors.html.

[89] S.A. Campbell, *Fabrication Engineering at the Micro- and Nanoscale* (2013).

[90] A.G. Lind, N.G. Rudawski, N.J. Vito, C. Hatem, M.C. Ridgway, R. Hengstebeck, B.R. Yates, and K.S. Jones, Appl. Phys. Lett. **103**, 232102 (2013).

[91] A. Satta, E. Simoen, T. Clarysse, T. Janssens, A. Benedetti, B.D. Jaeger, M. Meuris, and W. Vandervorst, Appl. Phys. Lett. **87**, 172109 (2005).

[92] S.J. Pearton, A.R.V. Neida, J.M. Brown, K.T. Short, L.J. Oster, and U.K. Chakrabarti, J. Appl. Phys. **64**, 629 (1988).

[93] A.G. Lind, H.L. Aldridge, C. Bomberger, C. Hatem, J. Zide, and K.S. Jones, J. Vac. Sci. Technol. B (2015).

[94] A.J. Moll, K.M. Yu, W. Walukiewicz, W.L. Hansen, and E.E. Haller, Appl. Phys. Lett. **60**, 2383 (1992).

[95] J.P. de Souza and D.K. Sadana, Appl. Phys. Lett. **63**, 3200 (1993).

[96] A.G. Lind, H.L. Aldridge Jr, K.S. Jones, and C. Hatem, J. Vac. Sci. Technol. B **33**, 051217 (2015).

[97] H.G. Robinson, Diffusion of P-Type Dopants in Gallium Arsenide, Ph.D., Stanford University, 1992.

[98] H.L. Aldridge, A.G. Lind, M.E. Law, C. Hatem, and K.S. Jones, Appl. Phys. Lett. **105**, 042113 (2014).

[99] H.S. Leipner, R.F. Scholz, N. Engler, F. Börner, P. Werner, and U. Gösele, Phys. B Condens. Matter **273–274**, 697 (1999).

[100] M. Uematsu, P. Werner, M. Schultz, T.Y. Tan, and U.M. Gösele, Appl. Phys. Lett. **67**, 2863 (1995).

[101] H. Matino, Solid-State Electron. **17**, 35 (1974).

[102] A.B.Y. Young and G.L. Pearson, J. Phys. Chem. Solids **31**, 517 (1970).

[103] B. Goldstein, Phys. Rev. **121**, 1305 (1961).

[104] W. Walukiewicz, Z. Liliental-Weber, J. Jasinski, M. Almonte, A. Prasad, E.E. Haller, E.R. Weber, P. Grenier, and J.F. Whitaker, Appl. Phys. Lett. **69**, 2569 (1996).

[105] A. Milgram and M. Delfino, Appl. Phys. Lett. **42**, 878 (1983).

[106] S. Aronowitz, J. Appl. Phys. **63**, 1037 (1988).

[107] H. Aldridge Jr, A.G. Lind, C.C. Bomberger, Y. Puzyrev, C. Hatem, R.M. Gwilliam, J.M.O. Zide, S.T. Pantelides, M.E. Law, and K.S. Jones, J. Electron. Mater. 1 (2016).

[108] D.J. Eaglesham, P.A. Stolk, H.-J. Gossmann, and J.M. Poate, Appl. Phys. Lett. **65**, 2305 (1994).

[109] P.A. Stolk, H.-J. Gossmann, D.J. Eaglesham, D.C. Jacobson, C.S. Rafferty, G.H. Gilmer, M. Jaraíz, J.M. Poate, H.S. Luftman, and T.E. Haynes, J. Appl. Phys. **81**, 6031 (1997).

[110] D.J. Eaglesham, T.E. Haynes, H.-J. Gossmann, D.C. Jacobson, P.A. Stolk, and J.M. Poate, Appl. Phys. Lett. **70**, 3281 (1997).

[111] S. Koumetz and C. Dubois, J. Cryst. Growth **252**, 14 (2003).

[112] M. Ketata, K. Ketata, S. Koumetz, P. Martin, J. Marcon, and C. Dubois, J. Cryst. Growth **194**, 297 (1998).

[113] S. Koumetz, K. Ketata, M. Ketata, and J. Marcon, J. Phys. -Appl. Phys. **31**, 3421 (1998).

[114] S.D. Koumetz, P. Martin, and H. Murray, J. Appl. Phys. **116**, 103701 (2014).

[115] J. Marcon, S. Gautier, S. Koumetz, K. Ketata, and M. Ketata, Comput. Mater. Sci. **10**, 28 (1998).

[116] J. Marcon, M. Ihaddadene, and K. Ketata, J. Cryst. Growth **253**, 174 (2003).

[117] A.G. Lind, H.L. Aldridge, C.C. Bomberger, C. Hatem, J.M.O. Zide, and K.S. Jones, ECS J. Solid State Sci. Technol. **5**, P3073 (2016).

[118] C.V. Mouli, J. Vac. Sci. Technol. B **18**, 354 (2000).

[119] J.A. Nesbitt, (2001).

[120] K.M. Klein, *Monte Carlo Simulation of Boron-Ion Implantation into Single-Crystal Silicon* (Texas Univ., Austin, TX (United States), 1991).

[121] J.B. J. P. ; Ziegler, M. D. Ziegler, *SRIM - The Stopping and Range of Ions in Matter* (James Ziegler, 2008).

[122] G. Kinchin and R. Pease, Rep. Prog. Phys. **18**, 1 (1955).

[123] M.D. Giles and J.F. Gibbons, Nucl. Instrum. Methods Phys. Res. **209–210, Part 1**, 33 (1983).

[124] L.A. Christel, J.F. Gibbons, and S. Mylroie, J. Appl. Phys. **51**, 6176 (1980).

[125] W.D. Wilson, L.G. Haggmark, and J.P. Biersack, Phys. Rev. B **15**, 2458 (1977).

[126] J. Lindhard, *Integral Equations Governing Radiation Effects: (Notes on Atomic Collisions, III)* (I kommission hos Munksgaard, København, 1963).

[127] M.R. Pinto, Comprehensive Semiconductor Device Simulation for Silicon ULSI, 1991.

[128] M.E. Law, FLOOPS and FLOODS Short Course (2007).

[129] D.D. Wagman, editor , *The NBS Tables of Chemical Thermodynamic Properties: Selected Values for Inorganic and C_1 and C_2 Organic Substances in SI Units* (American Chemical Society and the American Institute of Physics for the National Bureau of Standards, New York, 1982).

[130] J.A.V. Vechten, J. Electrochem. Soc. **122**, 419 (1975).

[131] H.-P. Komsa and A. Pasquarello, Phys. B Condens. Matter **407**, 2833 (2012).

[132] L.J. Guido, W.E. Plano, D.W. Nam, N. Holonyak, J.E. Baker, R.D. Burnham, and P. Gavrilovic, J. Electron. Mater. **17**, 53 (1988).

[133] J.E. Northrup and S.B. Zhang, Phys. Rev. B **47**, 6791 (1993).

[134]*ISE Integrated Systems Engineering Release 9.0 - Part 7: FLOOPS* (n.d.).

[135] M.E. Law, *FLOODS/FLOOPS Manual* (Univ. Florida, Gainesville FL, 1993).

[136] R.H. Kingston and S.F. Neustadter, J. Appl. Phys. **26**, 718 (1955).

[137] S. Paul, J.B. Roy, and P.K. Basu, J. Appl. Phys. **69**, 827 (1991).

[138] S.C. Jain and D.J. Roulston, Solid-State Electron. **34**, 453 (1991).

[139] C. Leroy and P.-G. Rancoita, *Silicon Solid State Devices and Radiation Detection* (World Scientific Publishing Co. Pte Ltd, Singapore ; Hackensack, N. J, 2012).

[140] S.C. Jain, J.M. McGregor, and D.J. Roulston, J. Appl. Phys. **68**, 3747 (1990).

[141] C.G.V. de Walle and J. Neugebauer, J. Appl. Phys. **95**, 3851 (2004).

[142] P.E. Blöchl, Phys. Rev. B **50**, 17953 (1994).

[143] G. Kresse and D. Joubert, Phys. Rev. B **59**, 1758 (1999).

[144] G. Kresse and J. Furthmüller, Comput. Mater. Sci. **6**, 15 (1996).

[145] Y. Puzyrev and S. Pantelides, *DFT Calculations of Defects in InGaAs with Respect to Fermi Level* (Vanderbilt University, 2015).

[146] H.L. Aldridge Jr, A.G. Lind, C.C. Bomberger, Y. Puzyrev, C. Hatem, S. Pantelides, M.E. Law, and K.S. Jones, J. Electron. Mater. **In Publication**, (2016).

[147] M.E. Law, H. Park, and P. Novell, Appl. Phys. Lett. **59**, 3488 (1991).

BIOGRAPHICAL SKETCH

Henry Lee Aldridge Jr. was born in in Albany, Georgia. He then lived in five different states growing up. He lived in the greater Cincinnati, OH area for over 12 years, and attended William Mason High School. He then attended University of Dayton, where he earned a B.S. in Chemical Engineering in 2012. As an undergraduate, Henry had a strong interest in alternative energy, and completed several materials-focused internships at the Wright Patterson Air Force Base, including fuel cell work at the Materials Directorate. He also completed an Honors thesis project on microbial fuel cells utilizing thermophiles to generate electricity from organic matter. In January 2013, Henry started his graduate studies in Materials Science and Engineering at University of Florida, and obtained his Master in Materials Science and Engineering in fall of 2015. During the summer of 2015, Henry carried out a modelling internship with the High Temperature Materials Laboratory at Oak Ridge National Lab, as a part of the GEM graduate fellowship program. In August 2016 Henry completed his PhD. in Materials Science and Engineering from the University of Florida and will join Global Foundries in Burlington, Vermont.